



Master's Thesis

**Background studies for the ComPol  
Cube-Satellite**

Cynthia Glas

Technical University of Munich

May, 2022



First examiner: Prof. Dr. Susanne Mertens

Second examiner: Prof. Dr. Stefan Schönert



## Abstract

The ComPol mission aims to send a Cube Satellite Compton telescope into the low earth orbit in order to investigate the black hole binary Cygnus X-1. Its task is to gain more insights into its geometry, and the underlying processes via the thereby generated X-rays. These high-energy photons are Compton scattered in the Silicon Drift Detector and subsequently absorbed in the calorimeter of the ComPol CubeSat. By using the kinematics of the Compton scattering, information about the energy and the degree of polarization of the X-rays can be obtained and the processes that probably lead to their formation can be determined more precisely.

During its time in orbit, the CubeSat will be exposed to background particles from cosmic radiation and the South Atlantic Anomaly. Both background sources contribute to a different extent to the overall telescope background via direct interactions in the detector system and a time-delayed contribution due to cosmogenic activation. The core challenge of the ComPol mission is the strict size and mass limitation of the overall setup, which means that the shielding has to be carefully designed to match these requirements and simultaneously reach the maximum background suppression. The goal of this thesis is to better understand the background contributions and all its components and to conduct a first study on the impact of the shielding geometry and material. The studies are carried out using the Monte Carlo simulation toolkit Geant4.

The simulations give an estimation of the background rate induced by activation due to the South Atlantic Anomaly revealing its significant contribution to the total telescope background. Furthermore, the geometrical arrangement of the shielding can be improved compared to the preliminary geometry. By comparing different shielding materials with each other, a strong correlation between the photon absorption coefficient and the shielding efficiency is found.



# Contents

<b>1. Introduction</b>	<b>1</b>
1.1. Scientific motivation – Cygnus X-1	1
1.2. Particle Interactions	4
1.2.1. Compton scattering	4
1.2.2. The photoelectric effect	5
1.2.3. Pair production	5
1.3. Compton Telescopes	6
1.3.1. Working principle of a Compton telescope	6
1.3.2. Polarimetry	6
<b>2. The ComPol mission</b>	<b>11</b>
2.1. The ComPol CubeSat	11
2.1.1. The SDD detector	11
2.1.2. The CeBr <sub>3</sub> detector	12
2.2. Data analysis for ComPol	12
2.2.1. Event selection	13
2.2.2. Polarization analysis	14
2.2.3. Sensitivity	14
<b>3. Contributions to the telescope background</b>	<b>17</b>
3.1. Background sources in Low Earth Orbit	17
3.1.1. Cosmic radiation	17
3.1.2. The South Atlantic Anomaly	18
3.2. Direct and delayed background	18
3.2.1. Direct background	20
3.2.2. Background from cosmogenic activation	20
3.3. Conclusion	23
<b>4. Simulation of the ComPol CubeSat with GEANT4</b>	<b>25</b>
4.1. Introduction to Geant4	25
4.2. General simulation settings	26
<b>5. The activation study</b>	<b>29</b>
5.1. Implementation in GEANT4	29
5.2. Activation simulation for the cosmic radiation	30
5.2.1. Activation of the CubeSat components	30
5.2.2. Activation rate after event selection	39
5.3. Activation simulation including the SAA	39
5.3.1. SAA background rates	39
5.3.2. Analysis of the non-excludable background	42
5.4. Combined results and conclusion	43

<b>6. The shielding study</b>	<b>47</b>
6.1. Shielding study for different geometries . . . . .	47
6.1.1. Analysis of remaining background events after event selection . . . . .	48
6.1.2. Shielding efficiency with the SAA background included . . . . .	53
6.1.3. Summary and conclusion . . . . .	55
6.2. Shielding study for different materials . . . . .	56
6.2.1. Choice of shielding materials . . . . .	56
6.2.2. Shielding efficiency of different materials . . . . .	58
6.2.3. Compared results for different shielding materials . . . . .	61
6.2.4. Tin shielding with the SAA background included . . . . .	63
6.2.5. Summary and conclusion . . . . .	64
6.3. Further shielding concepts . . . . .	65
6.3.1. Graded shielding . . . . .	65
6.3.2. Active veto . . . . .	68
<b>7. Summary</b>	<b>69</b>
<b>A. Appendix</b>	<b>71</b>
A.1. Rate overview . . . . .	71
A.2. Code for the Activation simulation . . . . .	72
A.3. Additional isotope charts from the activation study . . . . .	83
A.4. The SAA temporal evolution . . . . .	84
A.5. Additional figures for the shielding study with different Materials . . . . .	86
A.5.1. Attenuation of photons in different materials . . . . .	86
A.5.2. Spectra and fluorescence lines with different shielding materials . . . . .	88

# 1. Introduction

In order to retrieve information about compact astrophysical objects, like black holes, white dwarfs, and neutron stars, it is necessary to expand the observation methods beyond the border of classical imaging. Especially the small size to distance ratio makes it impossible to gain knowledge about them via optical methods. Therefore, other possibilities were developed to collect data on these objects.

The **Compton Polarimeter** (ComPol) is a CubeSat mission with the goal to investigate the spectrum and polarization of the black hole binary Cygnus X-1 over the duration of at least one year in the medium to hard X-ray range (20 keV - 2000 keV) [1]. Due to the small detector area, and hence the low amount of data to be collected in comparison with standard X-ray satellite missions, ComPol will focus its observation on only one astronomical source. The scientific goal of the mission is to gather new insights into the geometry, accretion disk properties, X-ray emission mechanisms, and further characteristics of the black hole binary system of Cygnus X-1.

A brief description of the object Cygnus X-1 is given in [section 1.1](#). The process of Compton scattering is explained in [section 1.2](#). In [section 1.3](#) the working principle of a Compton telescope and Polarimetry measurements is described.

## 1.1. Scientific motivation – Cygnus X-1

The **Black Hole Binary (BHB)** System Cygnus X-1 consists of one black hole and the blue supergiant star HDE 226868. Both objects orbit each other during an orbital period of 5.6 days [2], and the black hole continuously accretes matter from the star. The system is known to be a strong X-ray source [3] and it was the first confirmed black hole in 1972 by Bolton et al. [4]. The BHB is located in the constellation of the Swan (lat. Cygnus) in a distance of 1.8 kpc to earth [5]. The mass of the black hole is of about  $16 M_{\odot}$  and  $27 M_{\odot}$  for the companion star [6]. Like many BHBs, the X-ray spectrum of Cygnus X-1 strongly fluctuates and several different spectral states can be identified. The states are distinguished by their luminosity and their dominant X-ray energy range.

The **Low Hard State (LHS)** has an energy of maximum emission of  $\sim 100$  keV, while its overall luminosity in the X-ray spectrum is lower than in the **High Soft State (HSS)**, where the energy of maximum emission lies at  $\sim 1$  keV [7] [8]. The LHS and HSS spectra is shown in [Figure 1.1](#). While the BHB tends to remain in the hard and the soft states for several years, a far more unstable and short-lived **Intermediate State (IS)** can be occupied in between. During the last 20 years the LHS was the dominant emission state of Cygnus X-1 [7]. The LHS, as well as the HSS consist of a low energy part (0.5 keV - 10 keV), a high energy part (10 keV - 400 keV), and a hard tail for all energies above 400 keV which are differently pronounced for each state. The emission in each part can be produced by several physical processes, e.g. thermal emission, synchrotron radiation, inverse Compton scattering, etc. [1] [9]. However, the interplay of these processes and their importance are not yet sufficiently understood. The aim of the ComPol mission is to gain more insights into the production mechanisms in the different states of the system. The two main mechanisms that could be responsible for the LHS spectrum of Cygnus X-1 are listed below and shown in [Figure 1.2](#).

## 1. Introduction

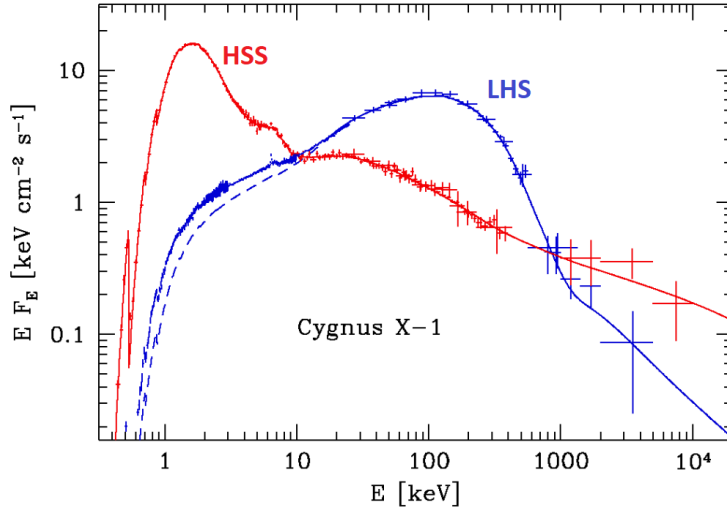


Figure 1.1.: **Cygnus X-1 spectra of the High Soft State and the Low Hard State.** The HSS is illustrated in red, the LHS is displayed in blue. The intermediate state is not shown here. The maximum emission lies at 1 keV for the HSS and 100 keV for the LHS. The Plot is adapted from [10].

- **Inverse Compton scattering** of soft photons in a hot Corona.  
Based on theoretical models, it is assumed that the black hole and the inner part of the accretion disk are surrounded by a hot corona with a thermal temperature of  $\sim 70$  keV. The photons undergo inverse Compton scattering on these electrons and hence gain energy which shifts them into the hard range of the spectrum [8].
- **Synchrotron emission** in the jets.  
The jets of a BHB consist of a small portion of matter, which does not fall into the black hole and is accelerated perpendicular to the accretion disk instead. Hard X-rays could be created due to synchrotron radiation in the jet formation region [11].

In the HSS instead, the presence of a hot corona does not match the spectral shape. Furthermore, no radio emission from jets was detected which leads to the conclusion, that there is no jet formation in the HSS [11]. Physical models without a corona and jets must be taken into account, as shown in Figure 1.3.

- **Thermal emission** of soft X-rays directly from the accretion disk.  
Since the disk can reach closer to the black hole, more soft photons can be emitted directly from the disk [1].
- **Inverse Compton scattering** on electrons, which are free falling into the black hole could be responsible for the (weak) high energy component of the HSS [12].
- **Synchrotron radiation** in the inner accretion disk generates the faint hard component of the HSS [1] [9].

For both states, the hard X-ray tail can be explained by synchrotron radiation from jets, due to their high degree of polarization [9].

In order to determine a complete model of a BHB, many further processes, e.g. geometrical and coronal effects, reflections, and relativistic effects have to be taken into account.

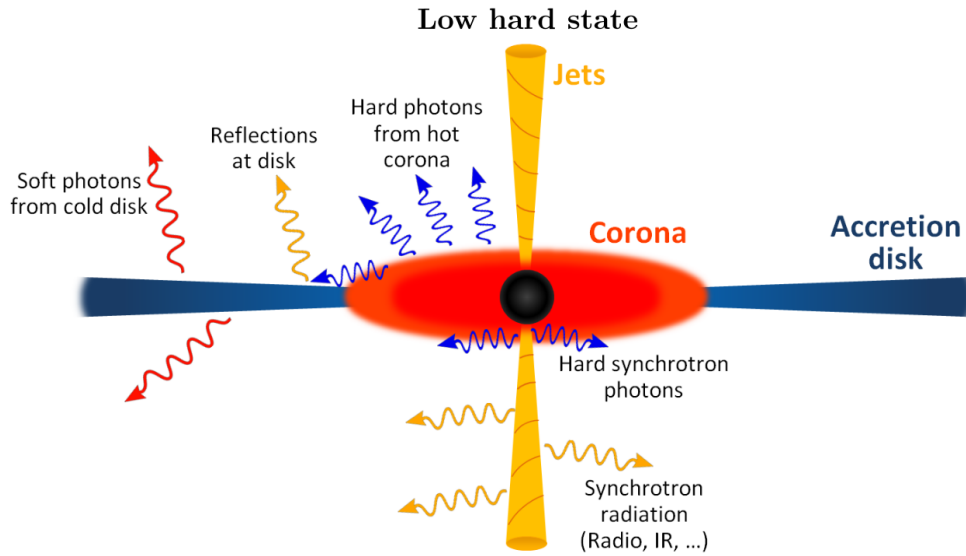


Figure 1.2.: **Illustration of a possible geometry and emission mechanisms for Cygnus X-1 in the LHS.** The black hole is indicated with a black circle in the center, while the companion star is not shown. The presence of a Corona can explain the hard emission component due to inverse Compton scattering. Additionally, hard X-rays are created in the formation region of the jets via synchrotron radiation. The figure is taken from [1].

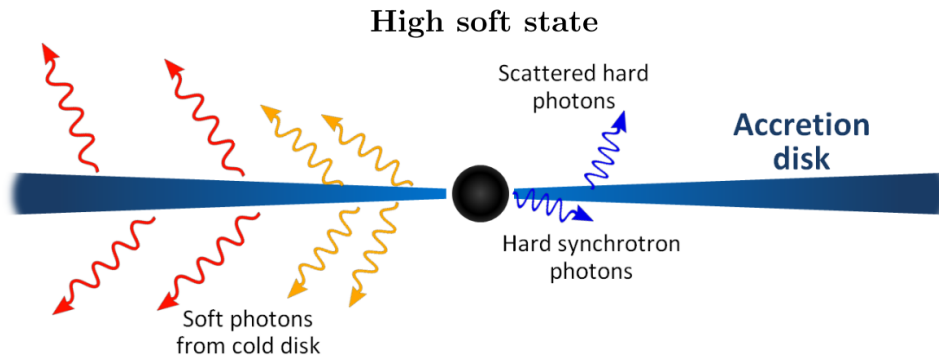


Figure 1.3.: **Illustration of a possible geometry and emission mechanisms for Cygnus X-1 in the HSS.** The black hole is indicated with a black circle in the center, while the companion star is not shown. Low energetic photons are emitted by the accretion disk, which is not covered by a corona. The hard component of the HSS is generated via synchrotron radiation in the inner parts of the accretion disk and via inverse Compton scattering on free-falling electrons. The figure is taken from [1].

Also, the mass, and spin of the black hole, and the orientation of the system play a huge role in the overall description of such a system. In the case of Cygnus X-1 are still many questions to be answered, e.g. "What are the links between the above-mentioned effects and the emitted radiation spectrum?", or "How do transition between different states work and what mecha-

## 1. Introduction

*nisms cause them?”.*

As stated in Matthias Meier’s master’s thesis [1], polarization measurements can help answer some of those open questions. Polarized radiation can be produced in a BHB via several mechanisms, namely synchrotron radiation and scattering. The degree and the plane of orientation of polarization depend on the coronal composition and the kinematics of the system. Also, the observer’s orientation to the system plays a not-insignificant role in measuring X-rays and their polarization. The alignment to the rotation axis and thus the accretion disc and the jets has an influence on the number of photons reaching the observer from each region of the BHB. By measuring not only the radiation spectrum but also the degree and plane of polarization in various energy ranges one can draw conclusions about several parameters of the astrophysical object [1].

The ComPol CubeSat will observe the spectrum of Cygnus X-1 in the energy range between 2 keV and 2 MeV, and simultaneously measure the polarization for energies up to 400 keV. After an initial sensitivity study performed by Matthias Meier, the minimum detectable polarization of ComPol after one year of data taking was determined to be 13% [1]. This is at the order of magnitude which is measured for Cygnus X-1 ( $P \leq 20\%$ ) in the energy range from 250 keV to 400 keV [13].

## 1.2. Particle Interactions

For the purpose of operating a Compton telescope, the underlying physics of Compton scattering must be understood. For an efficient analysis and background rejection, all other relevant particle interactions in the detector also have to be known. In the X-ray energy range, the most abundant interactions of photons with matter are Compton scattering and the photoelectric effect. For higher energies above 1 MeV also the process of pair production is possible. In general, the interaction probability depends on the energy of the photon and the properties of the interaction material.

### 1.2.1. Compton scattering

Compton scattering was discovered in 1923 by Arthur H. Compton [14] and the process occurs when a photon scatters inelastically on a free or nearly free electron [15]. The photon transfers some of its energy to the electron, leading to a wavelength shift  $\Delta\lambda$  and a deflection of the photon by the angle  $\theta$  which are related by the Compton formula (Equation 1.1):

$$\Delta\lambda = \lambda_C(1 - \cos\theta) \quad (1.1)$$

with  $\lambda_C = h/m_e c$ .

Klein and Nishina [16] described the differential cross-section for Compton scattering by the following formula (given in polar coordinates):

$$\frac{d\sigma_{CS}}{d\Omega} = \frac{r_0^2 \epsilon^2}{2} \left( \frac{1}{\epsilon} + \epsilon - 2 \sin^2(\theta) \cos^2(\phi) \right) \quad (1.2)$$

The ratio of the energies of the scattered and initial photon is denoted with  $\epsilon$ . The classical electron radius is given by  $r_0$ , whereas  $\theta$  and  $\phi$  stand for the scatter angle and the azimuthal scatter angle respectively. The latter describes the angle between the polarization vector  $\xi$  of the initial photon and the propagation direction of the scattered photon. A schematic of a Compton scattering process is shown in Figure 1.4. Regarding the application of Compton scattering in our CubeSat system, one has to take into account the effect of matter on

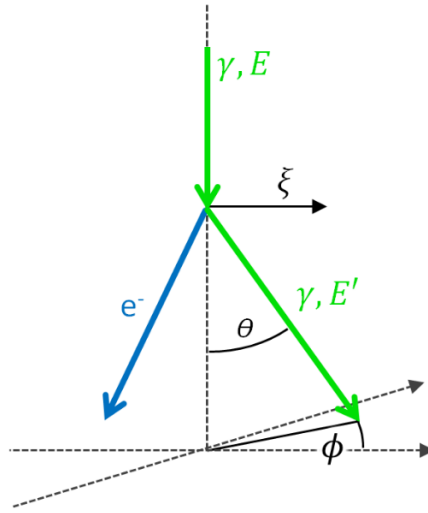


Figure 1.4.: **Sketch of a Compton scattering process.** An incoming photon (green) with Energy  $E$  and polarization vector  $\xi$  scatters on an electron (blue) and gets deflected by the angle  $\theta$ . After the scattering process, the photon has the energy  $E'$ . The azimuthal scatter angle between the polarization vector  $\xi$  and the outgoing photon direction is indicated with  $\phi$ . The figure is taken from [1].

scattering processes. Since electrons are bound to atoms and not completely free, classical Compton scattering does not apply here. Instead, the process of *incoherent scattering* has to be considered. Incoherent scattering differs from classical Compton scattering by adding the *incoherent scattering factor*  $S$  to the differential cross-section, as shown in Equation 1.3:

$$\frac{d\sigma_{IS}}{d\Omega} = \frac{d\sigma_{CS}}{d\Omega} \cdot S(E, \theta) \quad (1.3)$$

This correction factor  $S$  depends on the initial energy of the photon  $E$  and the material in which the scattering process happens. This can be translated to a dependence on the momentum transfer and resulting in a dependency on the scatter angle  $\theta$ . The difference between Compton scattering and incoherent scattering is most pronounced at low energies and small scatter angles [16]. However, it is more common to use the term *Compton scattering* for both processes, which will also be applied in this work.

### 1.2.2. The photoelectric effect

Besides Compton scattering, the photoelectric effect also plays a huge role in the X-ray energy range. Hereby a photon gets absorbed by the electron shell of an atom and an electron is ejected from the shell. This can only happen when the energy of the photon exceeds the binding energy of the electron, and thus is more dominant for weakly bound electrons in high shells. Hence, the cross-section for the photoelectric effect scales with  $Z^5$  and  $E^{-3.5}$  this process is most prominent in high  $Z$  elements and at low energies [1].

### 1.2.3. Pair production

The process of pair production becomes relevant for higher energetic photons above 1 MeV. An electron and a positron are created from a photon in the vicinity of a nucleus. The minimum

## 1. Introduction

photon energy lies at 1022 keV, which is the sum of the rest masses of the produced positron and electron. It plays no significant role in the energy range investigated in this thesis [1].

### 1.3. Compton Telescopes

The process of Compton scattering is taken advantage of in Compton telescopes. These instruments are capable of measuring the energy spectrum, position, and polarization of X-ray sources. By measuring the position of the initial Compton interaction in the detector, as well as the energy deposits of the scattered X-ray, the direction of motion of the scattered photon can be determined. On the basis of this so-called *event reconstruction*, a further polarization analysis can be conducted. The ComPol telescope follows the working principle of the simplest type of Compton telescope, the COMPTEL type [17].

#### 1.3.1. Working principle of a Compton telescope

The detector system consists of two energy- and position-sensitive detectors, which are arranged in a stacked order. A Compton event consists of one interaction in the first detector, where the photon undergoes Compton scattering at position  $R_1$  and transfers the energy  $E_1$  to the electron. Afterward, the X-ray has a consecutive interaction in the second detector at position  $R_2$  where the photon gets completely absorbed via photo effect and deposits the energy  $E_2$  [1] [17]. The second detector acts as a calorimeter and usually, a scintillating material is chosen for this purpose. A sketch of the COMPTEL type detector system and a useful Compton event is shown in Figure 1.5. By means of the Compton formula Equation 1.1, one can calculate the scatter angle  $\cos \theta$ :

$$\cos \theta = 1 - m_e c^2 \left( \frac{1}{E_2} - \frac{1}{E_1 + E_2} \right) \quad (1.4)$$

The wavelength shift  $\Delta\lambda$  was expressed in terms of energy here, and  $E_1 + E_2 = E$  is the initial photon energy [1]. With the knowledge of the scatter angle, the initial direction of the X-ray can be confined to a cone surface with an opening angle of  $2\theta$ . Since a COMPTEL type Compton telescope cannot resolve the direction of the recoil electron, the initial direction cannot be confined any further. A more elaborate description of the working principle of Compton telescopes can be found in the doctoral thesis of Andreas Zoglauer [17]. In order to confine the position of an X-ray source precisely, a significant number of Compton events have to be measured and the intersection point of all resulting Compton cones has to be calculated. This system can observe the entire solid angle of  $4\pi$  and is called a Compton camera [1].

By artificially restricting the observation to one specific direction, the above mentioned position reconstruction is not needed anymore. This is done by aligning the telescope towards one source and adding a collimator in front of the detector system [1]. The number of Compton events from other directions is therefore suppressed. The process to distinguish useful Compton events from Cygnus X-1 from background events is called *event selection* and it will be described for ComPol in subsection 2.2.1.

#### 1.3.2. Polarimetry

A Compton telescope can also be used to measure the degree of polarization  $P$  and the dominant polarization plane of an X-ray source. Hereby it is necessary to average over all measured photons [17]. As shown in Equation 1.2 and Equation 1.3 describing the cross-section for Compton scattering, and incoherent scattering respectively, the cross-section is

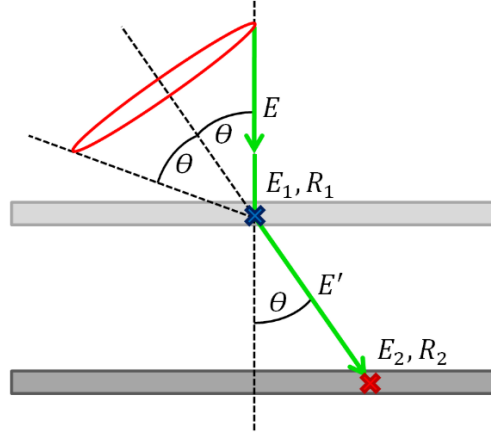


Figure 1.5.: **Schematic illustration of a COMPTEL type Compton telescope with an exemplary useful Compton event.** The first interaction of the X-ray (green) is a Compton scattering process in the upper detector where the Energy  $E_1$  is deposited at the position  $R_1$ . In the second detector, the photon is fully absorbed in the position  $R_2$  and deposits the energy  $E_2$ . By detecting the positions and energy deposits and applying Equation 1.4 it is possible to confine the origin of the initial photon to a cone surface with an opening angle of  $2\theta$ . The figure is taken from [1].

maximum for scatter angles of  $\phi = 90^\circ$  and  $\phi = 270^\circ$ . This translates to:

1. An increased probability for the photon to be scattered in a direction, which is orthogonal to the initial polarization vector.
2. For small scatter angles and scatter angles close to  $180^\circ$ , the detectable polarization signature is weak ( $\sin^2 \theta$  is close to zero).
3. At higher energies the scatter angle is smaller on average, leading to a weaker dependence on the polarization as well.

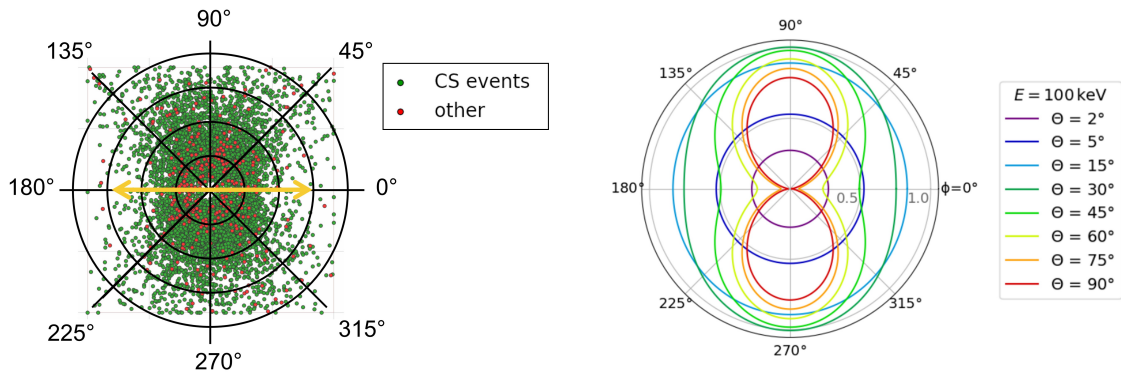
A sketch of the polarization dependence is given in Figure 1.6.

From Equation 1.3 the probability distribution for the azimuthal scatter angle can be calculated. Since the real azimuthal scatter angle  $\phi$  in the reference frame of the initial X-ray is not known, an arbitrary new scatter angle  $\Phi$  toward a fixed reference frame in the detector system is introduced [1]. The probability distribution for this new scatter angle can be expressed as follows [18]:

$$f_P(\Phi) = C \cdot [1 + a \cos(2(\Phi - \psi))] \quad (1.5)$$

As shown in Figure 1.7, the parameter  $C$  describes the offset of the azimuthal scatter angle distribution and is related to the total number of events. The modulation amplitude  $a$  describes the amplitude of the cosine curve and is calculated by the ratio of the absolute amplitude  $A$  and the offset  $C$ . The value of  $a$  has to lie between 0 and 1. The angle  $\psi$  describes the polarization angle in the reference frame of the instrument and leads to a shift along the x-axis of the probability distribution. With Equation 1.6 it is possible to calculate the degree

## 1. Introduction



(a) Interaction points of all remaining events after event selection in the second detector. (b) Polar plot of the differential cross-section for the incoherent scattering in silicon.

Figure 1.6.: **Interaction points in the detector and sketch of the polarization dependence.** a) The interaction points in the second detector of all remaining events after event selection of 10 keV to 300 keV photons from the signal simulation of the Cygnus X-1 spectrum are shown in green. Additionally, a few non-Compton events are marked in red. A polar coordinate system is overlayed to show the polarization dependence of Compton scattering. The initial polarization of the 100% polarized beam was chosen to be along the orange arrow. b) Polar plot of the differential cross-section for the incoherent scattering of 100 keV photons in silicon. The dependence of the cross-section on the azimuthal scatter angle  $\phi$  for a specific scatter angle  $\theta$  is shown in different colors. The radial distance to the midpoint corresponds to the amplitude in barn/atom. The polar plot was taken from [1].

of Polarization  $P$  by dividing the measured modulation amplitude  $a$  with the modulation amplitude for 100% polarized light  $\mu$ :

$$P = \frac{a}{\mu} \quad (1.6)$$

The modulation amplitude for 100% polarized light  $\mu$  depends on the used instrument and has to be determined experimentally via a calibration measurement.

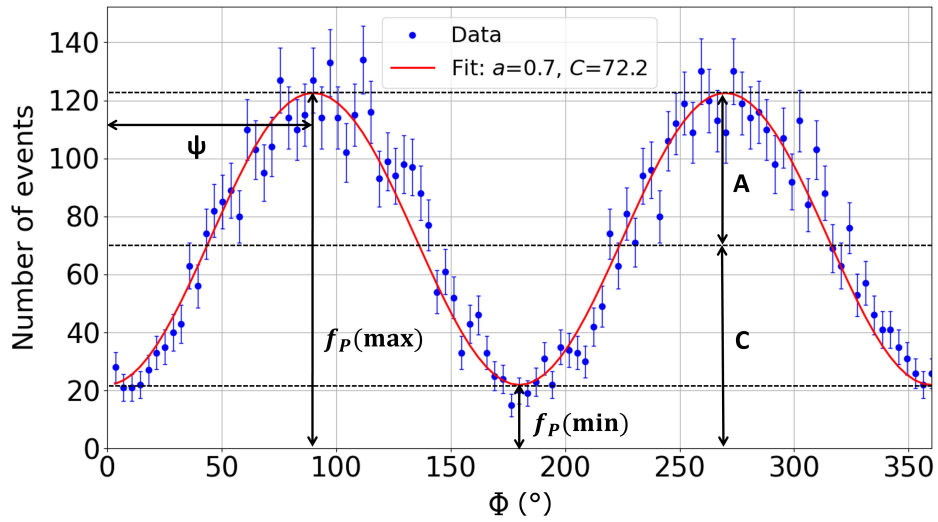


Figure 1.7.: **Exemplary data and fit of the cosine modulation of the azimuthal scatter angle distribution for polarized photons.** The parameter of the absolute amplitude  $A$ , the offset  $C$ , and the polarization angle  $\psi$  in the reference frame of the instrument are also drawn. The amplitude  $A$  is proportional to the degree of polarization, while the polarization angle  $\Phi$  corresponds to the plane of polarization.



## 2. The ComPol mission

The ComPol mission is designed as a CubeSat mission with a detector system consisting of two detectors with different purposes. In the following [section 2.1](#) the satellite properties, as well as both detectors will be described separately.

The exact procedure of data analysis for ComPol is described in Matthias Meier's master thesis [1]. It will nevertheless be summarized in [section 2.2](#).

### 2.1. The ComPol CubeSat

The Compton telescope ComPol will be built as a CubeSat (Cube Satellite). A CubeSat is a small and lightweight alternative to a standard satellite mission and is extensively used in order to test and verify new equipment and detection mechanisms in space. The Cube Satellites can be quickly and easily assembled following standardized size and payload units. They are launched in huge quantities at once by commercial institutions into a wide range of low earth orbits. The satellite equipment, the holding structure, and the launch service can be bought from the shelf. This makes the CubeSat an excellent tool for universities and student groups to conduct their own experiments and tests in space.

While CubeSats are usually only used for in-orbit verifications for later missions and do not gain any scientific knowledge on their own, the ComPol CubeSat is already designed to conduct measurements of scientific interest on an astrophysical object (Cygnus X-1) (see [section 1.1](#)). Being able to do research with a relatively small and minimalistic telescope in a CubeSat will be a great achievement.

The ComPol CubeSat will consist of 3 CubeSat Units. One unit has the standardized size of  $10 \times 10 \times 11.35 \text{ cm}^3$  and maximal weight of 1.3 kg [19], which would translate to a size of  $10 \times 10 \times 34 \text{ cm}^3$  and weight of 3.9 kg for ComPol. Due to the strong limitation in size and weight, most of the heavy shielding material must be omitted. This makes the satellite sensible to cosmic radiation, and dust particles, which relatively quickly degrade the electronics and shorten the lifetime of the satellite. A typical lifetime for a CubeSat is estimated at 1 year in Orbit.

The detector system for the Compton events consists of a **Silicon Drift Detector (SDD)** in which the Compton scattering takes place. Underneath this first detector, the scattered photons are absorbed in a  $\text{CeBr}_3$  scintillator operated as a calorimeter. A schematic of the setup with an exemplary Compton interaction is shown in [Figure 2.1](#). Both detectors are thoroughly described in Matthias Meier's master thesis [1]. The most important characteristics are summarized in the following subsections ([subsection 2.1.1](#) for the SDD and [subsection 2.1.2](#) for the calorimeter).

#### 2.1.1. The SDD detector

The SDD was developed for the TRISTAN project of the KATRIN experiment [20] for sterile neutrino search at Karlsruhe Institute of Technology. The SDD module for ComPol has dimensions of  $10 \times 12.7 \text{ mm}^2$  and a height of 0.4 mm. The exterior dimensions of the SDD are also shown in [Figure 2.1](#) and [Figure 2.2](#). The SDD module for ComPol will consist of a

## 2. The ComPol mission

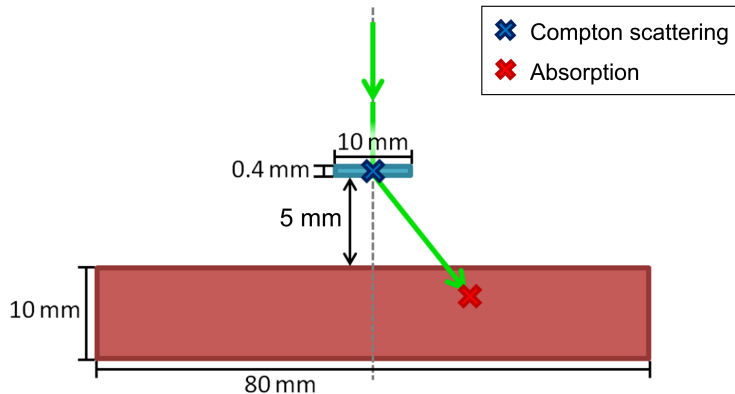


Figure 2.1.: **Detector setup of the ComPol CubeSat.** The setup consists of the TRISTAN SDD (blue) and the  $\text{CeBr}_3$  scintillator in red. It is shown with an exemplary Compton event in the SDD (blue cross) and subsequent full absorption in the calorimeter (red cross). Both detectors have approximately a quadratic base (the 3<sup>rd</sup> dimension is not shown here). The indications of size are preliminary. The figure was adopted from [1].

31-pixel detector. A drawing of the module as well as a photo of a smaller 7-pixel TRISTAN SDD detector can be seen in Figure 2.2. The TRISTAN SDD detector can handle a count rate of up to 100 kcps per pixel and has an excellent energy resolution of 139 eV FWHM at 5.9 keV at  $-30^\circ\text{C}$  [21]. These are good prerequisites for the ComPol project. For an efficient background rejection, the energy deposition during the Compton scattering event has to be measured as accurately as possible. The energy resolution of the SDD can be described by the Fano noise [22] and the noise originating from the detector electronics and the readout chain [23]. The lower detection threshold is set at 1 keV. The position resolution of the SDD is restricted by the pixel size of 2 mm.

### 2.1.2. The $\text{CeBr}_3$ detector

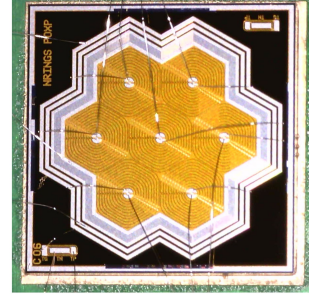
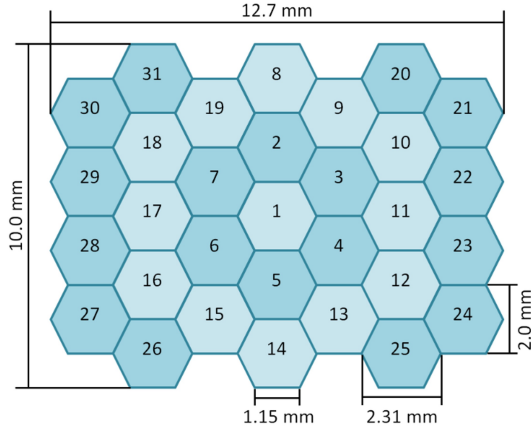
The calorimeter is made of the scintillating materials  $\text{CeBr}_3$  with a maximum emission at 380 nm [24]. It will be read out by an array of 64 Silicon Photomultipliers. The measured scintillation light distribution depends on the position of the interaction and the energy of an incoming photon in the detector. The readout system to reconstruct the interaction point was developed at Université Paris-Saclay and is based on a neural network [25].

The calorimeter has a quadratic base with a side length of 80 mm and a height of 10 mm. The dimensions of the  $\text{CeBr}_3$  are also shown in Figure 2.1.

The spacial resolution of the  $\text{CeBr}_3$  detector is limited to 2.5 mm parallel to the detector plane and 2.2 mm in the vertical dimension (height of the detector). The lower energy threshold of the calorimeter is 10 keV and the overall energy resolution can be calculated on the basis of measurements with various radioactive sources in [25]. The FWHM at 59.5 keV ( $\gamma$   $^{241}\text{Am}$ ) is determined to be 10.5 keV.

## 2.2. Data analysis for ComPol

The scientific goal of the ComPol mission is to gain more information about the degree and plane of polarization of Cygnus X-1 (see section 1.1). The best results can be achieved by



(a) Preliminary geometry of the SDD

(b) Seven-pixel prototype of the TRISTAN SDD

Figure 2.2.: **The SDD in the ComPol setup.** a) A schematic view of the preliminary SDD geometry. The module consists of 31 hexagonal pixels with a size of 2 mm each. The figure is taken from [1]. b) Seven-pixel prototype of the TRISTAN SDD. The pixels of the shown prototype have the same dimensions as the ones in the sketch on the left.

suppressing the rate of background events compared to the rate of signal Compton events from the astrophysical source as efficiently as possible. This background reduction is done by external shielding, as described in [chapter 6](#) and via a selection process that is implemented in python. The full process of background rejection is called *event selection* and is summarized in [subsection 2.2.1](#). The selected events then undergo the Polarization analysis ([subsection 2.2.2](#)). Using the Monte Carlo truth from simulations, the origin of the remaining events is known. A final signal and background rate can be obtained and a final value for the sensitivity of the Compton telescope can be determined ([subsection 2.2.3](#)).

### 2.2.1. Event selection

The only useful event for the polarimetry analysis is the Compton scattering in the SDD with complete absorption of the scattered X-ray in the calorimeter. All other interactions from X-rays originating from Cygnus X-1 or a background source cannot be used for the polarimetry analysis. The majority of these events will be identified as background events and rejected. The event selection process rejects background event in several stages:

1. **Coincident events:**

Only events with interactions in both detectors at the same time will be taken into account for further analysis

2. **Energy range of interest:**

The sum of energies that are deposited in both detectors does not exceed 300 keV. The probability for Compton scattering is highest in the energy range of 20 keV to 300 keV. The lower energy threshold for acceptance is defined by the detector thresholds and set at 11 keV.

$$11 \text{ keV} < E_{\text{SDD}} + E_{\text{Cal}} < 300 \text{ keV} \quad (2.1)$$

3. **Selection of Compton events:**

Two different methods of calculating the scatter angle theta are used to select the

## 2. The ComPol mission

Compton events. The first method is a geometrical calculation of the scatter angle  $\theta_{\text{Pos}}$ . For this, it is necessary to know the interaction points in the SDD  $R_{\text{SDD}}$  and the calorimeter  $R_{\text{Cal}}$ , as well as the geometric assembly and orientation towards the source. Additionally, the cosine of the scatter angle  $\theta_{\text{E}}$  can be calculated via the Compton formula [Equation 1.4](#) and the detected energy deposits  $E_{\text{SDD}}$  and  $E_{\text{Cal}}$  in both detectors. If the event is a useful Compton event both obtained scatter angles are equal and the following relation is valid:

$$\Delta\theta = \theta_{\text{Pos}}(R_{\text{SDD}}, R_{\text{Cal}}) - \theta_{\text{E}}(E_{\text{SDD}}, E_{\text{Cal}}) = 0 \quad (2.2)$$

An exemplary distribution for  $\Delta\theta$  is shown in [Figure 2.3a](#). For Compton events the  $\Delta\theta$  peaks around 0. Due to the energy and position resolution of the detector system, there is a tolerance area applied around 0 where events are still accepted as Compton events (shown with dashed lines). The general acceptance region for all performed analyses in this thesis was set in the following range:

$$\Delta\theta \in [-26.0^\circ, 13.0^\circ] \quad (2.3)$$

### 4. Selection of events with large scatter angle:

As it can be seen in [Equation 1.2](#) and [subsection 1.3.2](#), the modulation of the distribution of the azimuthal scatter angle  $\Phi$  is strongest for large Compton scatter angles  $\theta$ . Therefore, another cut on the scatter angle is applied, to define the lower limit of the acceptance range. The scatter angle is defined by the geometries of the detector system. The acceptance region for  $\theta$  is

$$\theta \in [55.0^\circ, 83.0^\circ] \quad (2.4)$$

An exemplary distribution for  $\theta$  is shown in [Figure 2.3b](#). For Compton events, the measurable polarization signal is highest for large  $\theta$ . The dashed line shows the cut on the scatter angle. It is noted, that the curve of the Compton events is smoother than the one for the background events. This is due to the different simulation times of the Cygnus X-1 signal compared to the background (see [section 4.2](#)).

### 2.2.2. Polarization analysis

All events, which pass the event selection undergo the polarization analysis afterward. The cosine modulation of the azimuthal scatter angle  $\Phi$  is plotted and fitted with [Equation 1.5](#) which was described in [subsection 1.3.2](#) (Polarimetry). Since the signal simulation was performed with 100% polarized light, the modulation amplitude  $a$  corresponds to the maximal modulation amplitude  $\mu$ . After normalizing the data to the expected observation time of Cygnus-X1, the signal rate  $R_{\text{S}}$  can be calculated.

The remaining background events, which were falsely accepted are unpolarized and will only contribute as a flat background to the modulation amplitude. After normalizing the data accordingly, the background distribution will therefore be fitted with a flat function, whereof the rate of remaining background events  $R_{\text{BG}}$  can be determined.

The rates, as well as the polarization parameter  $\mu$ , are used in the next chapter about the polarization sensitivity.

### 2.2.3. Sensitivity

The final sensitivity of the ComPol telescope can be estimated with the knowledge obtained, the simulation of signal and background events and the event selection and polarization analysis afterward.

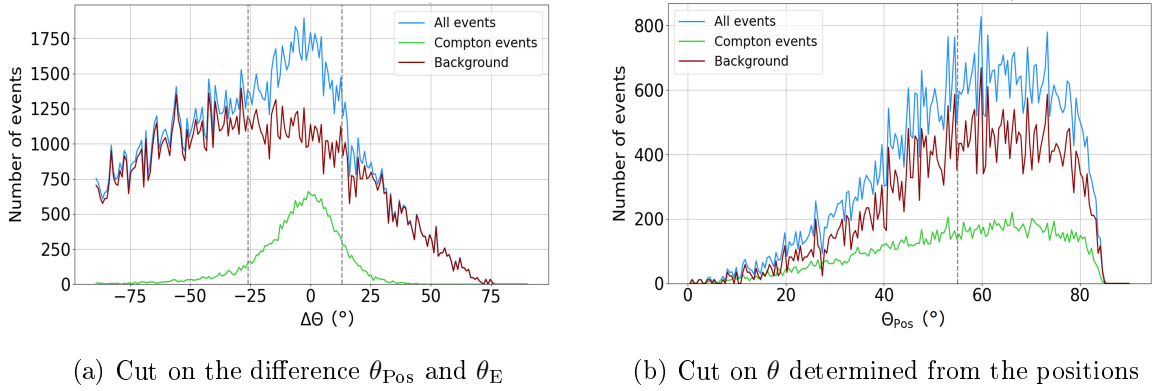


Figure 2.3.: **Distribution of  $\Delta\theta$  and  $\theta_{\text{Pos}}$ .** a) Exemplary distribution of  $\Delta\theta$  which is calculated using Equation 2.2. The sum of background events is shown in red, while the Compton events are shown in green. The sum of both is shown in blue. The Compton events are distributed around  $\Delta\theta = 0$ . The cuts on  $\Delta\theta$  are indicated with dashed lines. The region within the dashed lines will be processed in the next step of event selection. b) Exemplary distribution of  $\theta$ . Again the background events (red), the Compton events (green), and all events (blue) are shown. The cut on  $\theta$  is indicated with a dashed line. All events, which lie at angles above the dashed line will be used for the polarization analysis.

A first estimation on an instrument's sensitivity is commonly performed by the calculation of the **Signal to Noise Ratio (SNR)**. It is defined as the ratio of the signal to the background rate:

$$\text{SNR} = \frac{R_S}{R_{\text{BG}}} \quad (2.5)$$

In order to give an estimation on the sensitivity on the degree of polarization for the instrument, the **Minimum Detectable Polarization (MDP)** is used. The MDP describes the polarization sensitivity to a 99% confidence level [26]. It can be calculated as follows:

$$\text{MDP} = \frac{4.29}{\mu \cdot R_S} \left( \frac{R_S + R_{\text{BG}}}{T} \right)^{1/2} \quad (2.6)$$

The observation time is labeled with  $T$  and the modulation amplitude for 100% polarized light  $\mu$  which was introduced in Equation 1.6.

The SNR and the MDP will be used for all simulations performed in this thesis to serve as parameters to evaluate the sensitivity of the instrument in the respective configuration. The MDP is hereby always given after 0.5 years, which corresponds to an estimated observation time of Cygnus X-1 within a one-year mission. The exact observation time is orbit dependent and not calculated yet.



## 3. Contributions to the telescope background

The goal of this thesis is to improve the signal-to-noise ratio and accordingly the overall sensitivity of the ComPol instrument. This is done by optimizing the shielding strategy of the detector system. In order to conduct a thorough analysis of the shielding properties, all relevant background sources and the resulting particle interactions with the CubeSat material have to be known.

In the following [section 3.2](#) the main background sources for the telescope are presented. In the next [section 3.2](#) the interaction possibilities of background particles in the detectors and their effects on the total telescope background are explored.

### 3.1. Background sources in Low Earth Orbit

The background for a satellite in **Low-Earth Orbit (LEO)** consists of two main sources. The cosmic radiation background, which will be discussed further in [subsection 3.1.1](#), and the background due to the South Atlantic Anomaly (see [subsection 3.1.2](#)).

#### 3.1.1. Cosmic radiation

The background spectrum in LEO depends mainly on the altitude and inclination of the spacecraft's orbit and the solar activity during mission time. The spectrum consists of primary and atmospheric cosmic particles, namely photons, protons, electrons, positrons, neutrons, and alpha particles. Primary particles originate directly from cosmic sources, while atmospheric particles are secondary particles created by interactions of primary cosmic particles in the earth's atmosphere. Neutrons are only generated in the atmosphere, hence they are called atmospheric neutrons. For the ComPol mission, the background spectrum of all charged particles, as well as the photon spectrum was taken from Cumani et al. [27] and the model for the atmospheric neutron spectrum was taken from Kole et al. [28]. They are based on measurements with various satellite, balloon, and high altitude aircraft missions. In both sources, an altitude of 550 km height at an inclination of  $0^\circ$ , and an average solar activity halfway between minimum and maximum were assumed.

The spectra for all charged particles is determined in an energy range from 1 MeV up to 100 GeV and consist of the sum of all primary cosmic particles, and all secondary particles, which are generated in the atmosphere. For the photon spectrum, an energy range from 10 keV to 10 GeV was investigated. The total photon spectrum consists of extragalactic photons, photons originating from the galactic center and disk, and albedo photons created by the atmosphere. The neutron spectrum is given in the energy range from 0.01 eV to approximately 30 GeV and consists of neutrons, generated by the interaction of cosmic rays with the atmosphere. The full background spectrum is shown in [Figure 3.1](#). The cosmic radiation is assumed to be constant and isotropic and therefore is independent of the position or orientation of the satellite during its orbit.

### 3. Contributions to the telescope background

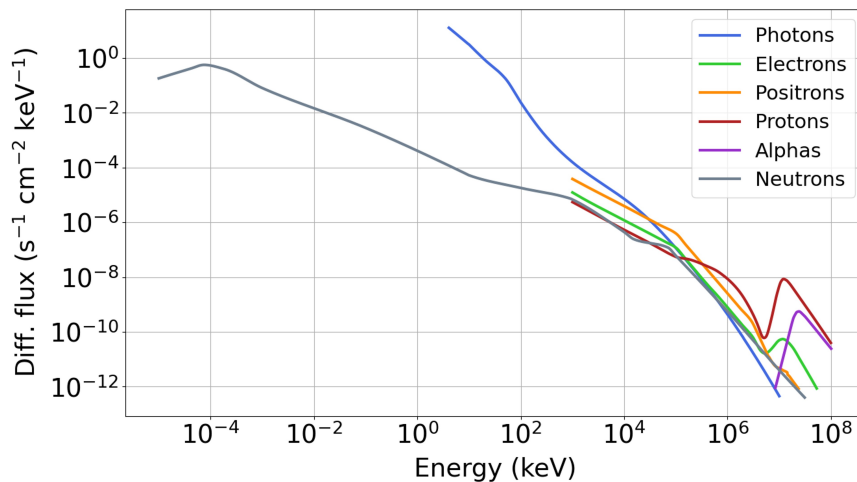


Figure 3.1.: **Spectrum of the cosmic background in LEO.** The spectra are taken from [27].

#### 3.1.2. The South Atlantic Anomaly

Additional to the cosmic radiation background, the background from the South Atlantic Anomaly has to be taken into account. The South Atlantic Anomaly is a region above the South Atlantic, where the inner Van Allen Belt reaches close to the earth's surface and leads to an increased flux of charged particles in LEO. When passing through this area, the CubeSat will be exposed to intense proton and electron radiation causing an increased background [27]. The flux was obtained with the AP-8 and AE-8 models, which consist of maps that contain the omnidirectional, integral electron (AE maps), and proton (AP maps) fluxes in the energy range of 0.04 MeV to 7 MeV for electrons and 0.1 MeV to 400 MeV for protons in the Earth's radiation belt. The proton and neutron fluxes are illustrated in Figure 3.2. Charged particles are guided along the magnetic field lines towards the poles. This can be seen in the increased electron flux above the polar regions where the outer electron belt reaches close to the earth surface as well [29]. For this work, both regions with increased electron flux were added together and taken into account.

The spectrum of SAA-protons and -electrons depends strongly on the orbit parameters of the satellite. The impact of the SAA is increased for orbits with high inclination, defined as nearly polar, or polar orbits. In order to estimate the impact of the SAA on the ComPol CubeSat, a worst-case orbit with an inclination of  $85^\circ$  is chosen. The altitude of the CubeSat is set to 550 km. The CubeSat will fly through the SAA multiple times a day with varying degrees of SAA interference per orbit. The average proton and electron spectrum was obtained with the SPENVIS website [30] and is shown in Figure 3.3 in comparison to the cosmic background spectra for protons and electrons.

## 3.2. Direct and delayed background

Both background sources discussed above have a direct and immediate influence on the overall background rate, as well as a time-delayed effect due to cosmogenic activation. These two differing contributions are discussed in subsection 3.2.1 and subsection 3.2.2.

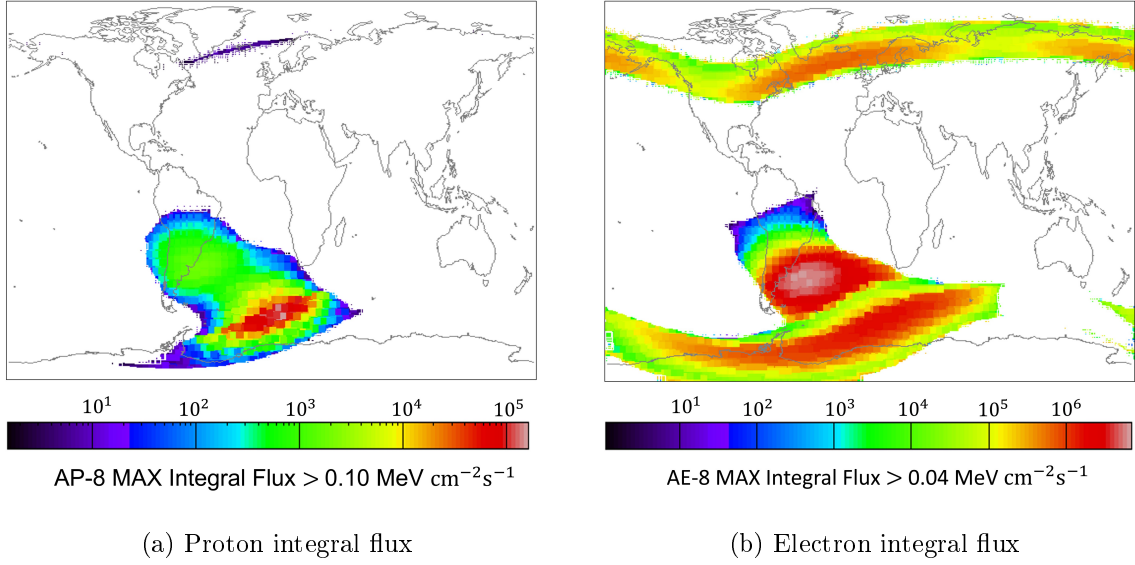


Figure 3.2.: **Regions of increased flux of charged particles.** a) Increased proton flux in the South Atlantic Anomaly obtained with the AP-8 model. The flux is indicated by the colormap and exceeds the cosmic proton flux by up to 5 orders of magnitude. b) Increased electron flux in the South Atlantic Anomaly obtained with the AE-8 model. An increased electron flux can also be seen above the polar regions. For this work, both regions with increased flux were added together and taken into account. The flux is indicated by the colormap and exceeds the cosmic electron flux by up to 6 orders of magnitude.

The figures were generated using the SPENVIS website [30].

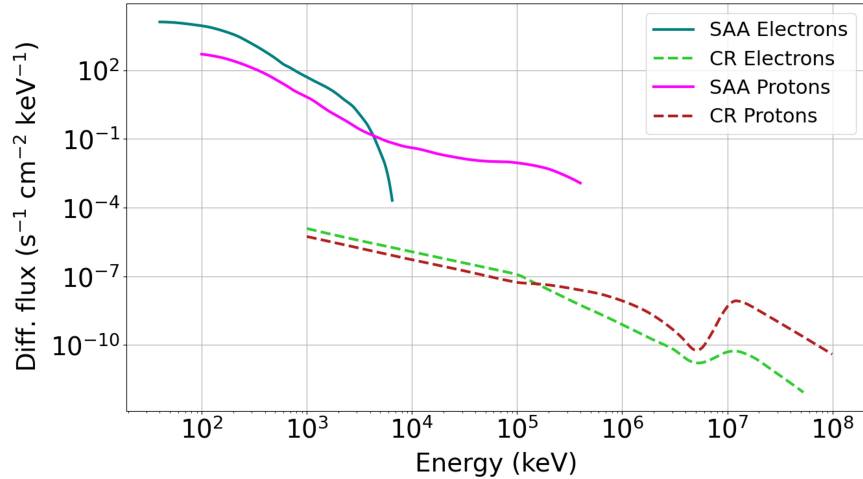


Figure 3.3.: **Electron and proton spectra in the SAA.** The two solid lines correspond to the electron and proton energy spectrum in the SAA. These spectra were generated using the SPENVIS website [30]. The two dashed lines are drawn for comparison with the normal spectrum of cosmic rays (see subsection 3.1.1). The cosmic background spectra are taken from [27].

### 3. Contributions to the telescope background

#### 3.2.1. Direct background

Both background sources described in the two sections above contribute to the overall background of our instrument via direct interactions of the respective particles in the detectors. This also includes immediate interactions of elsewhere-produced secondary particles. The background rate is hereby dependent on the interaction cross-sections of the particles with the detector materials in the respective energy range.

The cosmic radiation creates a constant background rate due to these direct interactions. Whereas the direct interactions induced by the SAA only contribute while the satellite passes the SAA. During these passages, the direct background rate is normally too high to gain scientific data and the observation is usually stopped during this time frame [27].

#### 3.2.2. Background from cosmogenic activation

Furthermore, interactions of cosmic particles in the material of the satellite create radioactive isotopes via activation processes. The decay of these isotopes causes an additional time-delayed background in our detectors which will be analyzed in detail in [chapter 5](#). The underlying processes, causing cosmogenic activation and their decay processes are explained in the following paragraphs.

##### Cosmogenic activation

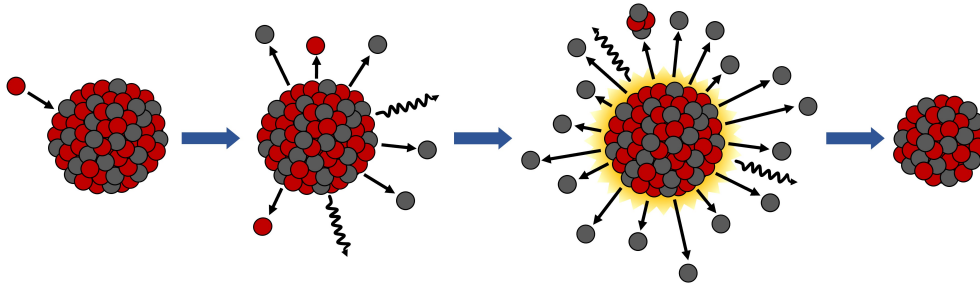
The CubeSat will be constantly exposed to cosmic rays. This includes protons, neutrons, photons, electrons, positrons, and to some extent also alpha particles and heavier ions. This exposure to cosmic radiation leads to an activation of the material inside the satellite. The process of creating radioactive isotopes or excited nuclei due to cosmic rays is referred to as *cosmogenic activation*.

One of the most dominant processes for cosmogenic activation is the spallation of nuclei by highly energetic nucleons [31]. Herby, during the impact of the cosmic particle the target nucleus will be split into two or more, smaller residual nuclei with atomic numbers far from the target nucleus [32]. The remnant nuclei can be left in an excited state and subsequently decay radioactively after their specific lifetime. The generated radioisotopes depend on the target material and can be very diverse. Tritium is one common spallation product and is frequently produced [31]. A schematic illustration of the spallation process is shown in [Figure 3.4a](#).

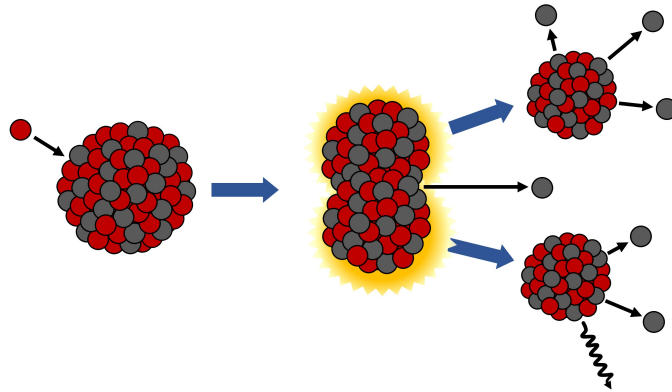
Another important process for cosmogenic activation is nucleon capture. This is an inelastic nuclear reaction in which one or more nucleons collide and then merge with a nucleus. The then heavier nucleus is usually left in an excited state and decays radioactively [33]. Capture reactions are often caused by low energetic neutrons which are created in the atmosphere. Additionally, exchange reactions can occur. In this case, a proton or neutron is captured by the target nucleus while another nucleon is ejected. If the type of the ejected nucleon differs from the captured one, the process is called exchange reaction [34].

Concerning high  $Z$  materials also fission needs to be considered. In contrast to spallation, the target nucleus breaks into only two large residual nuclei when hit by highly energetic neutrons or charged particles. Usually, a lighter (mass number around 90) and a heavier fission fragment (mass number around 140), and a few neutrons are produced. A fission process is sketched in [Figure 3.4b](#).

The released energy during spallation and fission is released through a high kinetic energy of the residual nuclei and neutrons. These fragments are slowed down in the surrounding material and can trigger new nuclear reactions as well. Other reactions like fragmentation or break-up also contribute to the creation of radioactive isotopes. Cosmogenic activation is



(a) Schematic drawing of a spallation process



(b) Schematic drawing of a fission process

Figure 3.4.: **Sketches of processes generating activated nuclei.** The protons are illustrated in red and the neutrons are drawn in grey. **a)** shows an example for a spallation process. The target nucleus emits neutrons and protons immediately after the interaction with the cosmic proton and is left in an excited state. This leads to the evaporation of further nucleons (mostly neutrons). **b)** depicts an exemplary fission process. The target nucleus is divided into two smaller nuclei with roughly equal size and emits a few fast neutrons, which could trigger further fission reactions.

### 3. Contributions to the telescope background

consequently dominated by hadrons [35].

Additionally, the production rate of radioactive isotopes depends on the energy of the initial cosmic hadrons, and particle energies in the MeV to GeV scale are most responsible for cosmogenic activation. Given that the hadronic cosmic ray spectrum in this energy range is dominated by protons and neutrons at low earth orbit, protons and neutrons are the dominant sources for activating the Cube Sat's material. Heavy ions do not play a significant role in cosmogenic activation [31].

The activity  $A$  of a certain material after an exposure time  $t_{\text{exp}}$  and a cool-down time  $t_{\text{cool}}$  can be calculated as follows:

$$A = \lambda N \cdot e^{-\lambda t_{\text{cool}}} = R(1 - e^{-\lambda t_{\text{exp}}}) \cdot e^{-\lambda t_{\text{cool}}} \quad (3.1)$$

The decay constant  $\lambda$  and the production rate  $R$  are both material dependent. The number of activated nuclei after the exposure time  $t_{\text{exp}}$  is given with  $N$ . The production rate  $R$  depends on the flux of initial activating particles  $\varphi$ , and the isotope production cross-section  $\sigma_a$ , being both dependent on the particle energy  $E$ . The production rate can be calculated as follows:

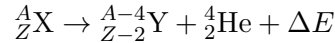
$$R = N_0 \int \varphi(E) \sigma_a(E) dE \quad (3.2)$$

Since the decay constant, and the production rate are isotope dependent, Equation 3.1 is only valid for one particular isotope. However, in every material a natural mixture of different isotopes occurs with a certain probability distribution for each isotope. The total activity of a material consists of the sum of the activity of each isotope weighed by its relative proportion [34].

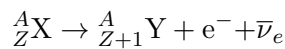
#### Radioactive decays and decay chains

The radioactive decay of the previously generated unstable isotopes can cause an additional background in the detector system. Especially, the short, and medium living isotopes with lifetimes ranging from seconds to days or weeks contribute to this additional background. (Very) long living isotopes with lifetimes of more than one year will decay mostly long after the expiration of the ComPol mission, and hence do not contribute as a background source. All relevant decays are summarized below [36]:

- **$\alpha$ -decay:** A nucleus emits a  ${}^4_2\text{He}$ -nucleus which is also called  $\alpha$ -particle. Unlike other types of decay,  $\alpha$ -decay as a process is confined to a minimum-size atomic nucleus that can support it [34].



- **$\beta^-$ -decay:** A weak process during which a neutron is converted into a proton. An anti-neutrino and an electron are emitted during this conversion. They share the released energy. Therefore, the process is a three-body interaction and thus, their energy distribution follows continuous spectra. Below, the decay is depicted in a reaction equation, and furthermore, the changes in the atomic number  $Z$ , and the mass number  $A$  are shown.

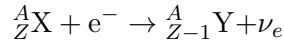


Tritium is an abundant product generated by cosmogenic activation it is highlighted here as a pure  $\beta^-$  emitter with a released energy of  $Q = (18.591 \pm 0.001)$  keV and a half-life of  $(12.312 \pm 0.025)$  years [31].

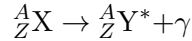
- **$\beta^+$ -decay:** A weak process during which a proton is converted into a neutron. A neutrino and a positron are emitted. Analog to  $\beta^-$ -decay the energy spectra of the decay products are continuous.



- **Electron capture (EC):** A competing process to  $\beta^+$ -decay is electron capture and it occurs in any  $\beta^+$ -emitter as another decay channel. A proton of the nucleus is transformed into a neutron, while a shell electron close to the nucleus is annihilated and a neutrino is produced and emitted. The gap in the atomic shell leads to the emission of a characteristic X-ray fluorescence photon or Auger electrons in the energy range of several eV to a few keV [34].



- **$\gamma$ -decay:** If a nucleus is left in an excited state after e.g. a spallation process, it can deexcite by emitting  $\gamma$ -radiation. In case the excited state is a long-lived (metastable) state, its deexcitation is called isomeric transition (IT) and has distinct lines.



Since the ComPol detectors are sensible to photons, and electrons, the relevant decays in this case are  $\beta$ -decay, and  $\gamma$ -decay.  $\alpha$  decay does not directly contribute as a notable background in the detectors, since the resulting  $\alpha$ -particle has a very short penetration depth and does rarely reach the detector system. Due to its highly ionizing capability,  $\alpha$ -particles can excite the surrounding material leading to the creation of secondary electrons and/or fluorescence photons, which in turn can interact in the detectors and cause a measurable background.

Depending on the isotope, it happens, that the daughter nucleus itself is again radioactive and subsequently decays with a specific decay type, forming a new radioactive daughter nucleus. This process can continue especially for actinoid nuclides and is commonly called a *decay chain*. Within every step in the chain, there is often more than one decay process possible. Instead, the nucleus can decay via different decay types to a diverse number of daughter nuclei. The probability for one specific decay type to happen is referred to as the *branching ratio*. The decay chain will end at very long-living or stable nuclei. Within such a sequence the production rate of one isotope is dependent on the decay rate of the isotope(s) beforehand. The mathematical description of decay chains can become very computing time consuming and complicated and will not be further explained here. For an in-depth description and some computing approaches, the reader is referred to [36] and [37].

### 3.3. Conclusion

To sum up, the total background for our instrument consists of the cosmic radiation background and the background due to the South Atlantic Anomaly. The former is assumed to be constant with regard to the mission time and the position of the CubeSat. The latter strongly varies with the position of the satellite and the inclination of the Orbit. Both background sources have a direct contribution to the overall background, as well as a time-dependent contribution due to cosmogenic activation. An overview of the different background sources and their contributions is given in Figure 3.5. The direct contribution of the SAA will not be investigated further, since the scientific data-taking is stopped during the flight through the SAA. Hence, the total background rate  $R_{BG}$  is calculated as shown in Equation 3.3.

$$R_{BG} = R_{CR}^{dir} + R_{CR}^{Act} + R_{SAA}^{Act} \quad (3.3)$$

### 3. Contributions to the telescope background

The direct cosmic radiation rate  $R_{CR}^{dir}$  includes all hits in the detectors after event selection is applied, except the hits originating from radioactive decays. The rate from activation is given additionally with  $R_{CR}^{Act}$ . The rate from activation due to the SAA is given with  $R_{SAA}^{Act}$ . An overview over all rates, which are discussed in the course of this thesis is given in [section A.1](#).

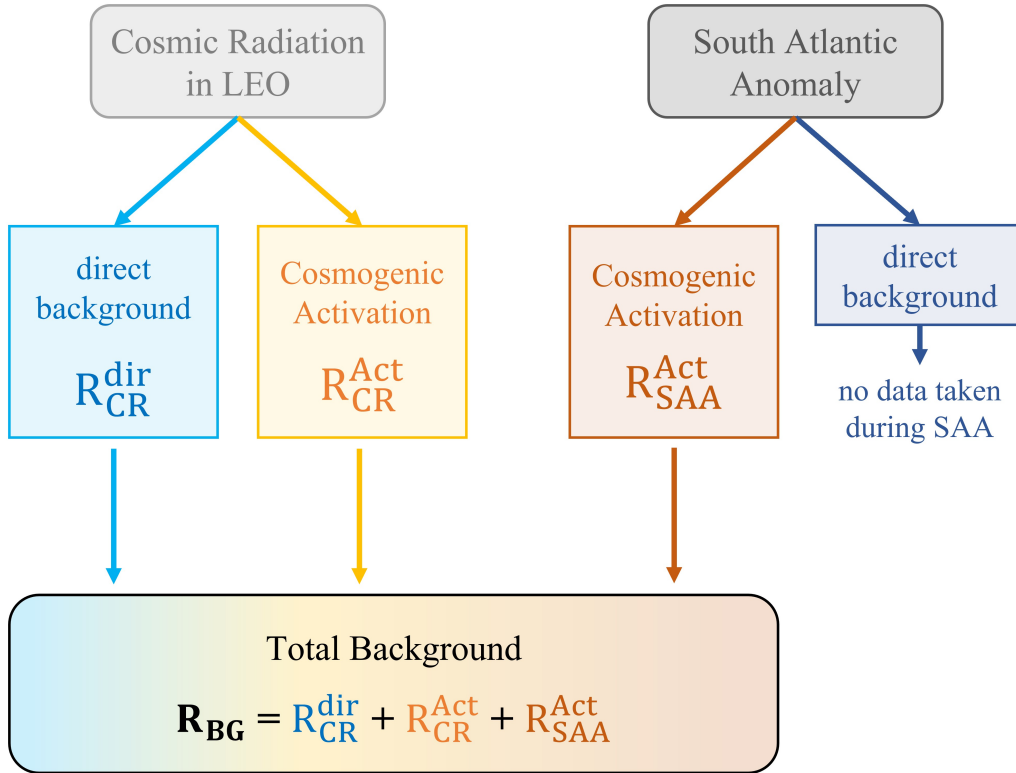


Figure 3.5.: **Overview over all relevant background sources and their different contributions to the overall background.** The cosmic radiation, as well as the South Atlantic Anomaly, create a direct background due to interactions of the particles in the detector system. They also create a time-dependent background due to cosmogenic activation. The direct background originating from the SAA is not considered further, since no data will be taken during this period.

The direct background can be reduced by adding more shielding material before and around the detector system. However, the additional shielding material is exposed to cosmic radiation and SAA protons, which will lead to an increase in the background due to cosmogenic activation. In order to minimize the overall background, the optimal solution for the shielding geometry, mass, and material has to be found. This is done in the following chapters of this thesis via simulation of different shielding configurations with Geant4 and investigating the impact of shielding on all relevant background contributions.

## 4. Simulation of the ComPol CubeSat with GEANT4

In preparation for the ComPol CubeSat mission, an in-depth study of the sensitivity of the detector system and the optimal shielding configuration must be carried out. In order to avoid the cost and time of building several prototypes, nowadays one mainly resorts to simulations. The ComPol CubeSat is simulated with the simulation toolkit Geant4 (**G**eometry and **t**ransport **4**). Hereby, its sensitivity and its behavior in orbit are estimated, considering the background sources mentioned in [chapter 3](#). In [section 4.1](#), a general introduction to the simulation tool is given. In [section 4.2](#) the specific implementations for the ComPol project are explained in more detail.

### 4.1. Introduction to Geant4

The results of this thesis were obtained using the simulation toolkit Geant4 using Monte Carlo methods. It simulates particle interactions in matter and is widely used in high energy physics, nuclear physics, and space science [38]. The tool is based on the object-oriented programming language C++ and was originally founded at CERN. Today, the maintenance and development are supervised by the international Geant4 Collaboration of physicists and software engineers [39]. The simulation toolkit includes features for geometry, particle tracking, detector response, analysis, and run management. It also comes with a user interface and visualization software for geometry and simulated particles. All features can be highly customized and are updated regularly. This makes Geant4 one of the most powerful particle simulation toolkits available [1].

The simulations can be built relatively quickly since the user does not have to spend much time on low-level implementations of physical processes. Furthermore, Geant4 accesses databases for all chemical elements and their properties, as well as interaction and scattering cross sections for a large number of particles and materials in a wide energy range. In order to run a simulation, the user has to implement the geometry of the setup, including the overall design of all materials of the experiment, the specific detector design, and the particle source. The materials are constructed via volumes of the respective shape, which are then assigned with physical material in the next step. It is also possible to create customized materials by mixing elements according to the desired chemical composition. In addition, electric and magnetic fields can be integrated into the setup. The detector materials can be assigned as sensitive volumes, which can be modified independently, using a separate class to save hits and conduct an analysis to generate a realistic detector response. The simulated particles can also be chosen freely. Geant4 is able to simulate all standard model particles and the user is also allowed to define their own particles. Particles and interactions, which are not relevant to the user's needs can be disabled in order to speed up the simulation time and minimize the output size. The offered physical processes cover all electromagnetic, hadronic, and optical processes in an energy range from 250 eV to several TeV, as well as radioactive decays [39]. The particles and physical processes have to be included by the user in the simulation and they are set by the physics lists. This is an already predefined class in Geant4 to select and

## 4. Simulation of the ComPol CubeSat with GEANT4

coordinate the processes and particles by the user.

The working principle of Geant4 follows the Monte Carlo method. Each event starts with an initial particle starting at the position of the particle source with a specific energy defined by the user. All interactions and secondary particles are generated with regard to their probability based on the interaction cross-section. The event ends when all secondary particles are either absorbed or have left the defined world volume, i.e. region of interest. The overall number of simulated events is chosen by the user. For each event the user can save information about the interactions of interest, for instance, the position, interaction type, time, deposited energy, etc. All particles are tracked and thus the history of interactions of one specific event and all its secondary particles can be reconstructed.

### 4.2. General simulation settings

In order to conduct simulations for the ComPol project, the CubeSat geometry, the necessary Physics Lists, and particle sources need to be implemented in Geant4. In the following, an overview of these customized segments of the simulation is given.

#### Geometry

The geometry is not the same for all simulations referred to in this work, however, the standard geometry is shown in [Figure 4.1](#). The SDD detector is shown in blue, while the calorimeter is illustrated in red. In front of the detector system, the shielding plate and the collimator are positioned (light gray). If it is not stated otherwise, the shielding plate and collimator are made of lead. The holding structure of the CubeSat is colored in dark gray and is made of aluminum.

Behind the detector system, several layers of material are shown in different colors. The materials and their layer thicknesses are listed in the caption. They represent the components in the CubeSat, and their masses are estimated on the basis of the material distribution in the final satellite. The silicon is used in the SiPMs, the aluminum is mostly integrated into the electronics, and mechanical parts, while the lithium is implemented in order to represent the batteries. The PCB-substrate and the electrical components (copper wires) are also taken care of. In order to control the position and momentum of the satellite, the reaction wheels made of iron are also included in the dummy material. For the background simulation and the activation study, it is important to consider these (dummy-) materials. They can act as shielding, but can also cause background due to activation (for the analysis see [chapter 5](#) and [chapter 6](#)). In favor of reducing the simulation complexity, the materials are implemented as simple layers in the geometry.

The sides of the CubeSat are covered with solar panels (yellow), which are set transparent in this sketch in order to visualize the interior of the geometry. The overall structure of the geometry stays constant for all simulations, whereas only the shielding shape and material are changed. The implemented geometry is chosen in a way to resemble a simplified version of a smaller 1-Unit CubeSat ( $10 \times 10 \times 11.3 \text{ cm}^3$ ). Using a simplified version of the overall geometry saves time during the implementation process in Geant4, and significantly reduces the simulation time, hence fewer interactions at material borders need to be simulated. The smaller size of the CubeSat is compensated by stacking the various payload materials (PCB, wires and cables, battery, etc...) as solid blocks behind the detector system. In the final CubeSat, the overall stacking density will be lower, however, the overall mass and hence the shielding efficiency will stay the same.

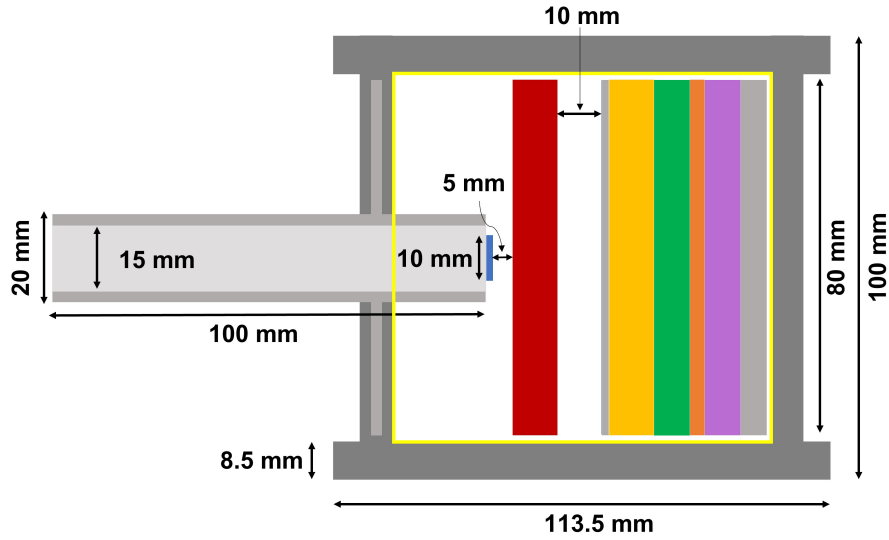


Figure 4.1.: **Simplified model of the ComPol CubeSat as implemented in Geant4.**

In different simulations, only the shielding material and its geometry are changed. The SDD detector is shown in blue, the calorimeter is depicted in red. The shielding plate and collimator are drawn in light grey. The CubeSat structure is shown in dark grey. Several layers of dummy material are placed behind the detector system. The dummy material represents an estimate of the overall materials and their masses in the final CubeSat. The layers are placed as follows: 0.2 mm silicon (not drawn here), 1 mm aluminum (light grey), 1 cm lithium (light orange), 8 mm PCB material (FR-4) (green), 3 mm copper (orange), 8 mm iron (violet) and 6 mm aluminum again. The sides of the CubeSat are covered with solar panels which are indicated by the yellow line (the surface is set transparent).

### Particle source

For the simulations in this thesis, three different particle sources are used to simulate the Cygnus X-1 signal and the background radiation.

- *Cygnus X-1*

The signal simulation is done with a quadratic particle source with an area of  $1 \text{ cm}^2$ , which is situated in front of the collimator. The beam with square cross section illuminates exactly the whole SDD. Its energy distribution follows the spectrum of Cygnus X-1 in the LHS. The spectrum of both states of the BHB is shown in [Figure 4.2](#). The beam consists of 100% polarized light and the simulated energy is in the range of 0 keV to 300 keV. In Geant4 only the LHS spectrum is implemented. The number of simulated particles is chosen to correspond to a real simulation time of approximately 8 months.

- *Cosmic Radiation in LEO*

The Cosmic Radiation background originates from a spherical surface around the CubeSat. The initial direction of all emitted initial particles follows the cosine emission law of Geant4 in order to generate isotropic radiation inside the sphere. The energy spectra are implemented as shown in [Figure 3.1](#) and the full energy range is taken into consideration. The simulated particles are photons, electrons, positrons, protons, neutrons, and alpha particles. The simulations are performed with  $10^{11}$  initial particles, which

#### 4. Simulation of the ComPol CubeSat with GEANT4

corresponds to a real simulation time of one month in orbit.

- *SAA spectrum*

Similar to the Cosmic Radiation background the particle source for all SAA simulations is chosen to be a spherical surface around the CubeSat emitting with the cosine emission law. The energy spectra of the SAA-protons and -electrons are implemented as shown in [Figure 3.3](#) and the full energy range is taken into consideration. Protons and electrons are simulated separately here, in order to minimize the output data per simulation. The number of simulated initial particles is set at  $10^{11}$ . Regarding the SAA-protons, this corresponds to a total time of 2370 s in the SAA, for the SAA-electron simulations the corresponding time in the region of increased flux is 104 s.

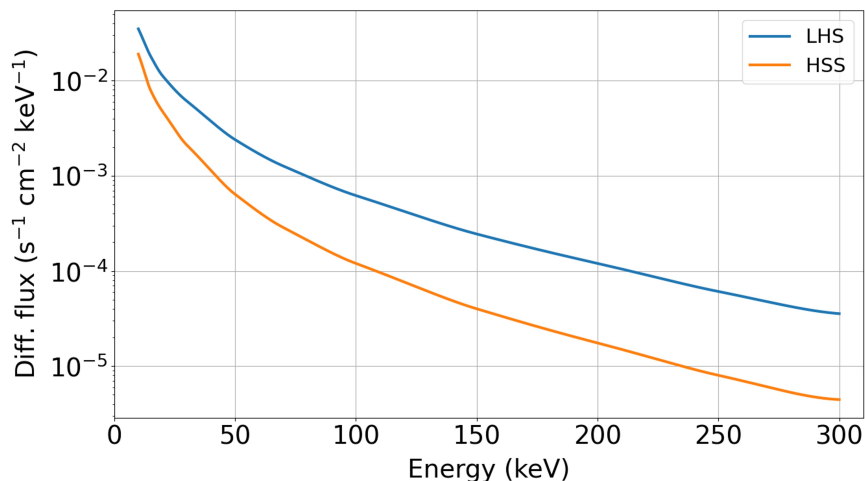


Figure 4.2.: **Cygnus X-1 spectra of the LHS and HSS in the region of interest.**

The varying real simulation times from signal and background simulations, and thus the differing absolute output data, are normalized during the analysis.

#### Physics lists

The used physics list for the ComPol simulations is generated using several predefined constructors provided by Geant4. For the electromagnetic interactions the `G4EmLivermorePolarizedPhysics` is used. The hadronic interactions are included with `G4HadronPhysicsQGSP_BERT_HP`. The radioactive decay is taken care of via the `G4DecayPhysics` and `G4RadioactiveDecayPhysics` constructors. All used physics lists are valid in the energy region of interest.

#### Detector response

The implementation of the detector response is described in [\[1\]](#) and will not be explained further here. The energy and position resolution of both detectors are discussed in [subsection 2.1.1](#) and [subsection 2.1.2](#).

## 5. The activation study

As described in [subsection 3.2.2](#), the exposure of the CubeSat to cosmic radiation leads to activation of the satellite material and thus to an additional background rate in our detectors due to radioactive decays. In order to estimate the exact influence of cosmogenic activation on the total background rate, a detailed analysis was carried out. The standard ComPol geometry (a sketch of it is shown in [Figure 4.1](#)) was simulated with Geant4. The exact details of the implementation of the activation simulation in Geant4 are explained in [section 5.1](#). In [section 5.2](#), the activation by the cosmic radiation is analyzed. The influence of the SAA on the activation is presented in [section 5.3](#). The results are summarised in [section 5.4](#).

### 5.1. Implementation in GEANT4

For the purpose of accessing the amount of activation in the CubeSat material, the Geant4 simulation needs to be capable of handling radioactivity and saving the requested output data. The radioactivity is taken into account during the simulation by adding the respective physics lists shown in [section 4.2](#). All created activated isotopes and excited nuclei are then marked and written to an output file. This was done with a user-specific code, which was added in the `TrackingAction.cc` and `StackingAction.cc` files of the simulation. The general ansatz of the code is outlined as follows:

1. Assigning a new global variable to all simulated particles (`SubEventID`).
2. Raising the value of the `SubEventID` every time a radioactive isotope or an excited nucleus is created (`SubEventID + 1`). The starting value at the start of each event is 1. For example, a cosmic neutron interacts with a lead isotope and generates a radioactive isotope via spallation. Thus, the radioactive isotope is assigned the `SubEventID = 2`.
3. Saving the radioactive isotope and its properties in an output file.
4. All particles, which originate from the radioactive decay of this isotope inherit the same value of the `SubEventID` as the isotope.  
For example, a  $\beta^+$ -decay happens and the emitted positron annihilates. The positron and the resulting photons are also marked with the `SubEventID = 2`. In the case of decay chains, the `SubEventID` for the subsequent radioactive daughter isotope is raised by 1 ( $\rightarrow$  `SubEventID = 3`).
5. The `SubEventID` is also saved for all hits in the detectors. Hits in the detectors are saved separately.  
For example, a photon interacts in the SDD and is thus saved as a hit in the detector with a `SubEventID = 2`. It can now be reconstructed, that this photon was generated as a result of a radioactive decay and therefore counts to the background due to activation.

Saving all radioactive isotopes and excited nuclei in all materials of the CubeSat gives an overview of the most abundant isotopes created. The order of the `SubEventIDs` gives the possibility to investigate decay chains. The full code can be found in the `TrackingAction.cc` and `StackingAction.cc` files in [section A.2](#).

## 5.2. Activation simulation for the cosmic radiation

The cosmic radiation contributes constantly to the activation of the CubeSat material. The term *activation*, is used in this thesis to describe all unstable isotopes that are created via a background particle. This includes radioactive isotopes, as well as excited states of nuclei. The resulting overall activation of the CubeSat components and the generated unstable isotopes are investigated in [subsection 5.2.1](#). In [subsection 5.2.2](#), the influence of the resulting radioactive decays on the rates in the detectors before and after the event selection is analyzed.

### 5.2.1. Activation of the CubeSat components

The activation rate in all parts of the satellite is illustrated in [Figure 5.1](#). The histogram shows the number of radioactive nuclei for all components used in the CubeSat. The absolute number of generated radioactive isotopes is normalized by the simulation time, leading to an activation rate. Since the shielding plate and the collimator consist of the same material (lead), they are summarized as "Shielding". The total activation rate for the whole CubeSat is given as follows:

$$\text{Activation Rate}_{\text{tot}} = 3.28 \text{ cps} \quad (5.1)$$

The cosmogenic activation is dominated by the shielding, the reaction-wheels, and the calorimeter.

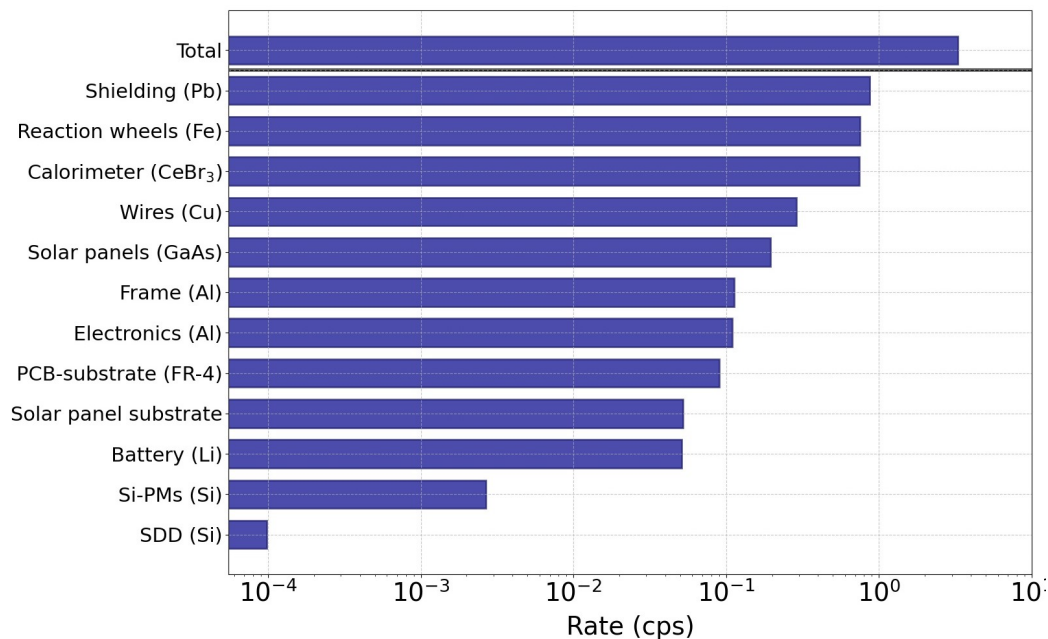


Figure 5.1.: **Rate of radioactive nuclei per component.** The amount of radioactive nuclei is given for each part of the CubeSat as an activation rate. The main materials are also shown in brackets next to the components. The masses of the components are based on estimations of the material distribution in the final CubeSat (c.f. [section 4.2](#)).

[Figure 5.2](#) shows the activation rate for all materials built in the CubeSat separately for all initial background particle types. Each activation rate is normalized to 100g of the respective material for a better comparison. The activation is dominantly produced by protons and

neutrons. This is true for all used materials and consistent with the description of activation processes in [subsection 3.2.2](#) theory. Taking [Figure 5.2](#) it is evident, that lead is the strongest activated material, followed by the calorimeter and the reaction wheels. These three components are investigated further and the isotopes generated due to activation are analyzed in more detail.

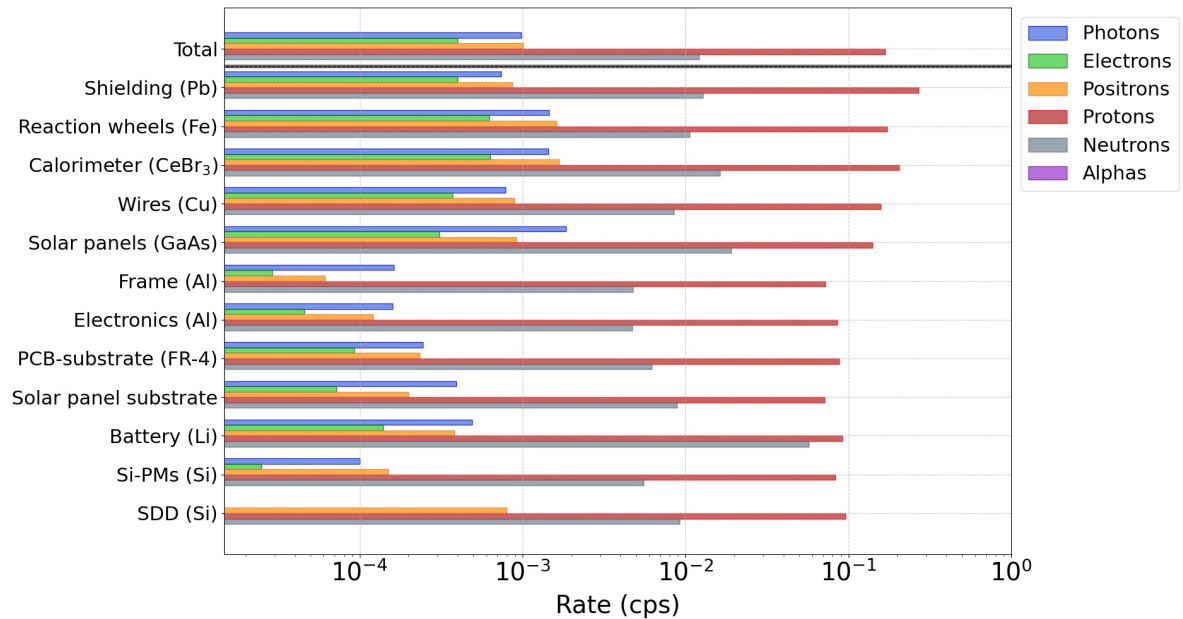
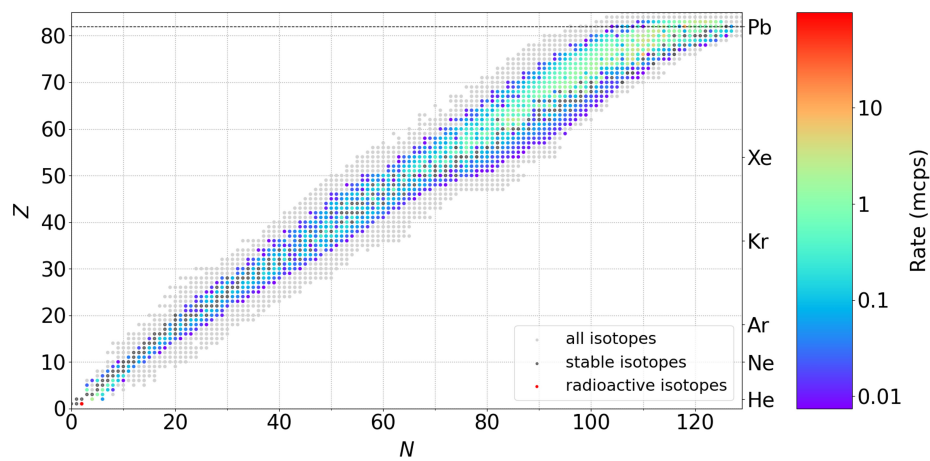


Figure 5.2.: **Rate of radioactive nuclei per material.** The activation rate is given separately for each initial background particle type. Each rate is normalized to 100g of the respective material in order to reach a better comparability.

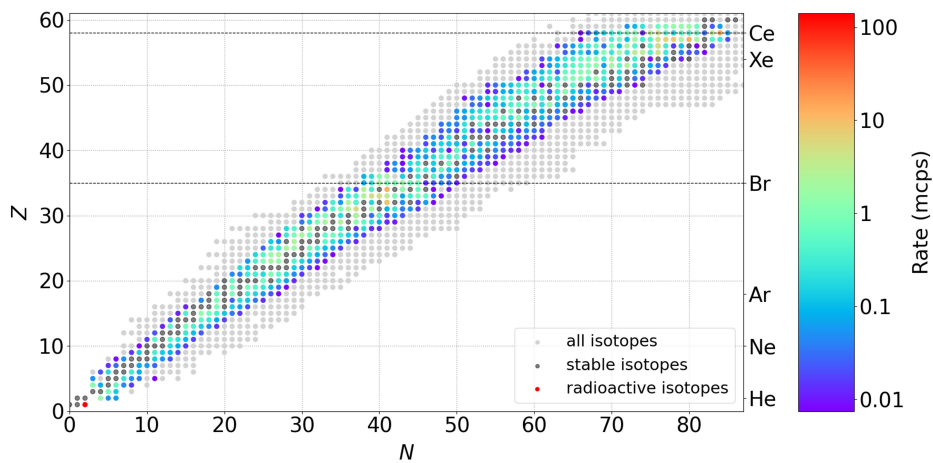
All created isotopes in the shielding, the reaction wheels, and the calorimeter respectively are shown in [Figure 5.3](#) in a nuclide chart. A large variety of isotopes are created in both cases, whereas tritium is the most prominent isotope since it is often generated as a byproduct of spallation processes (see [subsection 3.2.2](#)). The isotopes with  $Z$  and  $N$  next to lead, cerium, and bromine, and iron respectively, are also very commonly produced.

[Figure 5.4](#) shows the isotope charts for the lead shielding, however, the isotopes, created due to protons and neutrons are depicted separately. [Figure 5.4a](#) show the isotopes, which were created due to protons in the shielding. It becomes evident, that tritium is predominantly produced via protons since it is often generated as a byproduct of spallation processes together with high energetic protons. This is explained in [subsection 3.2.2](#). Additionally, a variety of lighter isotopes are generated, starting from lead. The frequency of isotopes is increasing towards the line of stable isotopes. The new isotopes are created due to spallation and fission processes, whereas especially spallation leads to a huge variety of different isotopes. After an initial spallation process, the resulting cascade of secondary neutrons can themselves again interact with some nuclei. These processes are also included in [Figure 5.4a](#). Furthermore, bismuth-isotopes ( $Z = 83$ ) are created via proton capture. These isotopes can only be created via direct interaction with the cosmic protons.

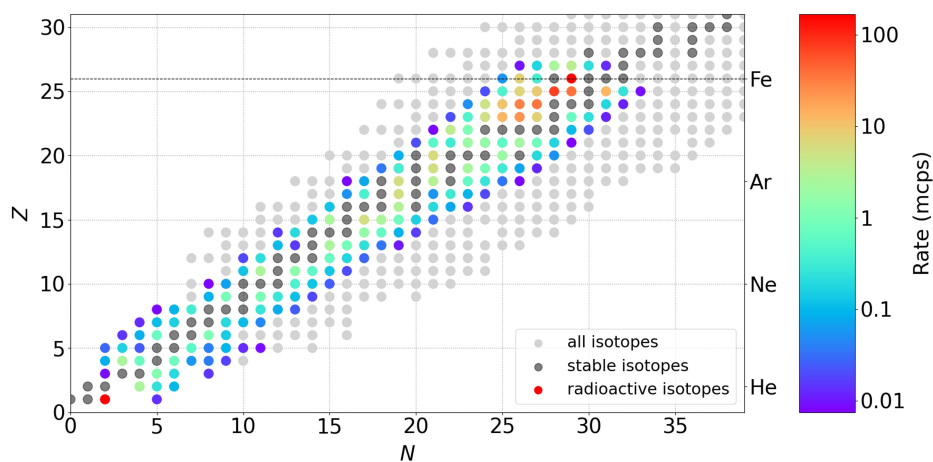
5. The activation study



(a) Radioactive isotopes in the lead shielding.

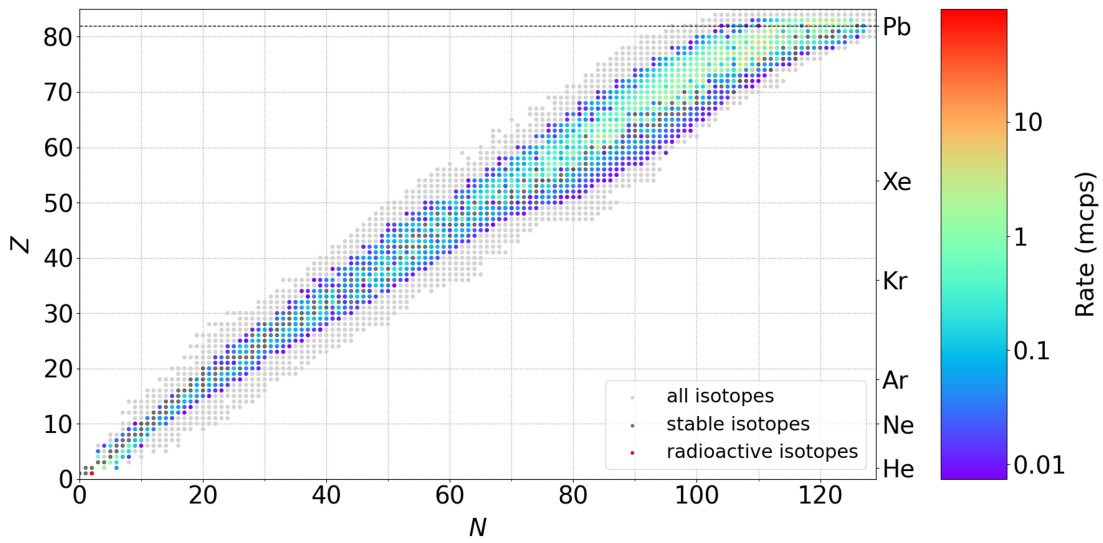


(b) Radioactive isotopes in the calorimeter.

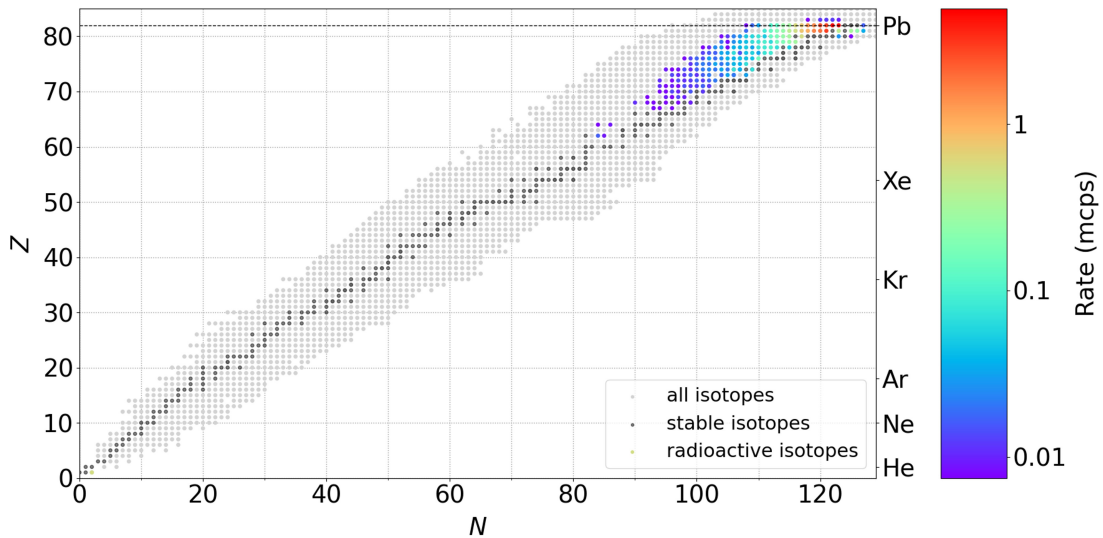


(c) Radioactive isotopes in the reaction wheels (iron).

Figure 5.3.: **Isotope charts showing the created radioactive isotopes.** a) gives the isotopes in the lead shielding. b) refers to the isotopes in the calorimeter, and c) displays the isotopes in the reaction wheels (iron). The colors indicate the abundance of each isotope (given in their creation rate). The stable isotopes are marked in dark grey, and for better orientation, all known isotopes are drawn in the background with a light grey color.



(a) Radioactive isotopes in the lead shielding created by protons.



(b) Radioactive isotopes in the lead shielding created by neutrons.

Figure 5.4.: **Radioactive isotopes in the lead shielding created by protons and neutrons.** a) gives the isotopes created by protons. b) refers to the isotopes formed via interactions with neutrons. The colors indicate the abundance of each isotope (given in their creation rate). The stable isotopes are marked in dark grey, and for better orientation, all known isotopes are drawn in the background with a light grey color.

Figure 5.4b gives an overview of the isotopes created due to neutrons interacting in the lead shielding. The isotopes with  $Z$  and  $N$  next to lead are very commonly produced, and only a low amount of tritium is produced here. Inelastic scattering processes of cosmic neutrons with nuclei kick out a few nucleons from the target nucleus via spallation and thus create lighter isotopes in the near vicinity of the target nucleus. A comparison of the overall rates indicates, that protons generate the main contribution to activation. This was already shown in Figure 5.2. The isotope charts showing the nuclides created by protons and neutrons in

## 5. The activation study

the the iron reaction wheels and the CeBr<sub>3</sub> calorimeter are given in [section A.3](#).

The next figures show a zoom into the regions around the initial elements of the considered materials. The zoom into the isotopes created in the vicinity of lead is depicted in [Figure 5.5](#). For the calorimeter the isotopes around bromine (see [Figure 5.6a](#)) and cerium (see [Figure 5.6b](#)) are given individually. In [Figure 5.7](#) the region around iron is illustrated. Additionally, the most abundant isotopes are labeled. If these isotopes form as a decay product of another isotope the decay path is indicated with dotted black arrows. If the marked isotope then decays further, the decay path is shown with a solid black arrow. Additionally, the labeled isotopes are listed in [Table 5.1](#) to [Table 5.4](#). Their most common decay process, the lifetime, and (if applicable)  $\gamma$ -energies in the energy range of interest are also given. The data on the decay type, the lifetime  $T_{1/2}$ , and the  $\gamma$ -energies are taken from [\[40\]](#). Each zoomed region is discussed individually in the following paragraphs, and their possible influences on the background rate in the detectors are evaluated.

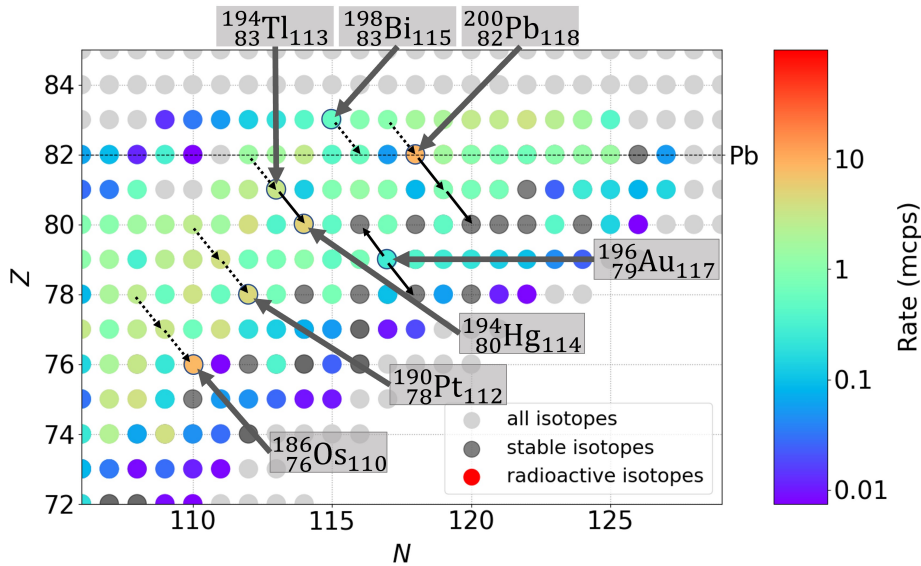


Figure 5.5.: **Isotope chart showing a zoom into the region around lead.** The most abundant isotopes are labeled and their decay paths are indicated with arrows.

### Zoom into the region around lead

In [Figure 5.5](#) it is evident, that the most prominent isotope is  $^{200}_{82}\text{Pb}_{118}$  which is can be created via inelastic proton scattering. The isotopes  $^{194}_{80}\text{Hg}_{114}$ ,  $^{190}_{78}\text{Pt}_{112}$ , and  $^{186}_{76}\text{Os}_{110}$  are predominantly created due to the EC  $\beta^+$ -decays of heavier isotopes. The lifetimes of these isotopes are given in [Table 5.1](#) and exceed the mission time by far. Thus, their decay cannot contribute to the background in the detectors. The half-lives of the other isotopes given in the table lie within a few days maximum and their  $\beta^+$ -decay products may contribute to the background rate. The resulting positrons may not contribute directly, however, the annihilation photons will possibly reach the detectors directly, or after further interactions in the surrounding material. The direct 511 keV annihilation photons are not critical in terms of background,

Table 5.1.: **Isotopes in the lead region.** The isotopes are labeled in Figure 5.5 listed with their predominant decay type, lifetime  $T_{1/2}$ , and for  $\gamma$ -decays the respective  $\gamma$ -energy. The data is taken from [40].

Isotope	decay type	$T_{1/2}$	$\gamma$ Energy
$^{198}_{83}\text{Bi}^*$	IT	7.7 s	248.5 keV
$^{198}_{83}\text{Bi}_{115}$	EC $\beta^+$	10.3 min	-
$^{200}_{82}\text{Pb}_{118}$	EC	21.5 h	-
$^{194}_{83}\text{Tl}^*$	IT	33 min	260 keV
$^{194}_{83}\text{Tl}_{113}$	EC $\beta^+$	33 min	-
$^{194}_{80}\text{Hg}_{114}$	EC	447 y	-
$^{196}_{79}\text{Au}^*$	IT	8.1 s	84.7 keV
$^{196}_{79}\text{Au}_{117}$	EC $\beta^+$	6.2 d	-
$^{190}_{78}\text{Pt}_{112}$	$\alpha$	$4.9 \times 10^{11}$ y	-
$^{186}_{76}\text{Os}_{110}$	$\alpha$	$2.5 \times 10^{15}$ y	-

since they lie outside the energy range of interest (11 keV-300 keV) (see subsection 2.2.1). A special focus has to be put on  $\gamma$ -decays (IT) of abundant excited isotopes, which emit photons with energy within the thresholds. The decay photons of the isotopes  $^{198}_{83}\text{Bi}^*$ ,  $^{194}_{83}\text{Tl}^*$ , and  $^{196}_{79}\text{Au}^*$  can contribute to the background rate due to activation.  $^{198}_{83}\text{Bi}^*$  as well as the other – not marked – bismuth isotopes are solely created directly by capturing a cosmic proton.

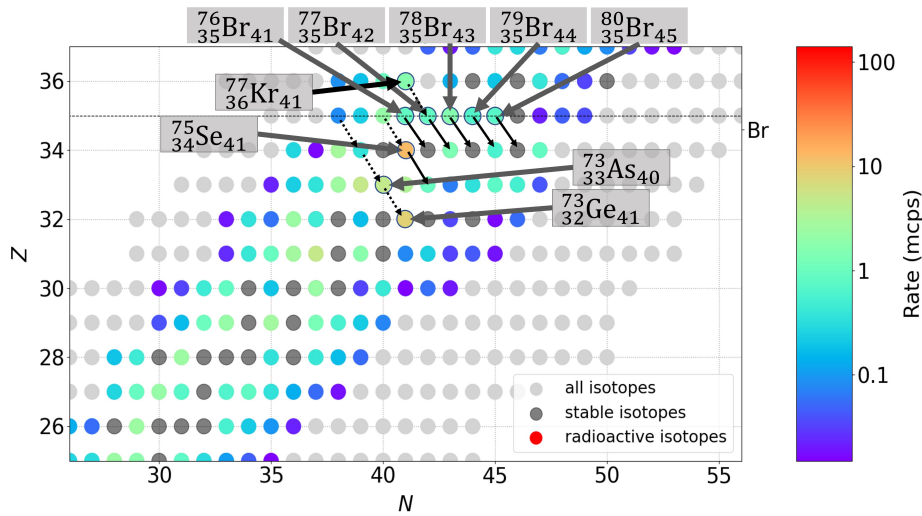
### Zoom into the region around bromine

As seen in Figure 5.6a, the most often produced isotopes are  $^{75}_{34}\text{Se}_{41}$ , and  $^{73}_{32}\text{Ge}^*_{41}$ , whereas the latter is primarily created as a daughter of previous decays. It deexcites within 0.5 s via emission of a 66.7 keV photon (given in Table 5.2), which could contribute to the background rate. With regard to the half-lives of the labeled isotopes, they all decay within the estimated mission time of 1 year. As explained in the previous paragraph, the EC  $\beta^+$ -decays could again have an indirect influence on the telescope's background via annihilation photons. The various bromine isotopes all possess an excited state which decays via  $\gamma$ -emission in the energy range of interest. As a result, they have to be considered as possible sources of background due to activation.

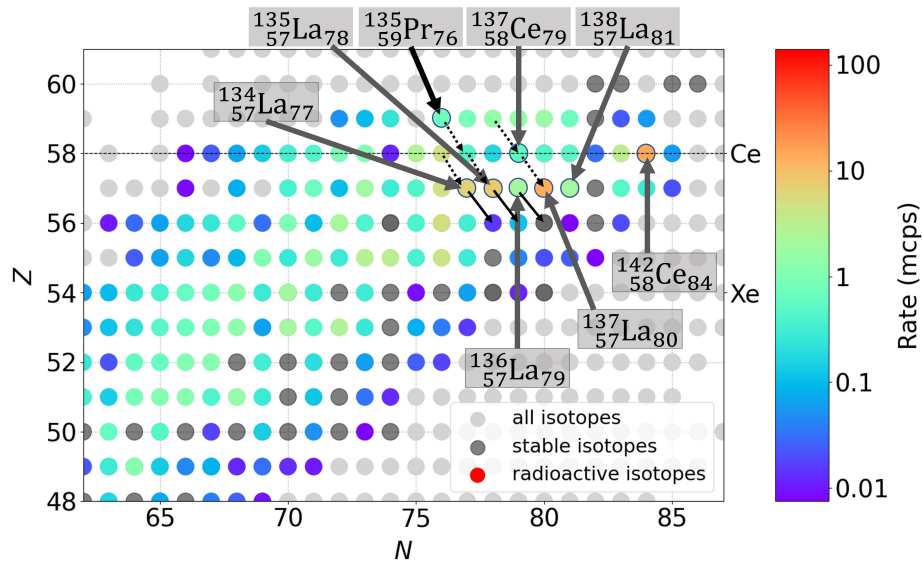
### Zoom into the region around cerium

Figure 5.6b illustrates, that the most likely created isotope is  $^{142}_{58}\text{Ce}_{84}$ , followed by  $^{137}_{57}\text{La}_{80}$ , and  $^{135}_{57}\text{La}_{78}$ . The first one can be created via inelastic proton scattering, whereas the latter are created in chains. Only the lifetime of  $^{135}_{57}\text{La}_{78}$  is short enough to consider the  $\beta^+$ -decay

5. The activation study



(a) Isotope chart showing a zoom into the region around bromine.



(b) Isotope chart showing a zoom into the region around cerium.

Figure 5.6.: **Isotope chart showing a zoom into the region around bromine and cerium** a) displays the region around bromine, and b) gives the zoom around cerium. The most abundant isotopes are labelled and their decay paths are indicated with arrows

positron as possible background source (see Table 5.3). Their half-life is rather short – maximum a few hours, except  $^{138}_{57}\text{La}_{81}$  which decays after  $1.0 \times 10^{11}$  y. Considering the half-life of the other marked isotopes  $^{138}_{57}\text{La}_{81}$ ,  $^{137}_{57}\text{La}_{80}$ , and  $^{142}_{58}\text{Ce}_{84}$  can be neglected as possible background sources. The shown  $\gamma$ -decays (IT) of all mentioned lanthanum, and the cerium isotope are all relevant as possible background due to activation.

Table 5.2.: **Isotopes in the bromine region.** The isotopes are labeled in Figure 5.6a listed with their predominant decay type, lifetime  $T_{1/2}$ , and for  $\gamma$ -decays the respective  $\gamma$ -energy. The data is taken from [40].

Isotope	decay type	$T_{1/2}$	$\gamma$ Energy
$^{77}_{36}\text{Kr}^*_{41}$	IT	118 ns	66.5 keV
$^{77}_{36}\text{Kr}_{41}$	EC $\beta^+$	71.2 min	-
$^{76}_{35}\text{Br}^*_{41}$	IT	1.3 s	102.6 keV
$^{76}_{35}\text{Br}_{41}$	EC $\beta^+$	16.2 h	-
$^{77}_{35}\text{Br}^*_{42}$	IT	4.3 min	105.9 keV
$^{77}_{35}\text{Br}_{42}$	EC $\beta^+$	57.0 h	-
$^{78}_{35}\text{Br}^*_{43}$	IT	119.4 $\mu\text{s}$	180.9 keV
$^{78}_{35}\text{Br}_{43}$	EC $\beta^+$	6.4 min	-
$^{79}_{35}\text{Br}^*_{44}$	IT	4.8 s	207.6 keV
$^{80}_{35}\text{Br}^*_{45}$	IT	4.4 h	85.5 keV
$^{80}_{35}\text{Br}_{45}$	EC $\beta^+$	17.7 min	-
$^{75}_{34}\text{Se}_{41}$	EC $\beta^+$	119.8 d	-
$^{73}_{33}\text{As}_{40}$	EC $\beta^+$	80.3 d	-
$^{73}_{32}\text{Ge}^*_{41}$	IT	0.5 s	66.7 keV

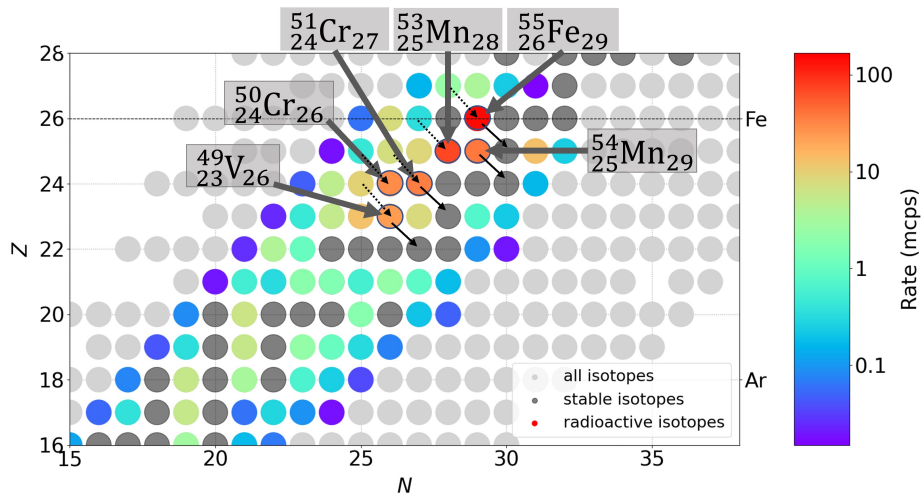


Figure 5.7.: **Isotope chart showing a zoom into the region around iron.** The most abundant isotopes are labelled and their decay paths are indicated with arrows

## 5. The activation study

Table 5.3.: **Isotopes in the cerium region.** The isotopes are labeled in Figure 5.6b listed with their predominant decay type, lifetime  $T_{1/2}$ , and for  $\gamma$ -decays the respective  $\gamma$ -energy. The data is taken from [40].

Isotope	decay type	$T_{1/2}$	$\gamma$ Energy
$^{135}_{59}\text{Pr}_{76}$	EC $\beta^+$	24 min	-
$^{137}_{58}\text{Ce}_{79}^*$	IT	34.4 h	254.3 keV
$^{137}_{58}\text{Ce}_{79}$	EC $\beta^+$	9.0 h	-
$^{142}_{58}\text{Ce}_{84}$	?	$5.0 \times 10^{16}$ y	-
$^{134}_{57}\text{La}_{77}$	EC $\beta^+$	6.5 min	-
$^{135}_{57}\text{La}_{78}$	EC $\beta^+$	19.5 h	-
$^{136}_{57}\text{La}_{79}^*$	IT	114 ms	259.5 keV
$^{136}_{57}\text{La}_{79}$	EC $\beta^+$	9.9 min	-
$^{137}_{57}\text{La}_{80}$	EC	$6.0 \times 10^4$ y	-
$^{138}_{57}\text{La}_{81}^*$	IT	116 ns	72.6 keV
$^{138}_{57}\text{La}_{81}$	EC $\beta^+$ , $\beta^-$	$1.0 \times 10^{11}$ y	-

Table 5.4.: **Isotopes in the iron region.** The isotopes are labeled in Figure 5.7 listed with their predominant decay type, lifetime  $T_{1/2}$ , and for  $\gamma$ -decays the respective  $\gamma$ -energy. The data is taken from [40].

Isotope	decay type	$T_{1/2}$	$\gamma$ Energy
$^{55}_{26}\text{Fe}_{29}$	EC	2.7 y	-
$^{53}_{25}\text{Mn}_{28}$	EC	$3.7 \times 10^6$ y	-
$^{54}_{25}\text{Mn}_{29}$	EC	312 d	-
$^{50}_{24}\text{Cr}_{26}$	EC	$1.3 \times 10^{18}$ y	-
$^{51}_{24}\text{Cr}_{27}$	EC	27.7 d	-
$^{49}_{23}\text{V}_{26}$	EC	330 d	-

### Zoom into the region around iron

Taking Figure 5.7, the most abundant isotopes are  $^{55}_{26}\text{Fe}_{29}$ , and  $^{53}_{25}\text{Mn}_{28}$ , closely followed by the other marked isotopes. The iron and manganese isotopes are mainly produced through direct interaction with cosmic protons and neutrons. As shown in Table 5.4 all marked isotopes only decay via EC emitting a neutrino. Hence, they do not contribute to the background.

Among all the isotopes considered here, most contribute indirectly to the background due to activation by emitting a positron from  $\beta^+$ -decay. In addition, photons in the energy range of interest are emitted by the deexcitation of excited nuclei (IT). The isotopes shown in the figures and the decay data provided in the tables represent only a small fraction of all isotopes and decay possibilities and do not claim to be complete. However, it would go beyond the scope of this work to consider all decay channels of all isotopes. This overview is merely intended to give some examples of possible sources for the background from activation.

### 5.2.2. Activation rate after event selection

In order to determine the overall influence of activation on the background rates in the detectors, the event selection (c.f. [subsection 2.2.1](#)) is applied. The remaining background rates (total and due to activation) are listed in [Table 5.5](#).

Table 5.5.: **Total rates  $R^{\text{tot}}$  and rates due to activation  $R^{\text{Act}}$  in different stages of the event selection.**  $R_{\text{SDD}+\text{Cal}}$  refers to the sum of rates in both detectors, before the event selection is applied. The rate of coincident events is given with  $R_{\text{coinc}}$ , and  $R_{\text{CR}}$  describes the rate after full event selection. Additionally, the contribution of activation to the total rate at each stage is given in %.

	$R^{\text{tot}}$	$R^{\text{Act}}$	$\frac{R^{\text{tot}}}{R^{\text{Act}}}$
$R_{\text{SDD}} + R_{\text{Cal}}$	119.09 cps	0.97 cps	0.81 %
$R_{\text{coinc}}$	14.92 mcps	0.01 mcps	0.08 %
$R_{\text{CR}}$	0.88 mcps	2.61 $\mu$ cps	0.31 %

The background rate originating from activation before the event selection is applied is found to be 0.81% of the overall background rate in the detectors. After the event selection is applied,  $R_{\text{CR}}^{\text{Act}}$  is the final background rate from cosmogenic activation due to the cosmic radiation.

$$R_{\text{CR}}^{\text{Act}} = 2.61 \mu\text{cps} \quad (5.2)$$

This corresponds to 0.31% of the overall background rate after event selection. Therefore, the activation of the CubeSat material due to its exposure to cosmic radiation is found to have no relevant influence on the overall background rate.

## 5.3. Activation simulation including the SAA

In the next step, the influence of the second dominant background source on the detectors and the cosmogenic activation is investigated. This contribution from the SAA is orbit dependent and therefore changes over time. [section A.4](#) aims to find the background rate originating from activation due to the SAA ( $R_{\text{SAA}}^{\text{Act}}$ ). In [subsection 5.3.2](#) the remaining events from activation after event selection are investigated further.

### 5.3.1. SAA background rates

Since this background is time-dependent, the activation does not happen constantly. The CubeSat passes through the SAA during approximately six consecutive orbits for approximately 10 minutes per orbit. During this time, the activation rate is increased. In between,

## 5. The activation study

there is no activation due to the SAA and only the activation due to the cosmic radiation takes place. Furthermore, the decay of the generated radioactive isotopes from the SAA-induced activation causes an additional background rate. The overall temporal evolution of the count rate from the SAA in both detectors for one day in orbit is shown in [Figure 5.8](#). The calculation of how the temporal evolution is derived from the individually simulated events is described in [section A.4](#). The direct background rate from cosmic radiation in the SDD and

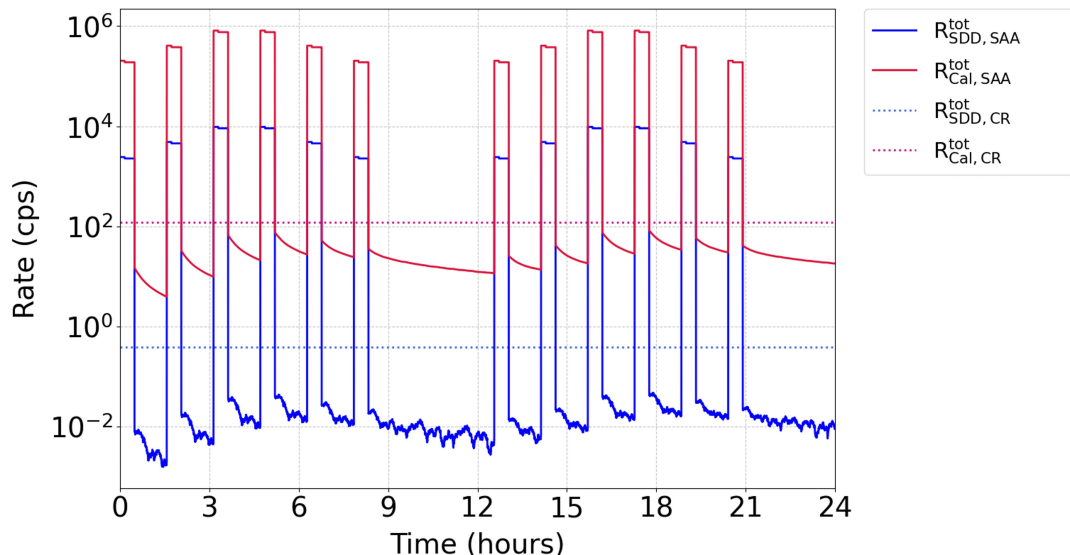


Figure 5.8.: **Temporal evolution of the background rate from the SAA for one day.**

The rate in the SDD is given in blue, and the rate in the calorimeter is plotted in red. The background rate from cosmic radiation in the SDD and calorimeter are shown with dotted lines. During the SAA, the rate in both detectors is increased by approximately 5 orders of magnitude. Between the SAA passages, the decay of activated nuclei generates an additional background.

A detailed explanation of how this temporal evolution is obtained from the simulation data can be found in [section A.4](#).

calorimeter are displayed with a dotted line to provide a better orientation. The respective background counts are determined using the cosmic radiation spectrum.

$$R_{\text{SDD, CR}}^{\text{tot}} = 0.39 \text{ cps} \quad (5.3)$$

$$R_{\text{Cal, CR}}^{\text{tot}} = 118.70 \text{ cps} \quad (5.4)$$

During the SAA passages, the overall rate is increased by approximately 5 orders of magnitude. The increased rate consists mainly of direct interactions of the SAA-electrons and -protons and secondaries which are generated in the CubeSat material. The extreme background rate in the detectors, of about 10 kcps in the SDD and almost 1 Mcps in the calorimeter, suggests that the data acquisition should be switched off during the SAA period.<sup>1</sup> This was already proposed in [subsection 3.2.1](#). The detectors themselves do not need to be switched off, since the SDD and the calorimeter could handle such a high a count rate. Between the flights

<sup>1</sup>In comparison with the signal rate of Cygnus X-1, a maximum SNR of 0.002 is calculated. For this purpose, the SAA background rate after event selection was used.

through the SAA, the radioactive isotopes created during the SAA passage, decay. This leads to an additional background rate, which has to be added to the cosmic radiation background rate.

Figure 5.9 displays the background rate only from the activation due to the SAA for one day in orbit. This background rate is created exclusively by the SAA-protons since the cosmogenic activation is predominantly generated by hadrons as illustrated in subsection 3.2.2. No contribution from the SAA-electrons is obtained. In order for electrons to contribute to the activation, they need to have higher energies than the SAA-electrons. All short-living

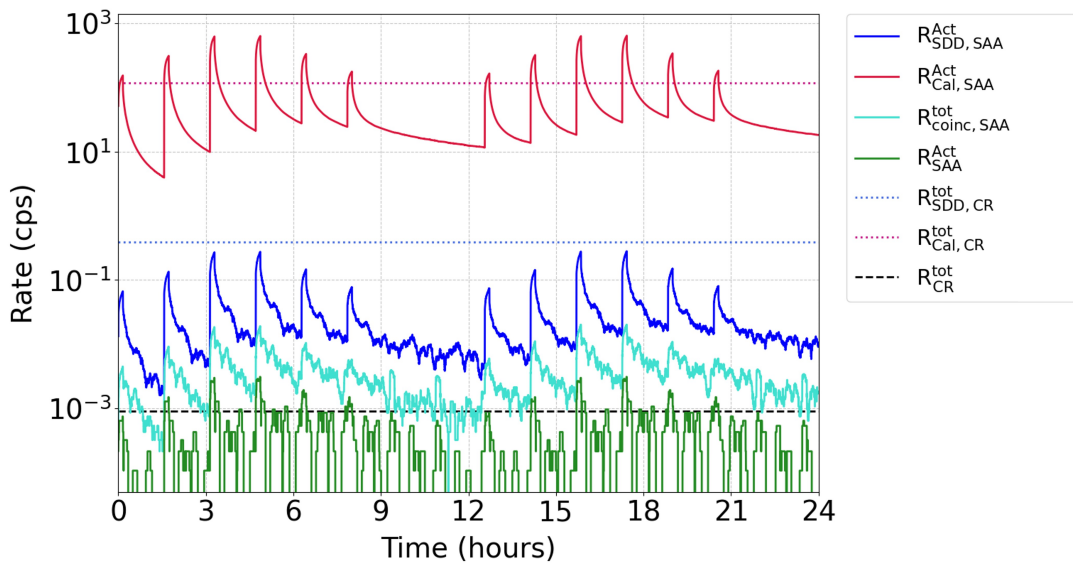


Figure 5.9.: **Temporal evolution of the background rate from activation caused by the SAA for one day.** The rate in the SDD is displayed in blue, and the rate in the calorimeter is drawn in red. Additionally, the rate of coincident events (turquoise) and the remaining background rate from activation after full event selection (green) are shown. The direct cosmic radiation background rates in both detectors are drawn with dotted lines. The final cosmic radiation background rate after event selection is indicated with a dashed black line.

isotopes already decay during or within a few seconds after the SAA transit, leading to an increased rate of activation during this time frame. This increased rate can be identified with the peaks in Figure 5.9 and is also visible after event selection is applied. However, the maximum rate from activation during the SAA is still of the same order of magnitude, or smaller than the direct cosmic radiation rate. Between the SAA transits the decay rate decreases and in general, the SAA activation rate lies one to two orders of magnitude beneath the cosmic radiation rate. The final cosmic radiation background rate after event selection is given with

$$R_{\text{CR}}^{\text{tot}} = 0.88 \text{ mcps} \quad (5.5)$$

This value was also determined, using the cosmic background simulation. The final SAA background rate amounts to at least 10% of the final cosmic radiation background rate for the majority of orbit time. This demonstrates, that the influence of the SAA on the total background in the CubeSat is not negligible.

## 5. The activation study

In order to estimate the average rate from activation due to the SAA, the temporal evolution is extended to one year. This time frame is chosen because the ComPol mission is planned to extend over at least one year in orbit whereas at least 0.5 years can be effectively used to observe Cygnus X-1. The average rate in the detectors, the coincident rate, and the rate after event selection originating from the decay of radioactive nuclei extrapolated to one year in orbit is shown in Figure 5.10. The average values plotted in the figure are obtained by calculating the mean rate over a 12-hour time period. Consequential, the peaks of increased flux during an SAA passage are smoothed. This leads to a conservative estimation of the activation rate  $R_{SAA}^{Act}$  since the detectors will be most likely switched off during the SAA passages. The rate of decays from the SAA increases within the first month in orbit and saturates afterward. After one year in orbit, the final rate of decays from the SAA is obtained:

$$R_{SAA}^{Act} = 0.61 \text{ mcps} \quad (5.6)$$

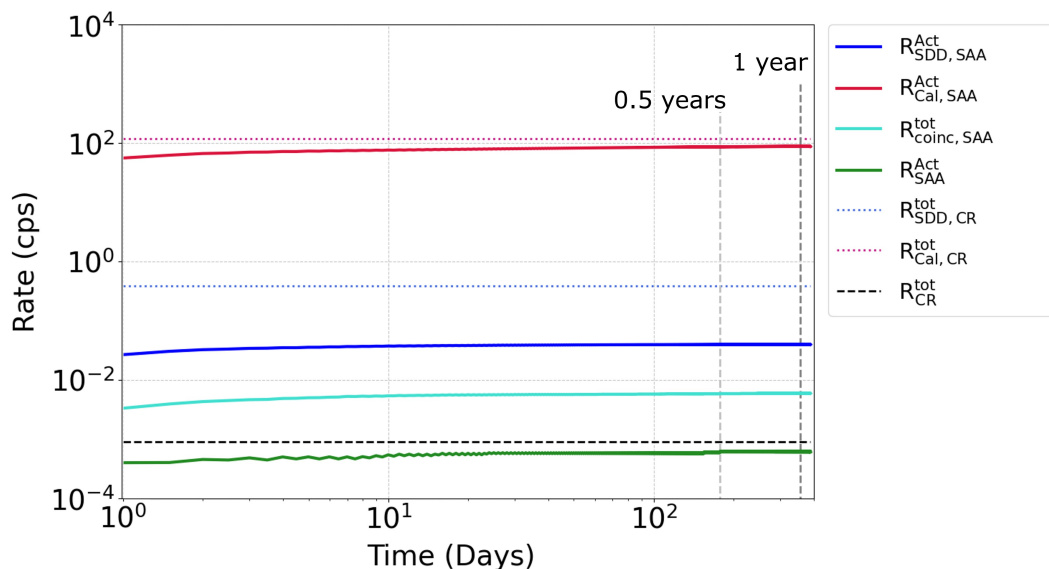


Figure 5.10.: **Averaged temporal evolution of the background rate from activation caused by the SAA for one year.** The rate in the SDD is given in blue, and the rate in the calorimeter is plotted in red. The rate of coincident events (turquoise) and the rate from activation after full event selection (green) are also shown. The cosmic radiation background rates in both detectors are drawn with dotted lines. Additionally, the final cosmic radiation background rate after event selection is indicated with a dashed black line. The time axis is set logarithmic here and the position of 0.5 years, as well as 1 year, is marked with vertical lines.

### 5.3.2. Analysis of the non-excludable background

The origin and exact influence of the activation background from the SAA are investigated further in this section. Figure 5.11 shows the CubeSat components which contribute to the remaining hits from activation after event selection. The lead shielding has the strongest influence here. Followed by the calorimeter and the reaction wheels. This is consistent with

Figure 5.1, since in this section it was shown that, the activation is maximum in these components.

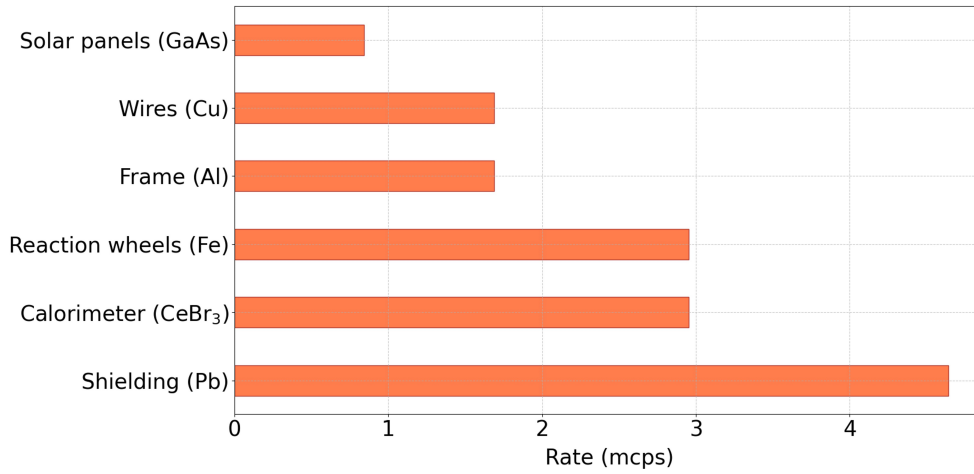


Figure 5.11.: Contributions to the remaining hits from activation after event selection listed by CubeSat component.

The energy spectrum from events due to activation is displayed in Figure 5.12. The figure shows the spectrum in the SDD and calorimeter once concerning all events due to activation (light green and yellow lines). On the other hand, the rate is calculated only by taking into account the events coming from decaying isotopes with a lifetime shorter than 1 year. In other words, only decay products are counted which are generated within 1 year mission time (red and blue lines). For both detectors, the majority of registered events are generated within our mission time. Events from decays with longer half-lives do not contribute significantly to the energy spectrum. The strongest pronounced lines in Figure 5.12 are marked with arrows and their energy is given in the plot. The line features are only visible in the calorimeter, whereas no lines are visible in SDD and coincident events (shown in turquoise) or in the final rate after event selection ( $R_{SAA}^{Act}$ ) (given in green). The lines are assumed to originate from  $\gamma$ -decays of radioactive isotopes created in the CubeSat material. Until this point, only the 511 keV line could be assigned to photons from positron annihilation from  $\beta^+$ -decay (see Figure 5.1). The origin of the other indicated lines could not be mapped to any of the isotopes listed in Table 5.1-Table 5.4 and discussed in Figure 5.1. More research has to be put into the spectrum in the future to identify the creating processes of these lines.

Another feature in Figure 5.12 is a region at approximately 50 keV to 100 keV in the calorimeter spectrum. It is also visible, shifted to slightly higher energies, in the coincident spectrum, and marked with a blue circle in both cases. The energy shift in the coincident spectrum originates from the additional energy from events in the SDD. Concerning this feature more research is also needed. The simulation output needs to be investigated further to find the processes responsible for creating this feature in the coincident spectrum and the line features in the calorimeter.

## 5.4. Combined results and conclusion

In the previous sections, the influence of activation by the cosmic radiation and the SAA were considered in great detail. Both background sources activate the CubeSat material in the

## 5. The activation study

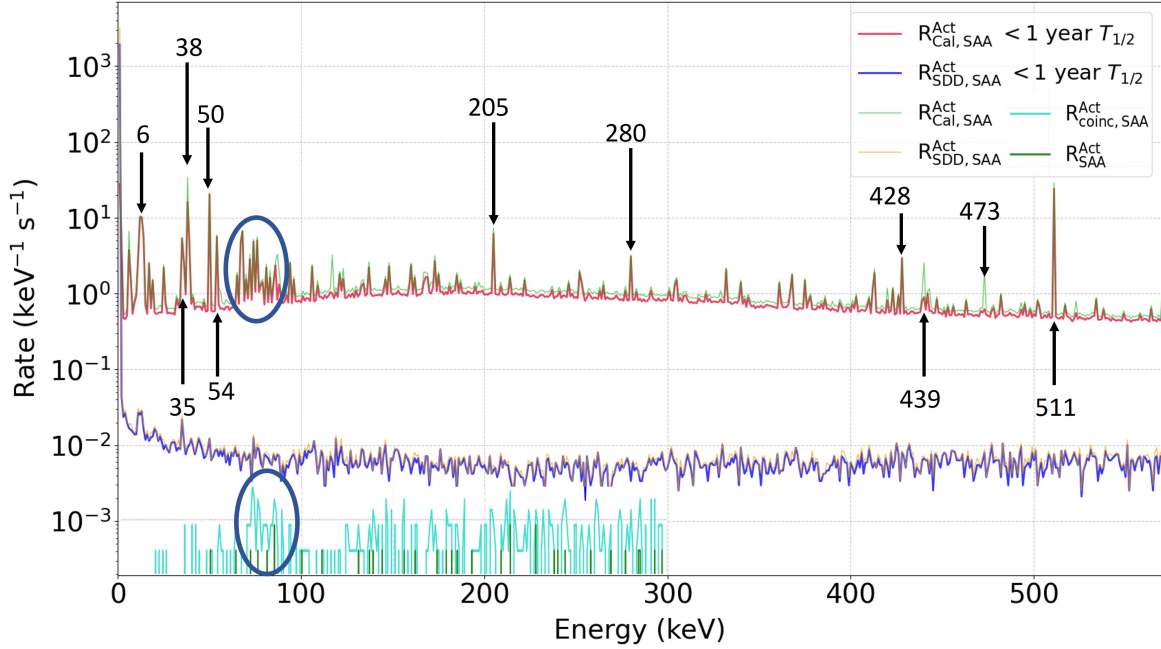


Figure 5.12.: **Energy spectra from events due to activation.** The spectra in the SDD and calorimeter are given taking into account only events from decays happening within a half-life of 1 year (red and blue) and in total (yellow and green). The coincident, and final rates (shown in turquoise and green) are given with regard to all events due to activation independent of their isotope’s lifetime. The most prominent line features are marked with arrows or circles. Their respective energy is written in the plot.

progress of the mission. It was found that the lead shielding, the  $\text{CeBr}_3$  detector, and the reaction wheels made of iron have the highest activation rate. The isotopes produced and their most common decay channels were studied in depth (see [subsection 5.2.1](#)). Furthermore, the rates of the cosmic radiation and the SAA caused by activation were calculated. These can now be used in [Equation 3.3](#) to calculate a final background rate. The calculation is shown in [Equation 5.7](#):

$$R_{\text{BG}} = R_{\text{CR}}^{\text{dir}} + R_{\text{CR}}^{\text{Act}} + R_{\text{SAA}}^{\text{Act}} \quad (5.7)$$

$$1.49 \text{ mcps} = 0.88 \text{ mcps} + 2.61 \text{ } \mu\text{cps} + 0.61 \text{ mcps} \quad (5.8)$$

Using [Equation 2.5](#) the Signal-to-Noise Ratio can be calculated. The signal rate  $R_S$  corresponds to the rate from Cygnus X-1 after the event selection is applied. This rate is obtained via a signal simulation with the Cygnus X-1 spectrum as described in [section 4.2](#).

$$R_S = 0.34 \text{ mcps} \quad (5.9)$$

The final SNR is displayed in [Equation 5.10](#) in comparison to the SNR before the activation analysis is applied and the influence of the SAA was not taken care of.

$$\text{SNR}_{\text{no SAA}} = 0.38 \quad \text{SNR}_{\text{incl. SAA}} = 0.23 \quad (5.10)$$

The final sensitivity of the Compton telescope is calculated via [Equation 2.6](#). The final result after 0.5 years of observation is again shown in comparison to the MDP without the influence of the SAA.

$$\text{MDP}_{\text{no SAA}} = 15.6\% \qquad \text{MDP}_{\text{incl. SAA}} = 19.1\% \qquad (5.11)$$

The sensitivity of the telescope is thus highly dependent on the activation induced by the SAA. The impact of the SAA can be reduced by minimizing the time the satellite spends in this region. This can be done by choosing another orbit with a lower inclination ( $i < 85^\circ$ ). However, it depends strongly on the launch provider and their capacity which orbits can be targeted. Therefore, this task has to be taken into account as soon as the launch provider is chosen. The best option would be to target an equatorial orbit ( $i \sim 0^\circ$ ) where the transit of the SAA can be avoided completely. This would result in an MDP of 15.6% after 0.5 years of data taking. Any orbit with inclination  $> 0^\circ$  but  $< 85^\circ$  will result in a final sensitivity between 15.6% and 19.1%.

Additionally, the design of the shielding can reduce the total background rate. Improving the shielding geometry will reduce the direct rate from cosmic radiation  $R_{\text{CR}}^{\text{dir}}$ , however, it has also an effect on the rate due to activation. In [chapter 6](#) different approaches to optimize the shielding are investigated.



## 6. The shielding study

The total background rate can be reduced by optimizing the shielding strategy.

On the one hand, the shielding efficiency depends on the geometry of the shielding. A general approach to suppress the direct background ( $R_{\text{CR}}^{\text{dir}}$ ) as effectively as possible, is to add more shielding around the detectors. This can be done by surrounding the whole detector system as tight as possible with shielding material. Additionally, the shielding effectiveness is increased by building the shielding as thick as possible. However, the overall mass and size constraints in the CubeSat do not leave much room for heavy and thick shielding. The shielding thickness is therefore limited to a few millimeters. In contrast, increasing the amount of material around the detectors will lead to more activated material and thus radioactive decays, which are likely registered by the detectors. Placing a huge amount of lead close to detectors will increase the background rates due to activation ( $R_{\text{CR}}^{\text{Act}}$  and  $R_{\text{SAA}}^{\text{Act}}$ ). In [section 6.1](#) the geometry of the shielding is varied and simulations with the cosmic radiation and SAA are performed in order to determine the optimal solution for the shielding geometry. The shielding material is always chosen to be lead in this section.

On the other hand, the material used for the shielding also strongly influences its effectiveness. The shielding material should be chosen in a way to attenuate the most abundant background particles as efficiently as possible. Additionally, the shielding material should be rather robust against cosmic radiation to minimize the background rate due to activation. In [section 6.2](#) the material used for the shielding is varied and simulations with the cosmic radiation background are performed in order to find the best material for the shielding. The respective rates are obtained in analogy to the analysis performed in [chapter 5](#).

In both sections mentioned above, simulations with cosmic radiation are carried out in the first step to determine the direct background rate  $R_{\text{CR}}^{\text{dir}}$ . All geometries or materials are compared with respect to their direct background shielding efficiency. The rate due to activation  $R_{\text{CR}}^{\text{Act}}$  is also determined and used as a comparative parameter. In the second step, selected geometries or materials are simulated with the SAA background to calculate the influence of the activation by the SAA  $R_{\text{SAA}}^{\text{Act}}$ . This and the total rate  $R_{\text{BG}}$ , resulting from the sum of all background rates, are again discussed comparatively to find the best geometry as well as the best material.

The third section in this chapter gives an outlook on further shielding concepts which could be explored more deeply in the future. The concepts are introduced and some first considerations are presented.

### 6.1. Shielding study for different geometries

In the course of this thesis, six different shielding geometries were simulated and compared to each other. All investigated geometries are shown in [Figure 6.1](#). The geometries can be separated into three groups. For the first group, the focus lies on the collimator and its length is varied. The second group focuses more on the shielding plate and varies its position and form. The collimator is set at the standard length of 10 cm for these simulations. The last group consists only of the simulation performed without any shielding at all to obtain

## 6. The shielding study

a maximum direct background rate and a minimum background rate from activation. The "10 cm Collimator"-geometry is also referred to as "Standard geometry" and was investigated in detail in [chapter 5](#). The sides of the shielding case in the "Shielding Case"-geometry are set to a thickness of 1.5 mm. This is the largest possible thickness, due to the size constraints of the CubeSat.

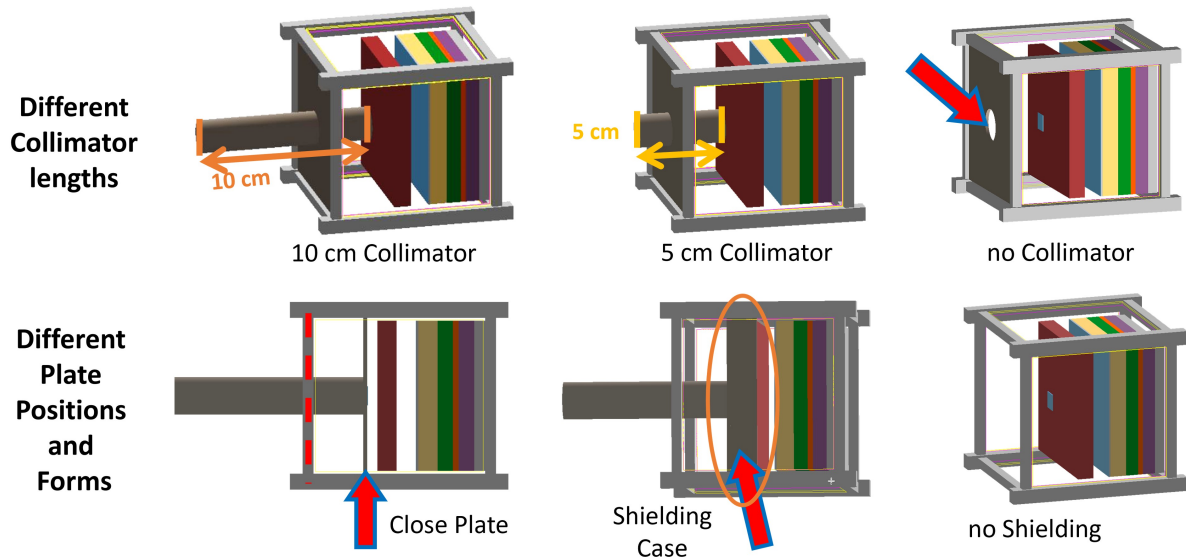


Figure 6.1.: **Sketches of all simulated shielding geometries.** The colors are chosen analogous to [Figure 4.1](#). The first row shows the different collimator lengths. The different variations of the shielding plate are shown in the second row. A geometry with no shielding at all was also simulated and is shown as the last sketch in the second row. The shielding plate is always implemented with a thickness of 2 mm. The collimator has a thickness of 2.5 mm. In the "Shielding Case"-geometry, the sides of the case have a thickness of 1.5 mm.

### 6.1.1. Analysis of remaining background events after event selection

The rate of background particles after event selection is investigated comparatively. Hereby, as a first step, the starting positions of the remaining background particles on the surrounding sphere are examined in greater detail. The background is simulated in Geant4 via a surrounding sphere as particle source (see [section 4.2](#)). Each background particle is assigned a starting position on a spherical surface around the CubeSat system from where it is emitted. The determination of the starting positions of the background particles provides important information about the effectiveness of the shielding. Furthermore, it can be deduced where additional shielding material has to be placed to further shield the background. Another aspect is to determine how effectively different collimator lengths shield the background particles.

In the starting positions of all background particles for the geometry, "no Collimator" is shown in detail in [Figure 6.2](#). Here, different regions are highlighted to illustrate the reasons why shielding fails at certain locations. The pink region shows an area on the surrounding sphere where background particles are emitted, pass through the hole in the shielding plate

and subsequently interact with the detectors. This area can be narrowed down by making use of a collimator. The blue shaded region indicates the starting positions of background particles traveling past the shielding plate before reaching the detectors. The limiting factor for this region is the shielding plate on one hand, and the sidelength of the calorimeter on the other hand. The shielding plate does not affect particles originating from this area. This area can be reduced by placing the shielding plate closer to the detectors or adding extra shielding at the sides.

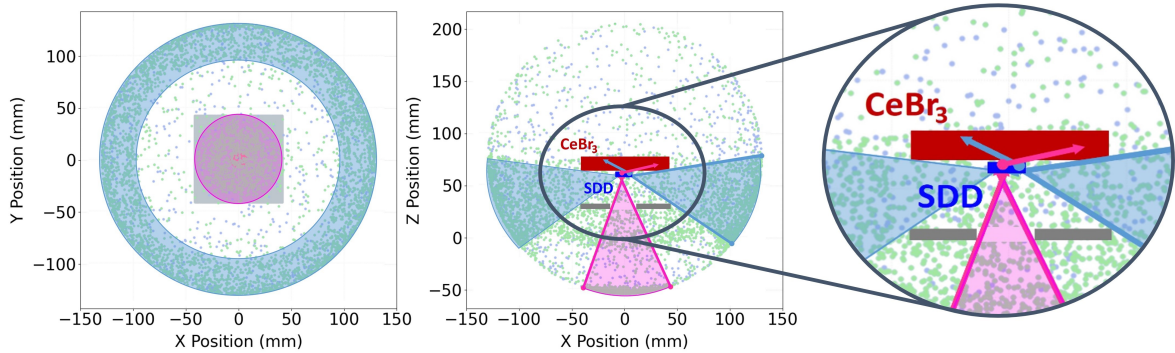


Figure 6.2.: **Origins of background events after event selection for the "no Collimator"-geometry plus a zoom into the detector region.** The area from where background particles are emitted, and subsequently pass through the hole in the shielding plate is highlighted in pink. The blue shaded region shows the starting positions of background particles that travel past the shielding plate before reaching the detectors. The particles, which directly interact in the detectors are marked in blue. The particles, which are scattered in the shielding before reaching the detectors are marked in green. The shielding plate is depicted in grey.

The scatterplots in [Figure 6.3](#) qualitatively demonstrate the attenuation ability of all simulated shielding configurations in comparison (except the "no Shielding"-geometry). The highlighting of different regions has been omitted here. The starting positions are marked in green if the background particle did not have any interaction in the shielding at all before it is registered in the detectors. The starting positions of the particles, which interact in the shielding, but are able to pass through it or generate secondaries that interact in the detectors, are indicated in blue. The number of hits decreases with increased shielding volume, showing to be the lowest for the "Shielding Case"-geometry. The shift of the shielding plate directly in front of the SDD detector already improves the shielding efficiency. This improvement is mainly accomplished by decreasing the number of particles that have no interaction in the shielding.

A quantitative analysis of the results shown in [Figure 6.3](#) is displayed in [Table 6.1](#). The table gives an overview of the background rates for all investigated shielding geometries. The overall background rate decreases with regard to the improved shielding geometry (2<sup>nd</sup> column). This decrease is mainly due to the decrease of background particles which have no interaction in the shielding (3<sup>rd</sup> column). The respective rate corresponds to all particles

## 6. The shielding study

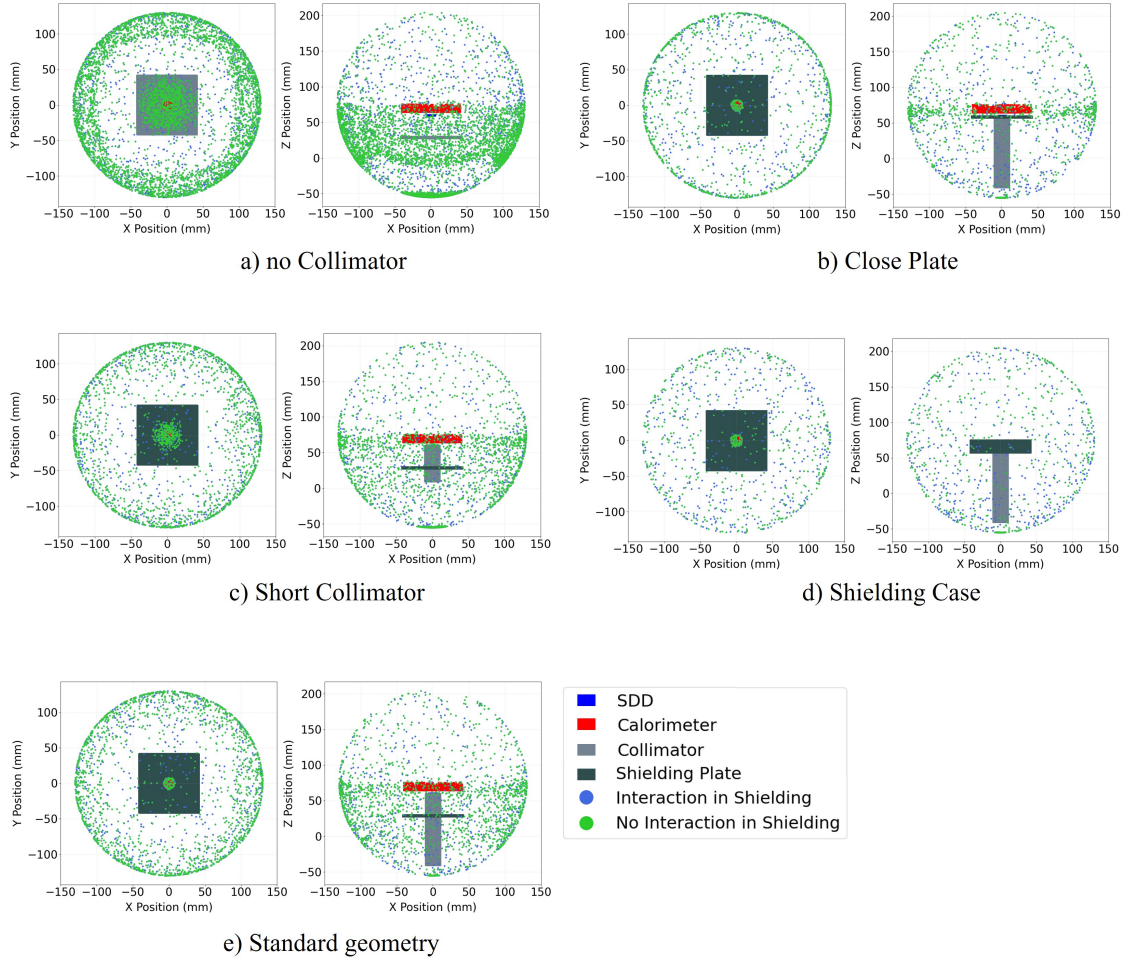


Figure 6.3.: **Origins of background events after event selection for five geometries.** The origin of background particles lies on a spherical surface surrounding the CubeSat. The figures show the top view along the z-axis on the simulated system and a side view along the y-axis.

The particles, which directly interact in the detectors are marked in blue. The particles, which are scattered in the shielding before reaching the detectors are marked in green. The shielding plate and the collimator are drawn in grey tones. The detectors are indicated in blue (SDD) and red (calorimeter). **a)** shows the "no Collimator"-geometry, the "Close Plate"-configuration is given in **b)**. **c)** illustrates the "5 cm Collimator"-geometry, and the "Shielding Case"-geometry is depicted in **d)**. The "10 cm Collimator"-configuration is also called Standard geometry and is shown in **e)**.

indicated with green marks in Figure 6.3. The overall rate corresponds to the sum of all blue and green marks in Figure 6.3 and is given as the sum of  $R_{CR}^{dir}$  and  $R_{CR}^{Act}$ . The rate of particles from the backside stays nearly constant for the geometries "5 cm Collimator", "10 cm Collimator", and "Close Plate" (4<sup>th</sup> column). This is expected since the shielding geometry is only changed in front of the detectors (lower half of the surrounding sphere) and no extra shielding is added from behind (upper half of the surrounding sphere). Only

the "Shielding Case"-geometry has the capability to shield a small number of particles from behind, due to its side coverings. This is visible in the slightly lower rate of particles from the backside. For the "no Collimator"-geometry an increased rate from the backside is obtained. A possible explanation is given by secondary particles created in the shielding plate which afterward interact with the detectors. These secondaries can be created by particles entering the shielding plate from the backside (from above in [Figure 6.3](#)). They can leave the shielding plate again in direction of the SDD detector and due to the missing collimator, they cannot be absorbed before reaching the detector. Generally speaking, the CubeSat's components behind the detector system (electronics, battery, onboard computer, etc.) also act as a good shielding and lower the rate of particles hitting the detector from behind. The calorimeter itself also acts as shielding for the SDD detector. Most photons entering the calorimeter from behind are absorbed and do not reach the SDD detector. Higher energetic photons may pass through the CubeSat material and the calorimeter before interacting in the SDD. Applying an upper energy threshold at 300 keV during event selection will disfavor any higher energetic events which could pass through the satellite material from behind. This can be seen in [Figure 6.3](#) since the upper half of the surrounding sphere indicated a lower density of particles for all geometries. The influence of the collimator is given by the rate of particles, which pass directly through the collimator (or the hole in the shielding plate) without interaction in the shielding (5<sup>th</sup> column). This corresponds to the pink region shown in [Figure 6.2](#). Its rate decreases for geometries with longer collimators and stays constant for all geometries with a 10 cm collimator.

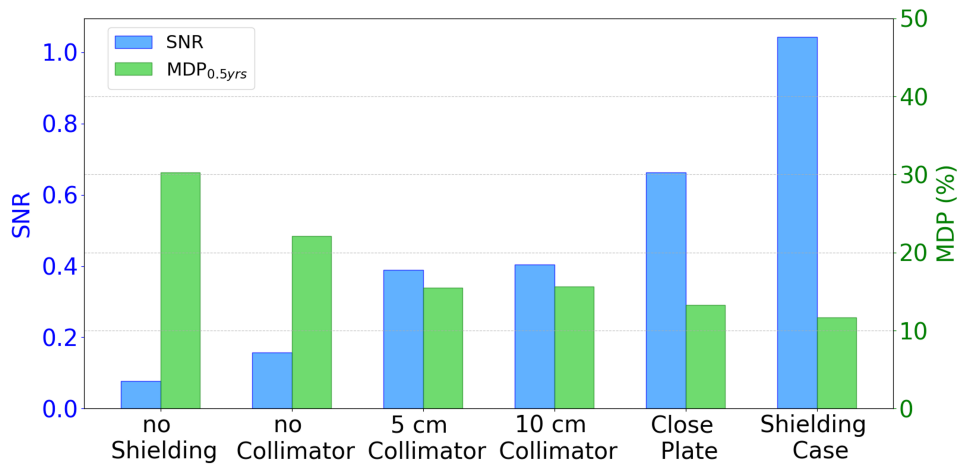
Table 6.1.: **Background rates for all analyzed geometries.**

Geometry	Rate (mcps)			
	After event sel. – ALL	No Interaction in shielding	From the backside	Directly through the Collimator
no Collimator	2.14	1.79	0.27	0.382
5 cm Collimator	0.89	0.69	0.19	0.105
10 cm Collimator	0.88	0.65	0.20	0.025
Close Plate	0.54	0.38	0.19	0.025
Shielding Case	0.35	0.20	0.16	0.026

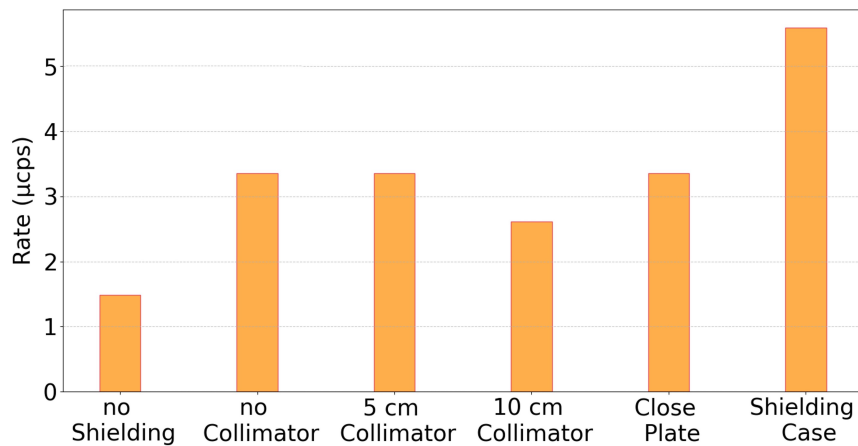
The SNR (see [Equation 2.5](#)) and the sensitivity (MDP) (see [Equation 2.6](#)) of the telescope can be calculated using the background rates ( $R_{CR}^{dir}$ ) for all simulated geometries and is shown in [Figure 6.4a](#). Furthermore, the activation rate ( $R_{CR}^{Act}$ ) is depicted in [Figure 6.4b](#) and was obtained analogue to [subsection 5.2.2](#). The activation depends on the amount of material around the detector system and thus is not equal for all geometries.

The SNR increases from 0.08 ("no Shielding") to 1.04 ("Shielding Case") with adding more shielding close around the detectors. This trend is expected, due to the decrease in the total background rate which was obtained in [Figure 6.3](#) and [Table 6.1](#). The signal rate stays constant for all geometries and does not affect the SNR and MDP. The MDP follows the same trend as the SNR and is the best (smallest) for the "Shielding Case"-geometry with 11.7%. This is an improvement of 3.9% compared to an MDP of 15.6% in the standard "10 cm Collimator"-geometry.  $R_{CR}^{Act}$  is of the order of  $\mu$ cps for all geometries and thus has no relevant influence on the total background rate since the direct background is approximately

6. The shielding study



(a) SNR, MDP after 0.5 years observation time for all shielding geometries.



(b)  $R_{CR}^{Act}$  for all shielding geometries.

Figure 6.4.: **SNR, MDP and  $R_{CR}^{Act}$  for all shielding geometries.** a) shows the SNR and MDP after 0.5 years for all shielding geometries. The SNR is shown in blue and indicated by the left y-axis, the MDP is depicted in green and refers to the right y-axis. The gridlines correspond to the right y-axis. b) depicts the background rate due to activation originating from the cosmic radiation  $R_{CR}^{Act}$ .

100 times larger (see subsection 5.2.2). The values for SNR, MDP and  $R_{CR}^{Act}$  are compared qualitatively in the following paragraph.

The rate due to activation is nearly equal for the geometries "no Collimator", "5 cm Collimator", "10 cm Collimator", and "Close Plate". For the "no Collimator"-geometry the  $R_{CR}^{Act}$  is the smallest due to the absence of activated material close to the detectors. In contrast, the absence of shielding leads to a strong increase in the direct background rate, which results in the worst SNR and sensitivity. The "Shielding Case"-geometry shows the highest rate due to activation, due to the most material directly in front and around the detectors. However, the advantage of general background suppression outweighs the increase of  $R_{CR}^{Act}$  leading to the "Shielding Case"-geometry as the best option followed by the "Close Plate"-geometry.

Comparing the different collimator lengths shows that the absence of a collimator decreases the sensitivity due to the increased background rate. The collimator length instead does not have a huge impact, since the SNR and MDP, as well as  $R_{CR}^{Act}$  are nearly equal for the "5 cm Collimator"- and "10 cm Collimator"-geometries. The final collimator length should be between 5 cm and 10 cm but has to be chosen with regard to the size and space constraints of the final CubeSat setup.

### 6.1.2. Shielding efficiency with the SAA background included

In subsection 6.1.1 only the cosmic radiation is considered as background source. As shown in section 5.4 the effect of the SAA due to activation is not negligible and has to be taken into account for all relevant geometries. The geometries "10 cm Collimator", "Close Plate", and "Shielding Case" are simulated with the SAA background. These geometries were chosen since they performed best concerning the cosmic radiation background. The "no Shielding" geometry is also simulated with the SAA spectrum to provide a reference for the CubeSat without any shielding. The contribution of the cosmogenic activation due to the SAA is depicted in Figure 6.5. The rates  $R_{CR}^{dir}$ ,  $R_{CR}^{Act}$  and  $R_{SAA}^{Act}$  are shown for the four simulated geometries in a stacked barplot. The  $R_{SAA}^{Act}$  was obtained following the approach explained in section 5.3. The  $R_{CR}^{Act}$  is two to three orders of magnitude smaller than  $R_{CR}^{dir}$  and  $R_{SAA}^{Act}$  and does not play a role for the total background. All Rates are given in Table 6.2.

Table 6.2.: **Total background rate  $R_{BG}$  and components from the cosmic radiation and SAA for four different geometries.** The contribution of the SAA to  $R_{BG}$  is given in percent in the 6<sup>th</sup> column.

Geometry	$R_{CR}^{dir}$	$R_{CR}^{Act}$	$R_{SAA}^{Act}$	$R_{BG}$	$\frac{R_{SAA}^{Act}}{R_{BG}}$
no Shielding	4.24 mcps	1.49 $\mu$ cps	0.07 mcps	4.31 mcps	1.6 %
10 cm Collimator	0.88 mcps	2.61 $\mu$ cps	0.61 mcps	1.49 mcps	40.9 %
Close Plate	0.54 mcps	3.36 $\mu$ cps	0.67 mcps	1.21 mcps	55.2 %
Case	0.35 mcps	5.59 $\mu$ cps	0.94 mcps	1.30 mcps	72.6 %

The effect of the SAA is clearly visible in the geometries "10 cm Collimator", "Close Plate", and "Shielding Case". The SAA contributes over 40% to the total background rate. For the "Close Plate"-, and "Shielding Case"-geometry the activation due to the SAA is the main background source. The impact of the SAA on the SNR and the telescope's sensitivity after

## 6. The shielding study

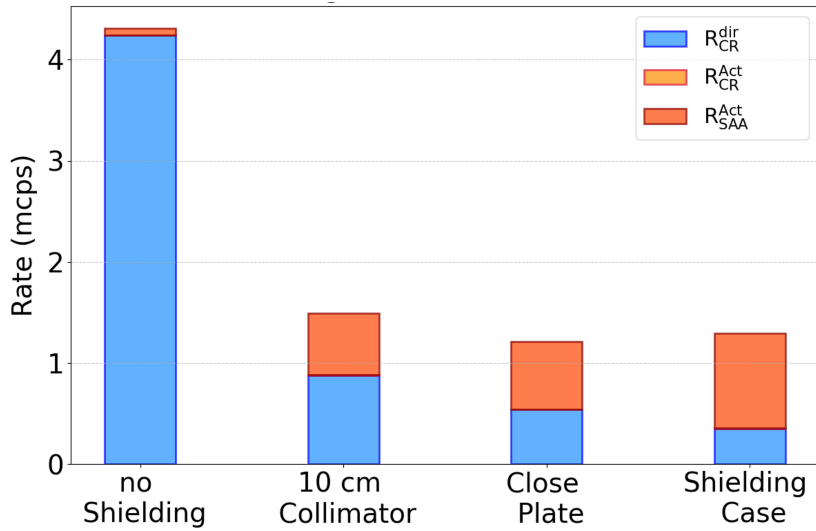


Figure 6.5.: **Background contributions for four different geometries in a stacked barplot.** The total background consists of  $R_{CR}^{dir}$ ,  $R_{CR}^{Act}$  and  $R_{SAA}^{Act}$  as explained in section 3.3. The values for  $R_{CR}^{Act}$  are three orders of magnitude smaller than  $R_{CR}^{dir}$  and  $R_{SAA}^{Act}$  and cannot be resolved in the plot.

half a year of data taking are illustrated in Figure 6.6. The results are plotted together with the SNR and MDP without the SAA-background for comparison..

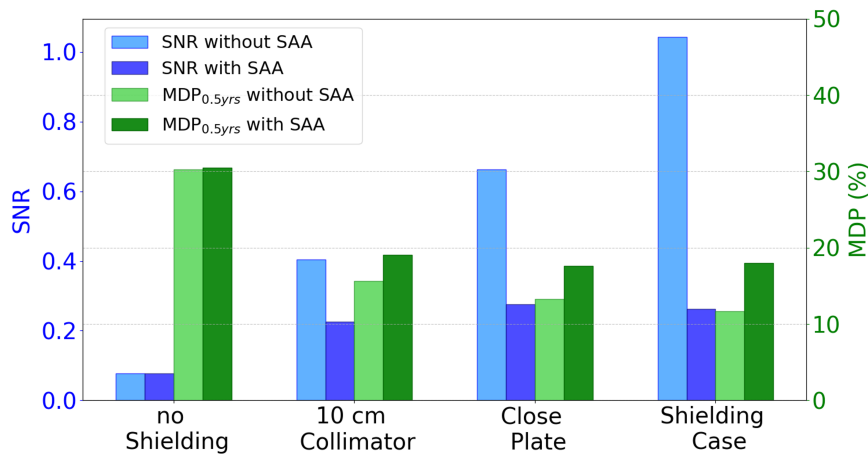


Figure 6.6.: **Comparison of SNR and MDP before and after the SAA contribution for four different geometries.** The values without the SAA are displayed in light blue (SNR) and light green (MDP), while the final values with the SAA-activation included are shown in dark blue (SNR) and dark green (MDP). The gridlines are aligned with the right y-axis.

Despite a significant contribution from the SAA activation, the overall sensitivity is improved for all configurations with shielding. The influence of the SAA on the "no Shielding"-geometry

in contrast is negligible. The activation due to the SAA contributes only to 1.6% to the overall background (see Table 6.2) which is reflected in a nearly equal SNR and MDP with and without the SAA included. The reduction of the SNR and the increase in MDP (worse sensitivity), compared to the case without SAA, is most prominent in the "Shielding Case"-geometry because of the strong increase in SAA-activation induced background (72.6% of the total background rate). The final SNR and MDP inclusive the SAA-activation are listed in Table 6.3.

Table 6.3.: **Final SNR and MDP after 0.5 years of data-aquisition for four different geometries.**

Geometry	SNR	MDP <sub>0.5 yrs</sub>
no Shielding	0.08	30.5 %
10 cm Collimator	0.23	19.1 %
Close Plate	0.28	17.6 %
Case	0.26	18.0 %

The final sensitivity after 0.5 years of measurement lies between 17.6% and 19.1% of minimum detectable polarization for all geometries with shielding. The configuration without any shielding has a sensitivity of 30.5%, which demonstrates the advantage of adding shielding to the telescope.

The best sensitivity can be achieved with the "Close Plate"-geometry, which improves the sensitivity from 19.1% to 17.6% compared to the "10 cm Collimator"-geometry which was investigated in chapter 5. This "Standard geometry" was constructed as the first approach for the sensitivity and shielding study. However, shifting the shielding plate close to the SDD detector improves the final sensitivity by 1.5%.

### 6.1.3. Summary and conclusion

The aim of this section was to find alternative shielding geometries, in order to improve the final sensitivity of the Compton telescope. After comparing various configurations of shielding geometries the following results are obtained:

- The position of the shielding with respect to the detectors has a visible impact on the direct background rate. Placing more shielding around the detectors improves the telescope's sensitivity by blocking direct interactions from background particles in the detectors.
- The presence of a collimator improves the sensitivity as well due to a reduction of background particles entering the detectors from the same direction as the Cygnus X-1 X-rays. The length of the collimator should lie between 5 cm and 10 cm.
- The SAA has a crucial influence on the overall background rate for all configurations with additional shielding. The SAA-activation-induced background rate contributes from 40% up to 73% to the overall background rate.
- Adding no extra shielding leads to the highest total background rate due to the direct background from cosmic radiation. Hence, the "no Shielding"-geometry is the worst option.

## 6. The shielding study

- The final sensitivity lies between 17.6% and 19.1% minimum detectable polarization after 0.5 years of data-taking for all configurations with extra shielding.
- The best performance can be achieved with the "Close Plate"-geometry, leading to an MDP of 17.6% after 0.5 years of measurement.

In the following section the "Close Plate"-geometry will be considered further.

### 6.2. Shielding study for different materials

In [section 6.1](#), the best option for a shielding geometry is found. After comparing different configurations of shielding arrangements with regard to the cosmic radiation and SAA, the "Close Plate"-geometry (c.f. [Figure 6.1](#)) is determined to perform best. This geometry is now investigated under the aspect of varying the shielding material. In all previous chapters, the shielding material is chosen to be lead. Due to its high density, lead is commonly used as a radiation shielding material to shield against X-rays and  $\gamma$ -rays.

Since lead is difficult to process, this material should be avoided if possible. In addition, the cosmogenic activation in lead is rather high, as it has a high scattering cross-section for protons due to its high atomic number. Furthermore, many secondary particles (namely neutrons) are generated in lead from scattering with cosmic protons. This leads to a possible increase of the activation in the material itself or the CeBr<sub>3</sub> detector [[41](#)]. For these reasons, it is of interest to explore alternative shielding materials.

After conducting a thorough analysis of the most dominant background particles, the alternative shielding materials are chosen in [subsection 6.2.1](#), and their impact on the telescope's SNR and sensitivity is investigated in [subsection 6.2.2](#).

#### 6.2.1. Choice of shielding materials

As explained in [section 3.2](#) the background consists of the cosmic radiation and the SAA. The cosmic radiation is composed of photons, electrons, positrons, protons, neutrons,  $\alpha$ -particles, and heavier nuclei which contribute to the direct background rate to varying degrees. Heavier nuclei than  $\alpha$ -particles are not considered in this work due to their small abundances. In order to find the best shielding material, it is necessary to determine the main background particles against which the shielding should be efficient have to be determined. Since the SDD detector is sensible on photons and electrons, these particles are most likely to cause a background.

In [Figure 6.7](#) the distribution of the background particle types that remain after event selection is shown. It should be noted that the initial background particles, which come from the universe or the atmosphere, are not necessarily the same particles that interact in the detector. Often secondary particles (mainly electrons and photons, and neutrons to some extent) are created, which then undergo the subsequent interaction in the detector. The secondary particles are not considered in [Figure 6.7](#). A more detailed analysis of the spectra of the background particles in the detectors can be found in [[1](#)]. The figure indicates, that cosmic photons have the strongest contribution to the direct background rate ( $R_{\text{CR}}^{\text{dir}}$ ). The second strongest contribution is provided by positrons. However, the effect of secondary particles has to be considered in this case. The positrons annihilate in the CubeSat's material and generate 511 keV photons, which are eventually registered in the detectors. This 511 keV line is significantly pronounced in the calorimeter spectrum (c.f. [Figure A.10](#)). Additional shielding is not necessarily effective against these photons, since the annihilation can happen

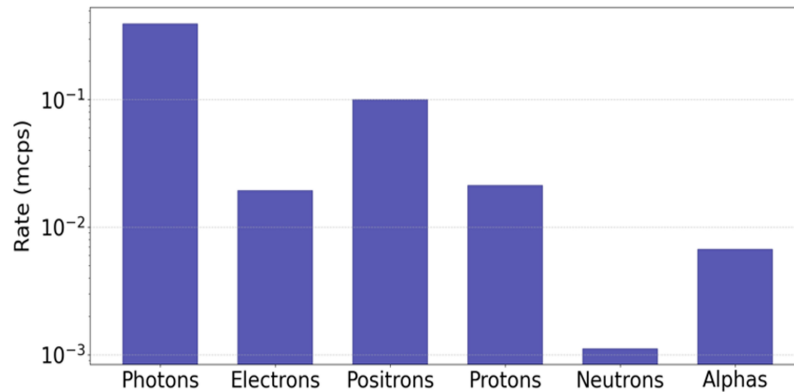


Figure 6.7.: **Initial particles after event selection.** The results are obtained only considering the cosmic radiation background.

in the shielding structure itself, as well as anywhere in the outer CubeSat’s material. Thus, regarding cosmic radiation, the focus on shielding lies in the task to shield cosmic photons, which would otherwise directly interact with the detectors. Considering photon shielding, the crucial parameter for the chosen material is density. The higher the density, the better will the material shield against photons.

With regard to the SAA, the possible background particles are decay products, namely photons from  $\gamma$ -decays and electrons and positrons (or annihilation photons) from  $\beta$ -decays.  $\alpha$ -particles from decays in the shielding do not count, since they have a low penetration depth. They contribute exclusively via secondary electrons and photons. A detailed view on the influence of decay products on the background rate was performed in [subsection 5.2.1](#) (in general) and [subsection 5.3.2](#) (for the SAA). As seen in [section 6.1](#), additional shielding is a strong source of this background. However, changing the shielding material can lead to a decrease in the activation rate.

The aspects discussed above lead to different shielding materials, which were selected for further simulations. The main considerations, as well as the resulting materials of interest, are listed below:

- The materials should be easy to work with (and be affordable in the required quantity).  
→ aluminum, copper
- The materials should have a high attenuation coefficient for photons and a high density.  
→ tantalum, lead
- The material should have a low activation rate.  
→ aluminum, tin

The shielding materials aluminum, copper, tin, and tantalum were chosen to be investigated further. The lead shielding plate and collimator are therefore replaced by a plate and collimator of the particular material. In each geometry, the thickness of the shielding plate is adjusted to keep the mass of the plate the same as in the lead configuration. The same applies to the wall thickness of the collimator. The masses of the shielding plate and the collimator are given below:

$$m_{\text{ShieldingPlate}} = 148.0 \text{ g} \qquad m_{\text{Collimator}} = 156.0 \text{ g} \qquad (6.1)$$

## 6. The shielding study

The resulting thicknesses for all materials are given in [Table 6.4](#).

Table 6.4.: **Thicknesses of the shielding plate and the collimator wall for each material.** Each thickness value corresponds to the mass equivalent of the original lead shielding.

Material	Shielding Plate thickness (mm)	Collimator thickness (mm)
Aluminum	8.6	8.0
Copper	2.6	3.1
Tin	3.5	4.0
Tantalum	1.4	1.8
Lead	2.0	2.5

To sum up, additional simulations were carried out with the cosmic radiation background using the shielding materials aluminum, copper, tin, and tantalum. The shielding efficiency of the individual materials is analyzed in more detail in the following [subsection 6.2.2](#). Furthermore, the sensitivity (MDP) and the SNR from the simulations of the different shielding materials are calculated and then compared with the lead configuration and the geometry without shielding in [subsection 6.2.3](#).

### 6.2.2. Shielding efficiency of different materials

In order to estimate the shielding property, the attenuation coefficients for photons for all used materials are illustrated in [Figure 6.8](#). The graphs were calculated with the Beer-Lambert law given in [Equation 6.2](#) for the attenuation of photons in matter [42]. The initial photon intensity is given with  $I_0$ , the final intensity is labeled with  $I_{\text{fin}}$ . The attenuation coefficient is given with  $\mu$  and  $d$  describes the thickness of the material.

$$I_{\text{fin}} = I_0 \cdot e^{-\mu d} \quad (6.2)$$

The thicknesses for the shielding plate are used in [Figure 6.8](#). The analogous figure for the collimator is shown in [subsection A.5.1](#). The energy range is chosen to include the range of interest (11 keV to 300 keV) and also considers higher energetic photons in the range up to 800 keV. [Figure 6.8](#) shows that lead has the best attenuation properties, closely followed by tantalum. From the aspect of photon attenuation, these two materials are the most suitable for shielding. This is also shown in [Figure 6.9](#). Here, the attenuation is shown over the thickness of a lead shielding for different initial photon energies. Already at a thickness of 2 mm of the shielding plate, the intensity of 200 keV photons is attenuated to 10% of their initial intensity. 68% of the intensity at 300 keV is shielded by the collimator. Further figures analogous to [Figure 6.9](#) considering the other investigated materials are given in [subsection A.5.1](#).

To complete the considerations about the shielding material, a closer look is taken at the spectra in the detectors to find out whether the fluorescence lines of the different shielding materials contribute to the background rate. Fluorescence lines range from 1 keV to approximately 100 keV and hence are in our region of interest. They are emitted during the deexcitation of ionized atoms. A material is ionized by being hit with  $\gamma$ -rays, ejecting one or

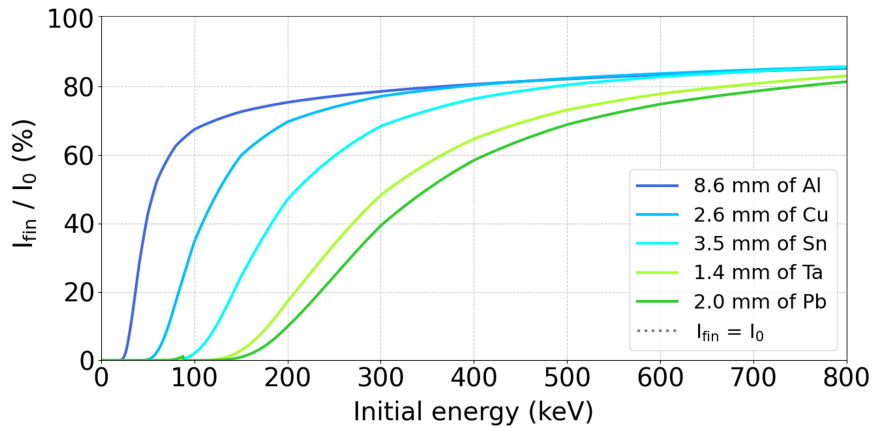


Figure 6.8.: **Final intensity vs. initial energy for all simulated shielding plate materials.** The thickness of the shielding plate for each material is given in the legend. Each thickness corresponds to the mass equivalent of a 2 mm lead shielding.

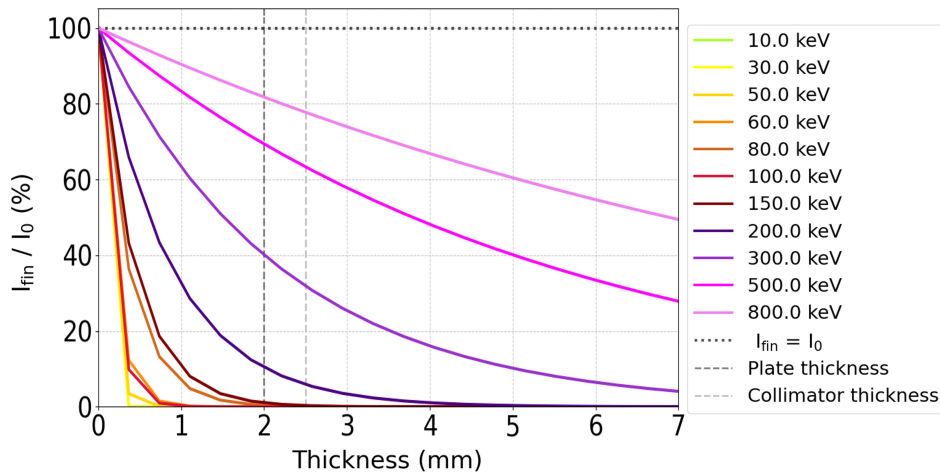


Figure 6.9.: **Dependence of the final photon intensity on the thickness of the lead shielding for different initial photon energies.** The shielding plate thickness is marked with a grey dashed vertical line at 2.0 mm. The thickness of the collimator wall is shown with a dashed line in light grey and is set to 2.5 mm.

more of its electrons from its orbital(s), leaving the respective orbital(s) unoccupied and thus the atom in an excited state. During deexcitation, the orbitals are reoccupied by electrons from higher levels and the characteristic fluorescence photons are emitted with distinct energy depending on the energetic difference of the respective orbitals. Fluorescence lines generated in the shielding contribute to our background and cannot always be rejected during event selection. In Table 6.5 the  $K_\alpha$  and  $K_\beta$  lines of the investigated materials are listed. In addition, the fluorescence lines of silicon (SDD), cerium, and bromine (calorimeter) are shown.

6. The shielding study

Table 6.5.: Fluorescence lines ( $K_{\alpha 1}$ ,  $K_{\alpha 2}$ ,  $K_{\beta}$ ) of all investigated shielding materials.

Material	$K_{\alpha 1}$ (keV)	$K_{\alpha 2}$ (keV)	$K_{\beta}$ (keV)
Aluminum	1.5	1.5	1.6
Copper	8.0	8.0	8.9
Tin	25.3	25.0	28.5
Tantalum	58.0	58.0	67.2
Lead	75.0	72.8	84.9
Silicon (SDD)	1.7	1.7	1.8
Bromine (Cal)	11.9	11.9	13.3
Cerium (Cal)	34.7	34.3	39.3, 40.2

In Figure 6.10, the energy spectrum in the detectors for the shielding configuration with lead is shown. In the SDD spectrum, cerium and bromine fluorescence lines are visible. The bromine

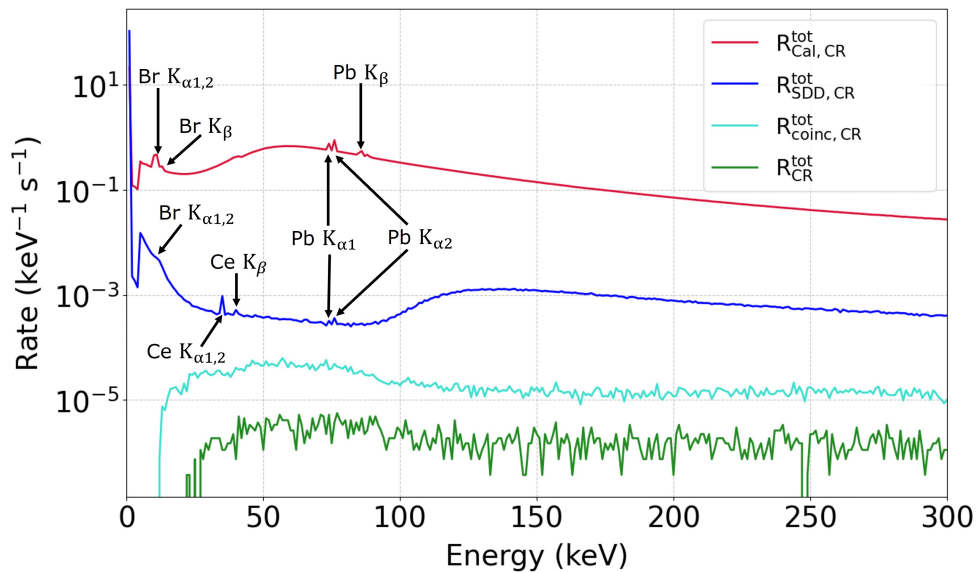


Figure 6.10.: Energy spectrum for the shielding configuration with lead in the region of interest. The total rate in the calorimeter is shown in red, while the rate in the SDD is depicted in blue. The rate of all coincident events is marked in turquoise, and the rate after event selection is drawn in green. The fluorescence lines of cerium, bromine, and lead are also indicated. The line-energies can be obtained from Table 6.5.

lines and the cerium  $K_{\beta}$  line are also recognizable in the calorimeter. In both detectors the  $K_{\alpha}$  and  $K_{\beta}$  lines from the lead shielding are visible. In Figure A.10 the spectrum is shown in a wider energy range and the 511 keV Line from the positron-electron annihilation is clearly visible. The spectra from the other investigated shielding materials are discussed in greater detail in subsection A.5.2. They are shown in Figure A.11 and Figure A.12. The fluorescence

lines of bromine and cerium are visible in all shielding configurations. Some of the shielding configurations also show a significant contribution of the shielding material's fluorescence lines in the SDD and calorimeter.

However, the final spectrum after the event selection does not show any line features in all cases. If lines were present, a further step has to be added to the event selection process, rejecting all events that have the energy of the respective fluorescence line, since it is no longer possible to trace back whether photons with this energy come from the source or are fluorescence photons. A deeper discussion on the influence of fluorescence on the telescope background is written in [subsection 6.3.1](#).

### 6.2.3. Compared results for different shielding materials

Analogue to the procedure shown in [subsection 6.1.1](#) the SNR (see [Equation 2.5](#)) and the sensitivity (MDP) (see [Equation 2.6](#)) of the telescope can be calculated. Hereby the background rates  $R_{CR}^{dir}$  for all simulated shielding materials are used. The result is given in [Figure 6.11a](#). The values for the SNR and MDP are given in [Table 6.6](#). Furthermore, the activation rate  $R_{CR}^{Act}$  is depicted in [Figure 6.11b](#) and was obtained analogue to [subsection 5.2.2](#). The activation depends on the type of material around the detector system and thus is not equal for all shielding materials. However, the rate due to activation is again negligible compared to the direct background rate from cosmic radiation for all investigated shielding materials. This is considered in the following relative to each other for the materials used. The comparison of  $R_{CR}^{dir}$  of the different configurations can be used with regard to the influence of the SAA without having to simulate the SAA again for all materials individually.

Table 6.6.: **Overview over the SNR and MDP of all investigated shielding materials.**  
The values are obtained without consideration of the influence of the SAA.

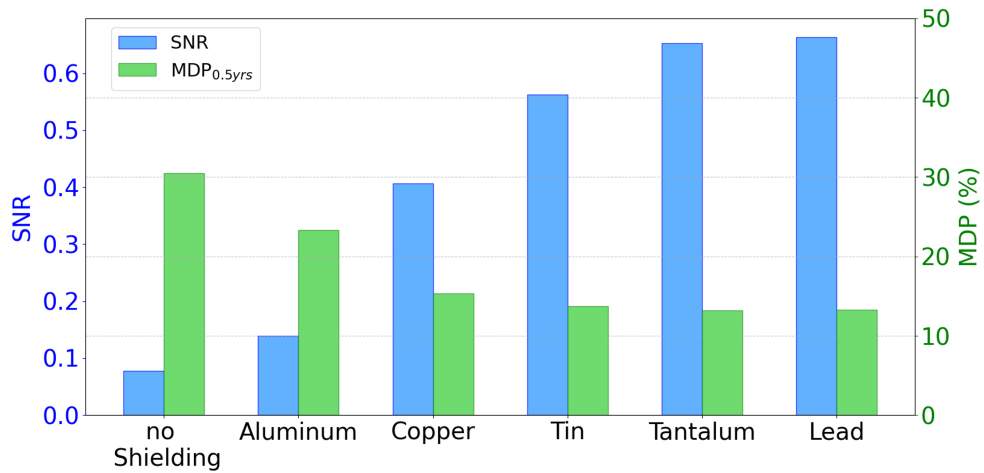
Material	SNR	MDP <sub>0.5 yrs</sub>
no Shielding	0.08	30.5 %
Aluminum	0.14	23.3 %
Copper	0.41	15.3 %
Tin	0.56	13.7 %
Tantalum	0.65	13.2 %
Lead	0.66	13.3 %

The SNR of the different materials shows a direct correlation with the attenuation properties for photons and thus the reduction of the direct background. According to [Figure 6.9](#), the attenuation property for photons for the different materials behaves as follows:

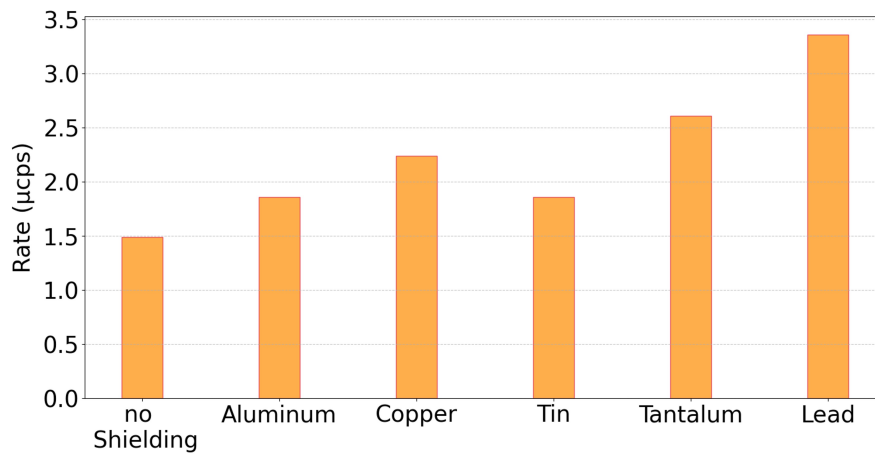
$$\begin{array}{ccccccc} \text{Aluminum} & \longrightarrow & \text{Copper} & \longrightarrow & \text{Tin} & \longrightarrow & \text{Tantalum} & \longrightarrow & \text{lead} \\ & & \text{lowest photon attenuation} & & & & \text{highest photon attenuation} & & \end{array}$$

The same behavior is reflected in the increase of the SNR. The direct background rate is highest for the aluminum shield due to poor photon attenuation. The resulting SNR is therefore the lowest. For tantalum and lead the highest SNR is obtained. In [Table 6.6](#) it is apparent that the performance of these two materials is almost equally good. Since the signal and

6. The shielding study



(a) SNR, MDP after 0.5 years for all shielding materials.



(b)  $R_{CR}^{Act}$  for all shielding materials.

Figure 6.11.: **SNR, MDP and  $R_{CR}^{Act}$  for all shielding materials.** a) shows the SNR and MDP after 0.5 years for all shielding materials. The SNR is shown in blue and indicated by the left y-axis, the MDP is depicted in green and refers to the right y-axis. The gridlines correspond to the right y-axis. b) depicts the background rate due to activation originating from the cosmic radiation  $R_{CR}^{Act}$ .

background rate are included in the calculation of the MDP, it demonstrates a similar trend. Due to the high background rate, the configuration with the aluminum shield is the least sensitive after 0.5 years of data taking ( $\text{MDP}_{0.5 \text{ yrs}} = 23.3\%$ ). Tantalum and lead again produce the best results, with tantalum being 0.1% more sensitive than lead, as can be obtained from the values in [Table 6.6](#).

With regard to the rate due to radioactive decays, the lead shielding configuration is the most active compared to the other materials. The activation rate  $R_{\text{CR}}^{\text{Act}}$  is highest here. Tantalum shows a comparatively lower value of  $R_{\text{CR}}^{\text{Act}}$ . The aluminum shielding together with the tin shielding have the lowest activation rate for a configuration with additional shielding. The activation rate for the "no Shielding" configuration is the overall lowest again. This was already explained in [subsection 6.1.1](#).

During the comparative analysis of the different configurations, the tin shield stands out in particular. The background portion due to activation is as low as for aluminum. The SNR, however, is significantly higher than for aluminum and copper. The combination of the low rate due to activation and the relatively high photon attenuation capability offers excellent conditions for effective shielding. Therefore, a further simulation with the SAA background is carried out with the tin configuration. Here, the contribution of the activation through the SAA is estimated. The results are then compared in [subsection 6.2.4](#) with the SAA simulation of the lead shield.

#### 6.2.4. Tin shielding with the SAA background included

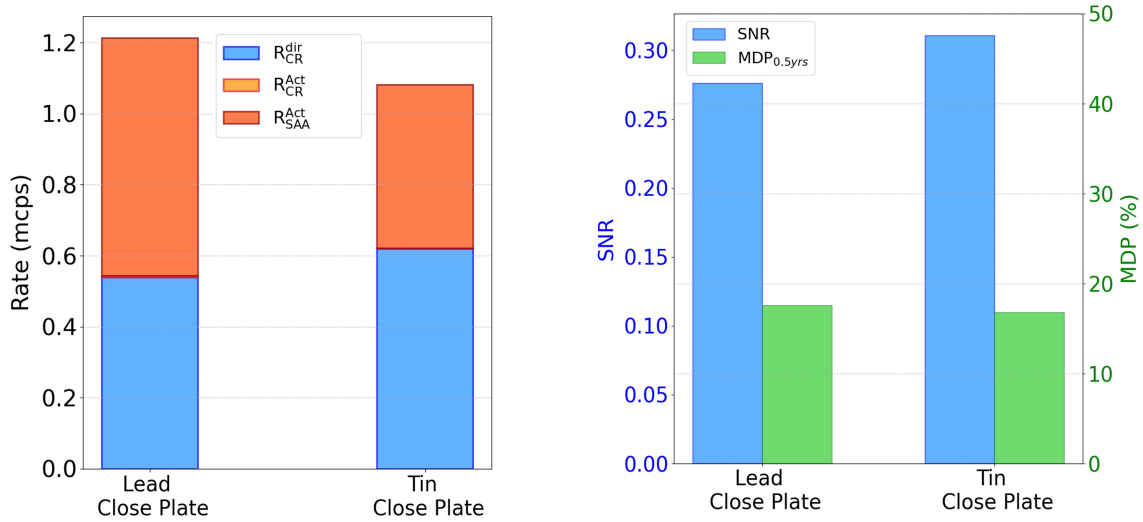
In this subsection the results of the SAA simulations with the tin shielding are compared to the ones obtained in [subsection 6.1.2](#) for the lead shielding. The activation rate  $R_{\text{SAA}}^{\text{Act}}$  is calculated following the procedure explained in [section A.4](#). The contribution of cosmic radiation and SAA to the total background rate for both settings is shown in [Figure 6.12a](#). The total background rate is lower for the tin shielding. This is due to the lower rate from SAA-induced-activation. The values for  $R_{\text{BG}}$  and  $R_{\text{SAA}}^{\text{Act}}$  are displayed in [Table 6.7](#). The contribution from the SAA is also compared there. The lower activation of tin compared to lead has a clear effect on  $R_{\text{SAA}}^{\text{Act}}$  which only contributes to 42.6% to the total background. In the lead configuration instead, the percentage is 55.6%. However the direct background  $R_{\text{CR}}^{\text{dir}}$  is increased in the tin-configuration. This is due to the lower absorption capability of tin compared to lead.

The SNR and the  $\text{MDP}_{0.5 \text{ yrs}}$  are also calculated and shown in [Figure 6.12b](#). The values are also given in [Table 6.7](#). As a result of the total background discussed above, the tin-SNR exceeds the SNR obtained from the lead configuration noticeably. The tin shielding excels also with regard to the sensitivity, with an  $\text{MDP}_{0.5 \text{ years}}$  of 16.8% compared to 17.6% for the lead shielding.

Table 6.7.: MDP, SNR, and the total background rate including its contribution of the SAA.

Material	$R_{\text{BG}}$	$\frac{R_{\text{SAA}}^{\text{Act}}}{R_{\text{BG}}}$	SNR	$\text{MDP}_{0.5 \text{ yrs}}$
Lead	1.21 mcps	55.6 %	0.28	17.6 %
Tin	1.08 mcps	42.6 %	0.31	16.8 %

## 6. The shielding study



- (a) Background contributions for the lead and tin configuration. The rates  $R_{CR}^{Act}$  are three orders of magnitude smaller than  $R_{CR}^{dir}$  and  $R_{SAA}^{Act}$  and therefore it cannot be resolved.
- (b) SNR, MDP for the lead and tin configuration. The SNR is shown in blue (left y-axis), the MDP is depicted in green (right y-axis). The gridlines correspond to the right y-axis.

Figure 6.12.: **Comparison of the total background rate, the final SNR and MDP of the tin and the lead configuration.** a) illustrates the total background rates and its contributions for both shielding configurations. b) depicts the SNR and MDP for both setups in comparison.

### 6.2.5. Summary and conclusion

The goal of this section was to find new materials, which can be used for shielding instead of lead. After comparing various shielding materials, the following results are obtained:

- The following shielding materials were chosen: Aluminum, Copper, Tin, and Tantalum  
They were selected due to their easy handling, their high photon absorption coefficient, and/or their low activation rate. Simulations with the shielding plate and collimator replaced by each of the above-mentioned materials were carried out with the cosmic radiation background source.
- The spectra in the detectors have been investigated concerning the impact of fluorescence lines of the shielding materials on the background rate. No line features are visible in the final background spectra.
- The tantalum and the lead shielding show the best sensitivity results regarding the cosmic radiation simulation.
- Comparing the rate due to activation, the tin, and aluminum shielding have the lowest contribution. The  $R_{CR}^{Act}$  is negligibly small for all configurations. Due to its low activation and relatively high SNR, the tin shielding was additionally simulated with the SAA spectrum.
- The final sensitivity can be further improved from an MDP of 17.6% down to 16.8% when a tin shielding plate and collimator are used.

Regarding the use of tin as a radiation shield in space, further investigation of the material characteristics is necessary. Being a very soft metal tin may not be suitable to be used in form of a solid plate or collimator rod. One also has to investigate the stability of tin during the accelerations and vibrations during launch. Another topic that has to be considered when working with pure tin or tin-finished surfaces are so-called "tin-whiskers". These are hair-like crystalline structures of several millimeters in length that may grow from the tin surface. Up to date, there is no single accepted explanation of the mechanisms by which these crystalline structures form, however they can grow in a vacuum and cause serious damage to the electronics assemblies. In the past, at least three complete failures of in-orbit commercial satellites due to tin whiskers have been recorded. As a result, NASA proposes to avoid using pure tin in satellite components [43].

Lead in comparison is already established as a common material used for space missions and therefore it is easy to resort to existing data concerning the use of lead in space.

### 6.3. Further shielding concepts

This section introduces two further shielding concepts which are used for satellite and Compton telescope missions. Some first considerations for the graded shielding are illustrated in [subsection 6.3.1](#), and in [subsection 6.3.2](#) the active veto is presented.

#### 6.3.1. Graded shielding

A common approach in radiation protection is the concept of *Graded Shielding*. In this setup, different materials are combined in a series of layers with varying thicknesses to build a full shielding. The atomic number  $Z$  decreases from the outside to the inside of the shielding layers. Hence, the concept is also referred to as *Graded  $Z$  – Shielding*. Any X-ray fluorescence from outer-lying materials is effectively suppressed by inner-lying materials and/or the energy of the fluorescence peaks is moved outside of the energy window of main interest in the mission [44].

Instead of relying only on lead as shielding material, the combination of various heavier and lighter materials (high  $Z$  and low  $Z$ ) can also reduce the overall shielding mass. Previous X-ray telescopes such as XMM Newton, Suzaku, and Chandra have already used this technique [45] [46]. As shown in [subsection 6.2.2](#) there is no evidence of fluorescence lines in the final spectrum of the ComPol CubeSat. However, the fluorescence photons do not have to contribute only as a visible line feature. They can undergo scattering processes like Compton scattering in the surrounding material and lose a fraction of their energy before interacting with the detectors.

This causes a broad background from fluorescence and it should be investigated further by - on the one hand - adjusting the simulation output and looking deeper into the interactions, that fluorescence photons undergo in the detector system. On the other hand, new simulations with various graded shielding configurations can be conducted. During the data analysis, the final spectra are compared to each other and to the results shown in [subsection 6.2.2](#).

In order to estimate possible options for a graded shielding suitable for this mission, several principal points have to be considered and optimized. First of all, the overall shielding efficiency should be comparable to or superior to the results that are obtained with lead (as shown in the course of this thesis). Secondly, the individual materials have to be chosen in a way, that they are able to absorb the fluorescence lines of the outer-lying material most efficiently. The thicknesses have to be calculated with respect to the attenuation capabilities of the individual materials and the size and mass constraints of the CubeSat. And as the last

## 6. The shielding study

point, it should be feasible to combine the materials to get the layered structure.

A common setup for a graded shielding is the combination of lead, tantalum tin and/or copper in the form of thin layers, or metal foils stitched together. Examples of the combination of these materials to form a graded shielding are the BAT instrument on the Swift satellite [47] and the Wide Field Imager of the ATHENA X-Ray Observatory [45].

Taking these sources as an example, some first calculations for a possible graded shielding are performed. Due to its high photon attenuation, lead is chosen to build the outer layer of the graded shielding. In order to save mass, the lead layer has to be thinner than 2 mm. For the first approach, only two layers are considered. Copper is chosen to build the second layer because its fluorescence lines lie beneath the energy threshold of the calorimeter and thus outside the energy range of interest. The requirement for the copper layer is to shield the fluorescence lines originating from the lead as efficiently as possible. The fluorescence energies are taken from Table 6.5 and for lead they are at 75.0 keV, 72.8 keV and 84.9 keV ( $K_{\alpha 1}$ ,  $K_{\alpha 2}$  and  $K_{\beta}$ ). With the help of Figure 6.13a the thickness of the copper layer that effectively shields these X-ray energies can be determined. A 3 mm thick layer of copper shielding 70% of 80 keV photons is chosen. This inner layer is combined with 1 mm lead on the outer side. A sketch of this configuration is shown in Figure 6.14a. The resulting attenuation vs. the initial photon energies is shown in Figure 6.15a. The attenuation capability of a 2 mm lead shield is also indicated in this figure (dashed line). At energies, lower than 300 keV the standard 2 mm lead shielding performs slightly better. At higher energies, the shielding capacity of the newly designed graded shielding exceeds the standard version. The overall mass of this lead-copper configuration is 244 g compared to 144 g for the standard lead shield. Concerning the mass limitations in the satellite, this graded shielding is still feasible, however more calculations with different thicknesses have to be carried out in order to reach roughly the same overall mass as the 2 mm lead shield.

In a second step, some first calculations with a three-layered graded shielding are conducted.

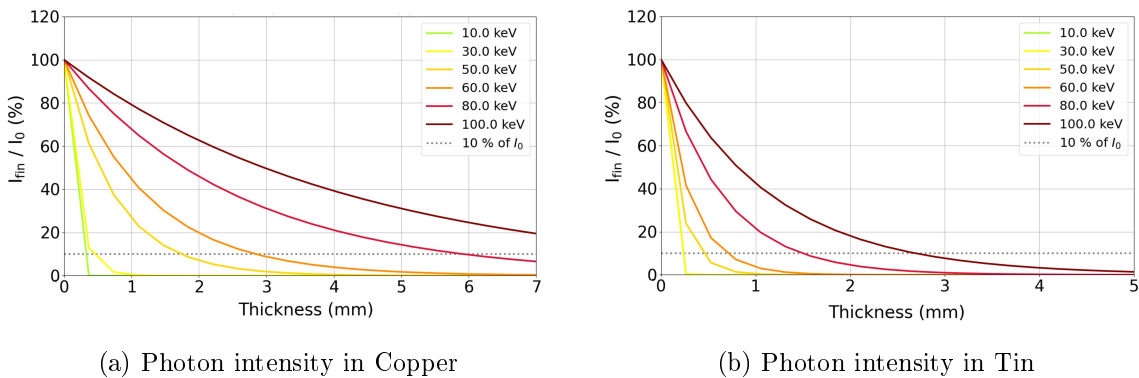
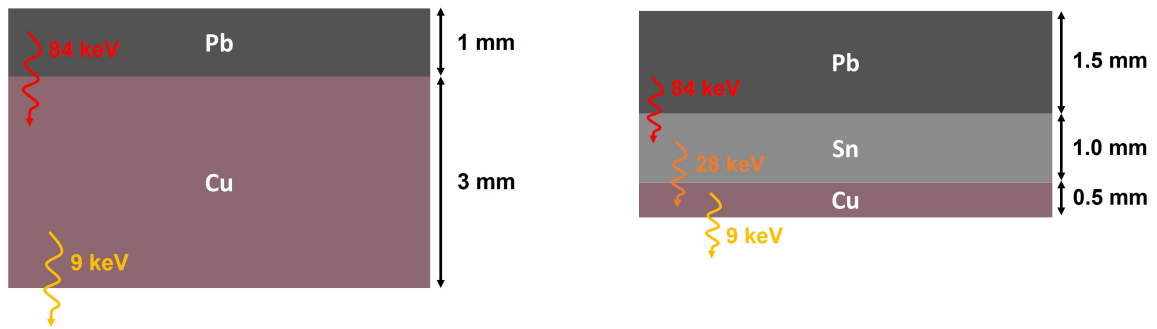


Figure 6.13.: **Dependence of the attenuation of photons on the thickness.** a) shows the photon intensity for copper. b) illustrates the intensity for tin.

In this case, tin is chosen to build the second layer between an outer lead plate of 1.5 mm thickness and an inner copper layer with a thickness of 0.5 mm. Since tin is sandwiched between lead and copper, there is no fear of tin whiskers being created. Using the attenuation dependence on the thickness of tin, displayed in Figure 6.13b, the thickness of the tin layer is determined to be 1 mm. This shields 80% of 80 keV photons and therefore has - compared to copper - an improved shielding capability with regard to the lead fluorescence. In this configuration, the task for the copper layer is to shield the tin fluorescence lines at 25 keV

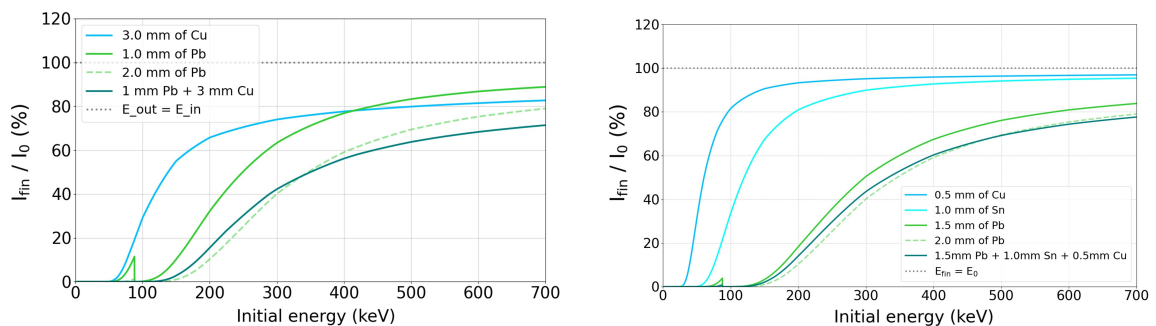
and 28 keV (taken from Table 6.5). The thickness is set to 0.5 mm this time. A sketch of this configuration is drawn in Figure 6.14a. The resulting attenuation vs. the initial photon energies is illustrated in Figure 6.15b. Over the considered energy range, the performance of the lead-tin-copper configuration is approximately equal to the standard 2 mm lead shielding. The mass is 287 g and therefore nearly twice as heavy as the standard shielding. Exploring different thicknesses and/or material combinations can lead to a mass reduction and/or a further improvement of the photon attenuation capability. This task has to be investigated in the future.



(a) Schematic drawing of the lead-copper graded shielding.

(b) Schematic drawing of the lead-tin-copper graded shielding.

Figure 6.14.: **Schematic drawings of two possible ideas for graded shieldings.** The maximum fluorescence energies of each material are depicted as well. **a)** illustrates the lead-copper graded shielding. **b)** sketches the lead-tin-copper graded shielding.



(a) Final intensity vs. initial energy for lead and copper individually and combined.

(b) Final intensity vs. initial energy for lead, tin and copper individually and combined.

Figure 6.15.: **Final intensity vs. initial energy for all simulated graded shielding materials individually as well as for the combination of the respective materials (plotted in teal).** **a)** considers the lead-copper configuration. **b)** illustrates the lead-tin-copper shielding. The thickness of each layer is given in the legend. The dotted line shows the Attenuation dependence for the 2 mm lead shielding as comparison.

### 6.3.2. Active veto

Instead of using passive shielding, an active veto can be installed in the CubeSat. The advantage of an active shielding or active veto is to directly monitor background particles in the shielding volume. Usually, a plastic scintillator or other types of scintillating material are used for an active veto. If a charged particle interacts in the active shielding and in the detector(s) it can be excluded in an additional step during event selection (veto). In particular, this is true for decay products, namely electrons, positrons, and alphas, generated in the active shielding material itself. Consequently, an active veto could probably reduce the background rate due to activation significantly. In order to conduct a quantitative analysis more simulations using an active veto need to be carried out in the future.

Furthermore, the material used for the veto needs to be selected carefully. The results obtained in [subsection 6.2.1](#) point out, that photons contribute as a major background source to the direct cosmic radiation background rate. Hence, the active veto has to have a decent photon attenuation capability in order to reduce this background rate to a level comparable with passive shielding. A normal plastic scintillator will probably not be sufficient. The photon attenuation for  $\text{CeBr}_3$ , however, lies within the range of materials used in [subsection 6.2.2](#). The attenuation of  $\text{CeBr}_3$  versus different initial energies is illustrated in [Figure 6.16](#). A simulation with a shielding plate made of 4.5 mm  $\text{CeBr}_3$  which is read out as an active veto detector, would yield interesting results concerning the direct and indirect background rates. On the other hand,  $\text{CeBr}_3$  is technically quite complex to fabricate. Since it is a crystal, it is not very mechanically stable, and not easy to shape into arbitrary forms. Moreover, it has to be packaged airtight, as  $\text{CeBr}_3$  is hygroscopic.

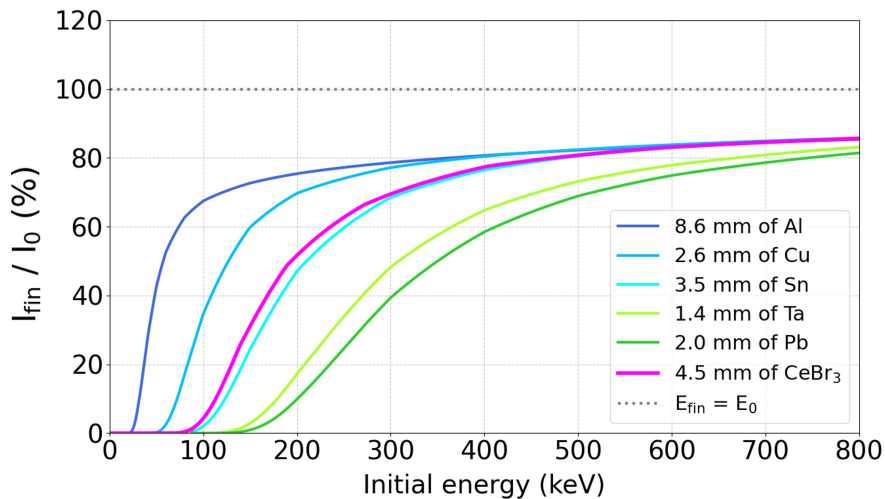


Figure 6.16.: **Final intensity vs. initial energy for all simulated shielding plate-materials and  $\text{CeBr}_3$ .** The thickness of the shielding plate for each material is given in the legend.

## 7. Summary

This thesis aims to investigate all possible background contributions to the ComPol CubeSat and, using the results obtained from the background study, to improve the shielding concept of the satellite. The Compton telescope will be launched into Low Earth Orbit and its goal is the observation of X-rays originating from the black hole binary Cygnus X-1 to gain more scientific insights into the physical processes and geometry of this compact astrophysical object.

During its stay in orbit, the CubeSat will be exposed to background particles from cosmic radiation and the South Atlantic Anomaly. The background sources are presented and discussed in the first part of the thesis.

The cosmic radiation background depends mainly on the height of the satellite above the earth's surface. A typical altitude for CubeSats is approximately 500 km above sea level. The cosmic radiation consists of mainly photons, electrons, positrons, protons, neutrons, and alpha particles originating from galactical and extragalactic sources or being generated in the upper atmosphere. Their flux and energy distribution can be assumed to stay constant with regard to the position of the satellite and the duration of the mission.

The South Atlantic Anomaly (SAA), on the other hand, is a region of increased flux of charged particles confined to an area above the South Atlantic. The exact shape and flux distribution in the SAA are influenced by the chosen altitude of the satellite. In order to estimate the maximum background due to the SAA, an orbit is selected, which resembles a worst-case scenario covering a flight through the entire SAA.

Both background sources contribute to the overall telescope's background via direct interactions in the detector system and a time-delayed contribution due to cosmogenic activation. The cosmogenic activation is defined as the formation of all types of unstable nuclei within the CubeSat's material caused by cosmic particles. Spallation, fission, and capture processes with highly energetic cosmic hadrons are the most common source for the generation of excited or radioactive nuclei. These isotopes radioactively decay within their specific lifetime and the resulting decay products can cause an additional background in the detectors. The activation in the telescope's components will accumulate over time due to its exposure to cosmic radiation and SAA-protons.

The goal of the first part of this thesis is to estimate the contribution of each background source regarding its direct and activation-induced background rates. The studies in this thesis are performed via Geant4. The ComPol geometry, as well as the particle spectra of the relevant background sources and from Cygnus X-1 are implemented in this Monte Carlo simulation toolkit. After analyzing the simulation data of both background sources, the total background rate is obtained:

$$\begin{aligned}
 R_{\text{BG}} &= R_{\text{CR}}^{\text{dir}} + R_{\text{CR}}^{\text{Act}} + R_{\text{SAA}}^{\text{Act}} \\
 1.49 \text{ mcps} &= 0.88 \text{ mcps} + 2.61 \text{ } \mu\text{cps} + 0.61 \text{ mcps}
 \end{aligned}$$

The direct background from the cosmic radiation and the background due to activation from

## 7. Summary

the SAA are found to contribute to a significant extent to the overall background rate. It should be noted, that the contribution of the SAA makes up 40.9% of the total background rate, and therefore the satellite's orbit need to be selected carefully in order to minimize the time spend in this area. The activation due to the cosmic radiation does not play a major role in the telescope's background.

Additionally, a more detailed analysis of the created unstable isotopes in the CubeSat structure is performed. The strongest activated parts in the satellite are the lead shielding, the CeBr<sub>3</sub> detector, and the reaction wheels whereas the most activating particles are protons and neutrons.

In the second part of this thesis, the shielding geometry and material are varied in order to improve the Compton telescope's sensitivity. The main task of improving the shielding strategy is to find an optimal balance between reducing the activation-induced background and suppressing the direct flux of particles reaching the detector system. It is often the case that reducing one component of the background results in an increase in the competing component. Generally speaking, an increase in the material around the detectors will lead to a decrease in the direct background rate, while the number of radioactive particles and thus the rate due to activation will increase.

Simulations with all background sources are carried out in order to find the optimal shielding geometry, with which the total background rate is minimum. It is found that the geometry can indeed be improved, so as to reduce the total background rate by 18.8%. The sensitivity on the degree of polarization of a Compton telescope is usually calculated with the Minimum Detectable Polarization (MDP). The MDP after 0.5 years of observation time of Cygnus X-1 is also reduced and is determined to be 17.6% compared to 19.1% for the not-optimized geometry.

In the next step, simulations with different shielding materials are performed. The used materials are aluminum, copper, tin, lead, and tantalum. The materials are chosen based on their photon attenuation capability, their mechanical handling, and their activation rate. With regard to the shielding efficiency against cosmic radiation, the tantalum and lead shielding perform best. In the configurations using the tin, or the aluminum shielding the lowest contribution due to activation is noticed. However, the background rate due to activation is negligibly small for all configurations. The tin shielding is additionally simulated with the SAA background and in comparison to the simulation with a lead shielding, the telescope's sensitivity is improved by 0.8%, resulting in an MDP of 16.8%.

Finally, the concept of graded shielding and active veto shielding are introduced as further shielding ideas and some first considerations are proposed.

In the future, the idea of the active veto and the concept of graded shielding have to be investigated in more detail. Furthermore, the background rate due to activation generated by the SAA needs to be examined more closely and the features seen in the energy spectrum have to be defined.

# A. Appendix

## A.1. Rate overview

Table A.1.: **Overview over all rates, which are investigated throughout the thesis.**

The superscript always indicates whether the respective variable is a rate consisting only of radioactive decays ("Act") or a total rate in which all hits are taken into account ("tot"). The superscript "dir" is used to designate all rates that include all processes except Activation. Here, the final rates after the event-selection process has been applied are considered. The subscript indicates the background source from which the rate was calculated (i.e. "Cosmic Radiation", or "SAA"). It is also indicated in which detector the rate is obtained ("SDD", or "Cal" for calorimeter). The rate of coincident hits is indicated by the subscript "coinc".

Variable	Description
$R_{BG}$	total background rate
$R_{CR}^{dir}$	direct Cosmic Radiation background rate (after event selection)
$R_{CR}^{Act}$	Cosmic Radiation background rate due to Activation (after event selection)
$R_{CR}^{tot}$	total background rate from Cosmic Radiation (after event selection) $\rightarrow R_{CR}^{dir} + R_{CR}^{Act}$
$R_{SAA}^{Act}$	SAA background rate due to Activation (after event selection)
$R_{SDD, CR}^{tot}$	total background rate in the SDD from Cosmic Radiation (before event selection)
$R_{Cal, CR}^{tot}$	total background rate in the calorimeter from Cosmic Radiation (before event selection)
$R_{SDD, CR}^{Act}$	background rate in the SDD from Cosmic Radiation due to Activation (before event selection)
$R_{Cal, CR}^{Act}$	total background rate in the calorimeter from Cosmic Radiation due to Activation (before event selection)
$R_{coinc, CR}^{tot}$	total background rate from Cosmic Radiation (coincident hits)

**Table A.1 continued from previous page**

$R_{\text{coinc, CR}}^{\text{Act}}$	background rate from Cosmic Radiation due to Activation (coincident hits)
$R_{\text{SDD, SAA}}^{\text{tot}}$	total background rate in the SDD from the SAA (before event selection)
$R_{\text{Cal, SAA}}^{\text{tot}}$	total background rate in the calorimeter from the SAA (before event selection)
$R_{\text{SDD, SAA}}^{\text{Act}}$	background rate in the SDD from the SAA due to Activation (before event selection)
$R_{\text{Cal, SAA}}^{\text{Act}}$	total background rate in the calorimeter from the SAA due to Activation (before event selection)
$R_{\text{coinc, SAA}}^{\text{tot}}$	total background rate from the SAA (coincident hits)
$R_{\text{coinc, SAA}}^{\text{Act}}$	total background rate from the SAA due to Activation (coincident hits)
Activation Rate <sub>tot</sub>	total rate of activated nuclei in the CubeSat
$R_{\text{S}}$	Signal rate (rate from Cygnus X-1 after event selection)

## A.2. Code for the Activation simulation

The following pages show code sections of the Activation simulation. The unstable nuclei are selected in `TrackingAction.cc`. The assignment of the `SubEventID` is done in `StackingAction.cc`.

## Code section of TrackingAction.cc

```

1  #include <G4SystemOfUnits.hh>
2  #include "TrackingAction.hh"
3  #include "RunAction.hh"
4  #include "G4RunManager.hh"
5  #include "EventAction.hh"
6  #include "G4IonTable.hh"
7  #include "G4ParticleTypes.hh"
8  #include "G4Track.hh"
9  #include "G4TrackStatus.hh"
10 #include <G4StackManager.hh>
11 #include "G4TrackingManager.hh"
12
13 #include "g4root.hh"
14 #include <MyTrackInformation.hh>
15 #include "G4VUserTrackInformation.hh"
16 #include <G4VProcess.hh>
17 #include "G4Material.hh"
18 #include "G4LogicalVolume.hh"
19 #include "G4VPhysicalVolume.hh"
20 #include "G4MaterialTable.hh"
21 #include <G4PhysicalVolumeStore.hh>
22
23 TrackingAction::TrackingAction(EventAction* event)
24 :G4UserTrackingAction(), fEventAction(event)
25 {
26     fSubEventID = fSEIDdefault;
27     fSubEventParentID = fSEPIDdefault;
28 }
29 TrackingAction::~TrackingAction()
30 {}
31
32 void TrackingAction::PreUserTrackingAction(const
    • G4Track* aTrack)
33 {
34     //first Track of Event -> set private SubEventID back
    • to 1 and SubEventParentID back to 0!
35     G4int TrackID = aTrack->GetTrackID();
36     if (TrackID == 1)
37     {

```

```

38     fSubEventID = fSEIDdefault;
39     fSubEventParentID = fSEPIDdefault;
40 }
41
42 // get the G4UserTrackInformation of the current Track
43 MyTrackInformation* MyTrInf = (MyTrackInformation*)
  • aTrack->GetUserInformation();
44 // is the Track an unstable nuclei and what is its
  • SubEventID?
45 G4bool Radioactive = MyTrInf->GetRadioactive();
46 G4int SubEventID = MyTrInf->GetSubEventID();
47 G4int SubEventParentID = MyTrInf-
  • >GetSubEventParentID();
48 G4RunManager* runmanager =
  • G4RunManager::GetRunManager();
49 G4int EventID = runmanager->GetCurrentEvent()-
  • >GetEventID();
50 // for all unstable nuclei
51 if (Radioactive == true)
52 {
53     //set the SubEventID and SubEventParentID to the
  • SubEventID and SubEventParentID of the radioactive
  • Track
54     fSubEventID = SubEventID;
55     fSubEventParentID = SubEventParentID;
56     // Get all important Track Information here
57     G4int ParentID = aTrack->GetParentID();
58     G4Ions* ion = (G4Ions*) aTrack->GetDefinition();
59     G4int ionID = aTrack->GetDefinition()-
  • >GetPDGEncoding();
60     G4double lifetime = ion->GetPDGLifeTime();
61     G4int ParticleID = runmanager->GetCurrentEvent()-
  • >GetPrimaryVertex()->GetPrimary()->GetPDGcode();
62     G4VProcess* process = (G4VProcess*) aTrack-
  • >GetCreatorProcess();
63     G4int CreationProcess = process->GetProcessSubType();
64     G4double xpos = aTrack->GetPosition()[0];
65     G4double ypos = aTrack->GetPosition()[1];
66     G4double zpos = aTrack->GetPosition()[2];

```

```

66     G4double zpos = aTrack->GetPosition()[2],
67     G4double creation_time = aTrack->GetGlobalTime();
68     G4VPhysicalVolume* material = (G4VPhysicalVolume*)
    • aTrack->GetVolume();
69     // ----- print list of all physical
    • volumes -----
70     G4PhysicalVolumeStore* store =
    • G4PhysicalVolumeStore::GetInstance();
71     if (store==0)
72     {
73         G4cout << "G4PhysicalVolumeStore not
    • accessible"<< G4endl;
74     }
75     else
76     {
77         unsigned int length = store->size();
78         G4int i = 0;
79         fVolNumber = 0;
80         for (unsigned int iVol = 0; iVol < length;
    • iVol++)
81         {
82             if ((*store)[iVol] == material)
83             {
84                 fVolNumber += i;
85             }
86             i++;
87         }
88     }
89     // Save all important Track Information to the
    • Activation tuple in the output file
90     G4AnalysisManager* analysis =
    • G4AnalysisManager::Instance();
91     G4int NTupleID = 4;
92     analysis->FillNTupleIColumn(NTupleID, 0, EventID); /
    • / = EventID
93     analysis->FillNTupleIColumn(NTupleID, 1, SubEventID);
94     analysis->FillNTupleIColumn(NTupleID, 2,
    • SubEventParentID);
95     analysis->FillNTupleIColumn(NTupleID, 3, fVolNumber);

```

```

96     analysis->FillNtupleFColumn(NTupleID, 4, xpos);
97     analysis->FillNtupleFColumn(NTupleID, 5, ypos);
98     analysis->FillNtupleFColumn(NTupleID, 6, zpos);
99     analysis->FillNtupleFColumn(NTupleID, 7,
    •     creation_time);
100    analysis->FillNtupleIColumn(NTupleID, 8, TrackID);
101    analysis->FillNtupleIColumn(NTupleID, 9, ParentID);
102    analysis->FillNtupleIColumn(NTupleID, 10,
    •     ParticleID);
103    analysis->FillNtupleIColumn(NTupleID, 11, ionID);
104    analysis->FillNtupleFColumn(NTupleID, 12, lifetime);
105    analysis->FillNtupleIColumn(NTupleID, 13,
    •     CreationProcess);
106    analysis->AddNtupleRow(NTupleID);
107    }
108    // Assign the correct SubEventID and SubEventParentID
    •     to all Tracks
109    // This was done already in
    •     StackingAction::ClassifyNewTrack() for radioactive
    •     Tracks
110    // But not yet for normal Tracks!
111    MyTrInf->SetSubEventID(fSubEventID);
112    MyTrInf->SetSubEventParentID(fSubEventParentID);
113    if (fSubEventID > 1)
114    {
115        // save all decays! Products from ProcessType
    •     "decay" = 6
116        // relevant subprocesses are "decay"? = 201,
    •     "DecayRadio" = 210, "DecayExt" = 231
117        G4VProcess* process = (G4VProcess*) aTrack-
    •     >GetCreatorProcess();
118        G4int CreationProcess = process->GetProcessSubType();
119        if (CreationProcess==201 || (CreationProcess==210
    •     || (CreationProcess==231) || (CreationProcess==211))
120        {
121            // Get all relevant Information (as above)
122            G4int ParentID = aTrack->GetParentID();
123            G4int ParticleID = aTrack->GetDefinition()-
    •     >GetPDGEncoding();

```

```

124     G4int PrimaryID = runmanager->GetCurrentEvent()-
    • >GetPrimaryVertex()->GetPrimary()->GetPDGcode();
125     G4double xpos = aTrack->GetPosition()[0];
126     G4double ypos = aTrack->GetPosition()[1];
127     G4double zpos = aTrack->GetPosition()[2];
128     G4double Ekin = aTrack->GetKineticEnergy();
129     G4double Etot = aTrack->GetTotalEnergy();
130     G4double creation_time = aTrack->GetGlobalTime();
131     G4VPhysicalVolume* material = (G4VPhysicalVolume*)
    • aTrack->GetVolume();
132     // ----- print list of all physical
    • volumes -----
133     G4PhysicalVolumeStore* store =
    • G4PhysicalVolumeStore::GetInstance();
134     if (store==0)
135     {
136         G4cout << "G4PhysicalVolumeStore not
    • accessible"<< G4endl;
137     }
138     else
139     {
140         unsigned int length = store->size();
141         G4int i = 0;
142         fVolNumber = 0;
143         for (unsigned int iVol = 0; iVol < length;
    • iVol++)
144         {
145             if ((*store)[iVol]) == material)
146             {
147                 fVolNumber += i;
148             }
149             i++;
150         }
151     }
152     // Save all important Track Information to the
    • Activation tuple in the output file
153     G4AnalysisManager* analysis =
    • G4AnalysisManager::Instance();
154     G4int NTupleID = 5:

```

## A. Appendix

```
155     analysis->FillNtupleIColumn(NTupleID, 0, EventID);
    •     // = EventID
156     analysis->FillNtupleIColumn(NTupleID, 1,
    •     fSubEventID);
157     analysis->FillNtupleIColumn(NTupleID, 2,
    •     fSubEventParentID);
158     analysis->FillNtupleIColumn(NTupleID, 3,
    •     fVolNumber);
159     analysis->FillNtupleFColumn(NTupleID, 4, xpos);
160     analysis->FillNtupleFColumn(NTupleID, 5, ypos);
161     analysis->FillNtupleFColumn(NTupleID, 6, zpos);
162     analysis->FillNtupleFColumn(NTupleID, 7,
    •     creation_time);
163     analysis->FillNtupleIColumn(NTupleID, 8, TrackID);
164     analysis->FillNtupleIColumn(NTupleID, 9, ParentID);
165     analysis->FillNtupleIColumn(NTupleID, 10,
    •     PrimaryID);
166     analysis->FillNtupleIColumn(NTupleID, 11,
    •     ParticleID);
167     analysis->FillNtupleIColumn(NTupleID, 12,
    •     CreationProcess);
168     analysis->FillNtupleFColumn(NTupleID, 13, Ekin);
169     analysis->FillNtupleFColumn(NTupleID, 14, Etot);
170     analysis->AddNtupleRow(NTupleID);
171     }
172 }
173 }
174 void TrackingAction::PostUserTrackingAction(const
    • G4Track*)
175 {
176 }
177
```

## Code section of StackingAction.cc

```

1  #include <G4SystemOfUnits.hh>
2  #include "StackingAction.hh"
3  #include "RunAction.hh"
4  #include "G4RunManager.hh"
5  #include "EventAction.hh"
6  #include "TrackingAction.hh"
7  #include "G4ParticleTypes.hh"
8  #include "G4IonTable.hh"
9  #include <G4Track.hh>
10
11 #include <G4Gamma.hh>
12 #include <G4Electron.hh>
13
14 #include "g4root.hh"
15 #include <MyTrackInformation.hh>
16 #include "G4VUserTrackInformation.hh"
17 #include "G4TrackingManager.hh"
18 #include <G4VProcess.hh>
19 #include "G4Material.hh"
20 #include "G4LogicalVolume.hh"
21 #include "G4VPhysicalVolume.hh"
22 #include "G4MaterialTable.hh"
23 #include <G4PhysicalVolumeStore.hh>
24
25 StackingAction::StackingAction(TrackingAction* track) :
26     G4UserStackingAction(), fTrackingAction(track)
27 {
28     fSubEventID = fTrackingAction->GetSEIDdefault();
29     fRadioactive = false;
30 }
31 G4ClassificationOfNewTrack
32 • StackingAction::ClassifyNewTrack (const G4Track* aTrack)
33 {
34     ///////////////////////////////////////////////////////////////////
35     • ///////////////////////////////////////////////////////////////////
36     // Select all unstable nuclei and shift them to the
37     • waiting stack. //
38     // Each unstable nuclei is simulated separately as a
39     • SubEvent. //

```

## A. Appendix

```
36 // Each SuEvent has its own
    • SubEventID. //
37 ///////////////////////////////////////////////////////////////////
    • ///////////////////////////////////////////////////////////////////
38 // get particle type
39 G4String particleType = aTrack->GetDefinition()-
    • >GetParticleType();
40 G4int ParentID = aTrack->GetParentID();
41 // check for secondaries (ParentID > 1) and
    • particleType == "nucleus"
42 // then: check for Lifetime > 0
43 if (particleType == "nucleus" && (ParentID>0))
44 {
45     G4Ions* ion = (G4Ions*) aTrack->GetDefinition();
46     G4String ionName = ion->GetParticleName();
47     G4double lifetime = ion->GetPDGLifeTime();
48     if (lifetime > 0)
49     {
50         // set fRadioactive on true / false
51         fRadioactive = true;
52         fSubEventID += 1;
53     }
54     else
55     {
56         fRadioactive = false;
57     }
58 }
59 else
60 {
61     fRadioactive = false;
62 }
63 // create G4VUserTrackInformation if it does not yet
    • exist
64 if(!aTrack->GetUserInformation())
65 {
66     G4VUserTrackInformation* MyTrInf = new
    • MyTrackInformation;
67     aTrack->SetUserInformation (MyTrInf);
68 }
    •
```

```

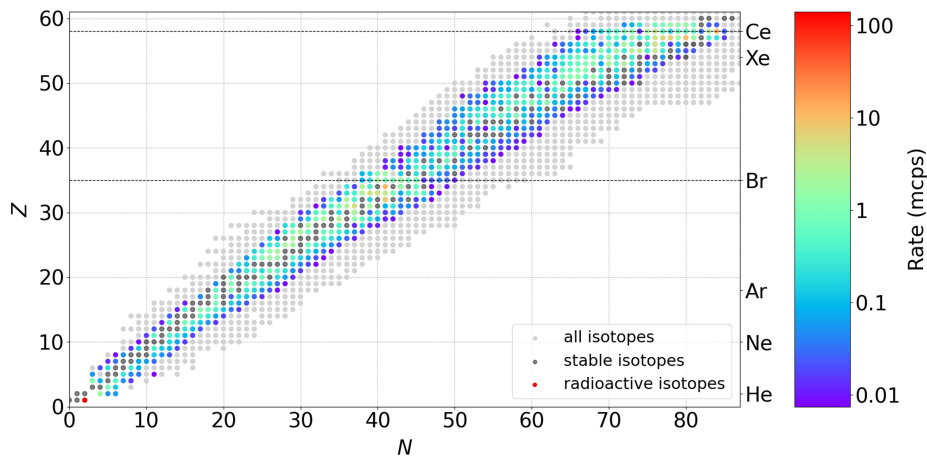
69     MyTrackInformation* MyTrInf = (MyTrackInformation*)
    • aTrack->GetUserInformation();
70     // save fRadioactive status in G4VUserTrackInformation
71     MyTrInf->SetRadioactive(fRadioactive);
72     if (fRadioactive == true)
73     {
74         // Save SubEventID in G4VUserTrackInformation ONLY
    • for Tracks of unstable nuclei
75         MyTrInf->SetSubEventID(fSubEventID);
76         // The fSubEventID for normal Tracks are irrelevant
    • here their value remains zero.
77         // See TrackingAction::PreUserTrackingAction() for
    • the final assignment of the SubEventID.
78         // Save current SubEventID from TrackingAction as
    • SubEventParentID for unstable nuclei since they
    • belong to the next SubEvent
79         G4int currentSubEventID = fTrackingAction-
    • >GetSubEventID();
80         MyTrInf->SetSubEventParentID(currentSubEventID);
81
82         // push Track of unstable nuclei to the waiting stack
83         return fWaiting;
84     }
85     // for Tracks of stable nuclei or other particles:
86     // push Track to default stack (urgent stack)
87     else
88     {
89         return
    • G4UserStackingAction::ClassifyNewTrack(aTrack);
90     }
91 }
92
93 void StackingAction::NewStage()
94 {
95     // This function is called when the urgent stack was
    • empty
96     // The urgent stack is already refilled with all
    • Tracks from the waiting stack

```

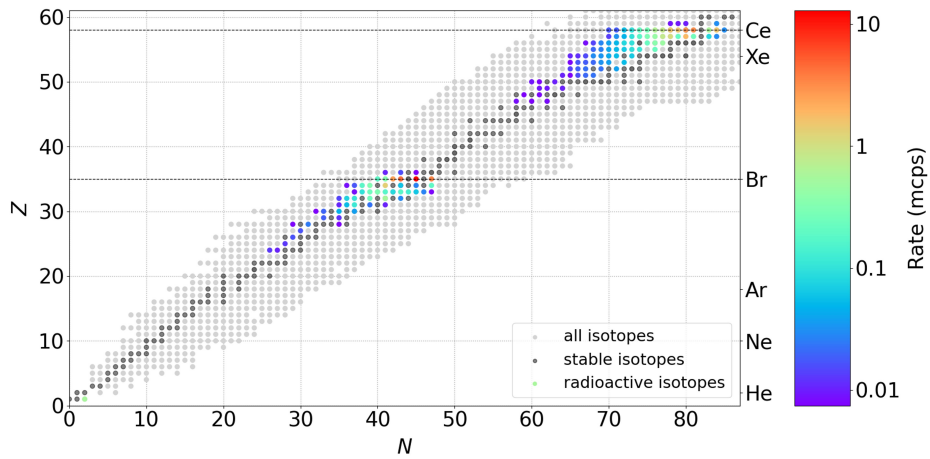
## A. Appendix

```
97     G4int NUrgent = stackManager->GetNUrgentTrack();
98     G4int NWaiting = stackManager->GetNWaitingTrack();
99
100    // If more than one Track got transfered from the
    •   waiting to the urgent stack:
101    if (NUrgent>1)
102    {
103        // move all Tracks back to the waiting stack
104        stackManager->TransferStackedTracks(fUrgent,
    •   fWaiting);
105        // move only one Track back again to the urgent stack
106        stackManager->TransferOneStackedTrack(fWaiting,
    •   fUrgent);
107    }
108    // reset fSubEventID if all stacks are empty
109    else if ((NUrgent==0) && (NWaiting==0))
110    {
111        fSubEventID = fTrackingAction->GetSEIDdefault();
112    }
113 }
114
```

### A.3. Additional isotope charts from the activation study



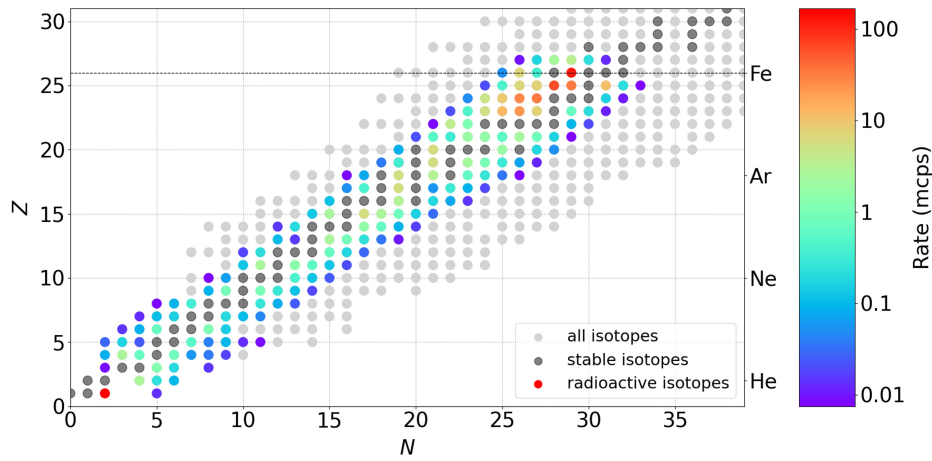
(a) Radioactive isotopes in the calorimeter created by protons.



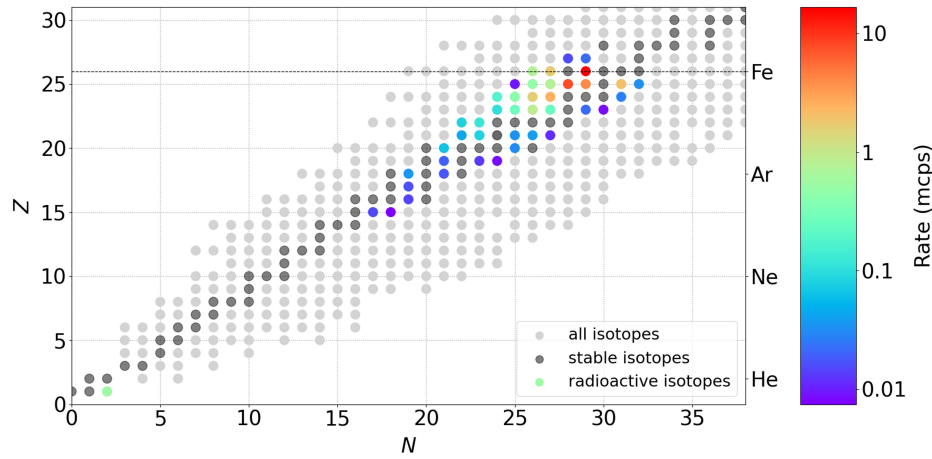
(b) Radioactive isotopes in the calorimeter created by neutrons.

Figure A.1.: **Isotope charts showing all radioactive isotopes in the calorimeter created by protons or neutrons.** The colors indicate the abundance of each isotope (given in their creation rate). The stable isotopes are marked in dark grey, and for better orientation, all known isotopes are drawn in the background with a light grey color. **a)** shows the radioactive isotopes created by protons. In **b)** the radioactive isotopes created by neutrons are shown.

## A. Appendix



(a) Radioactive isotopes in the reaction wheels (iron) created by protons.



(b) Radioactive isotopes in the reaction wheels (iron) created by neutrons.

Figure A.2.: **Isotope charts showing all radioactive isotopes in the reaction wheels (iron) created by protons or neutrons.** The colors indicate the abundance of each isotope (given in their creation rate). The stable isotopes are marked in dark grey, and for better orientation, all known isotopes are drawn in the background with a light grey color. **a)** depicts the radioactive isotopes created by protons. **b)** illustrates all radioactive isotopes created by neutrons.

### A.4. The SAA temporal evolution

In the temporal evolution of the activation rate in the detector system is shown (see [Figure 5.8](#)). This figure is generated by making use of the numerical convolution. The exact procedure is explained in the following paragraph.

During the simulation, all hits in the detectors are assigned a timestamp when the interaction in the detectors takes place. The time is always counted relative to the event-start, meaning the generation of the initial source particle at the source surface. The majority of hits in the detector system are registered nearly instantaneously after event-start. Consequently, the saved time is virtually 0. However, particles generated by radioactive decays reach the detector delayed, depending on the lifetime of the mother nuclide (in the case of decay chains

all lifetimes of all previous decays have to be taken into account). The time distribution of all hits in the detectors originating from radioactive decays is shown in Figure A.3. Figure A.3

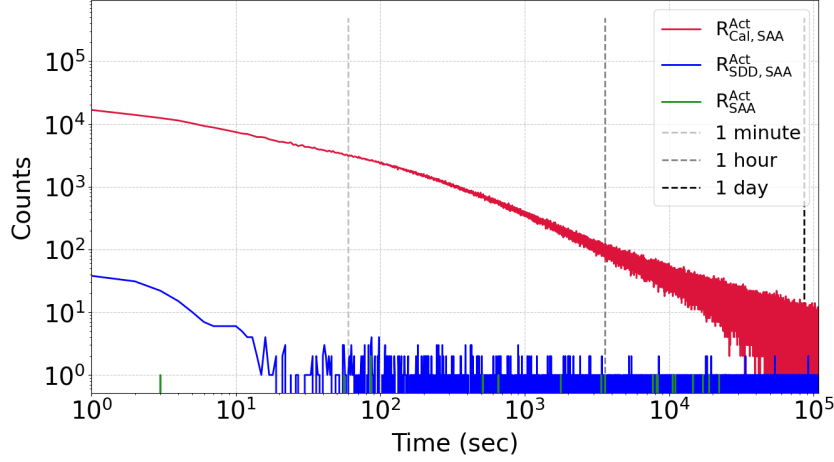
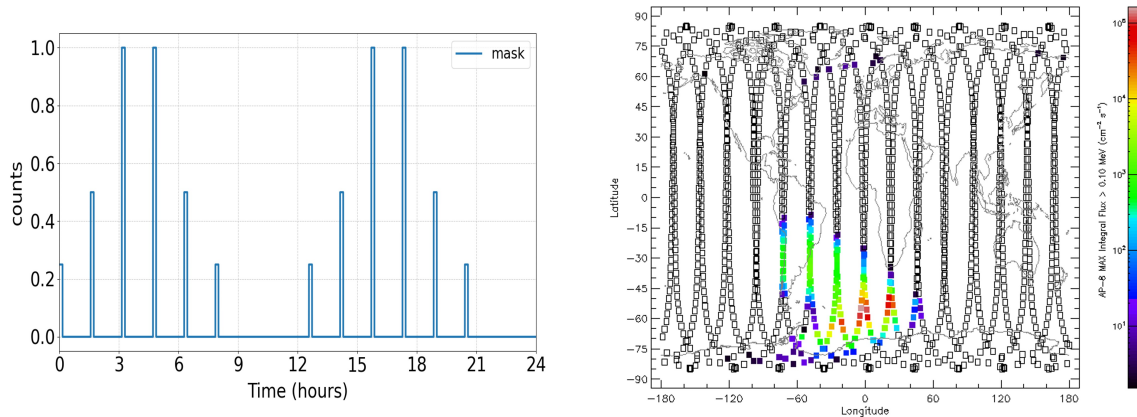


Figure A.3.: **Time distribution of all hits in the detectors originating from radioactive decays.** Hits in the calorimeter are shown in red, while hits in the SDD are depicted in blue. Additionally, the remaining events after event selection are drawn in green.

shows, that the main contribution consists of particles originating from short-living isotopes, hence they reach the detectors only with a small delay regarding the event-start. Overall, all events with a timestamp up to one year after event-start are taken into account for the final analysis. Events, from very long-living isotopes, reach the detectors long after the mission's end and do not contribute to the relevant background. In order to transform the timestamps after event-start into a temporal evolution, starting with the mission, the data is convolved with a specific mask. The mask resembles the time in orbit when the SAA is passed. The mask for extrapolation to one day in orbit is shown in Figure A.4a. Additionally, the orbit of the CubeSat for one day is shown in Figure A.4b. The SAA is passed during six consecutive orbits, while a full passage through the maximum flux happens only during two orbits. These orbits correspond to the highest peaks on the mask. Partial passages through the SAA in the previous and consecutive orbits are accounted for with lower peaks in the mask. Overall, the SAA is passed twice per day. The numerical convolution of the histogram of the timestamps after event-start (in counts) and the mask leads to the temporal evolution of the activation in the detector system. The mask has to be generated separately for protons and electrons to account for the exact time the satellite spends in the regions of increased flux. Since the SAA-electrons cover a larger area above the south Atlantic and an additional region of increased electron flux is found above the poles (c.f. Figure 3.2b), the mask for the electrons has broader peaks. After normalization with the simulation time the activation rate as shown in Figure 5.8 is generated. The convolution was performed with python using the numpy package. Via the convolution technique, an extrapolation to one week, one month, or one year in orbit can be generated. The respective maps consist of 7, 30 or 365 copies of the map for one day. The normalization must be taken care of individually for each extrapolation. Using the convolution allows to extrapolate the activation rate in the detectors to a extended time frame, however, the actual simulated time with the SAA spectrum only corresponds to 2370.1 s (for protons). Simulating a full SAA orbit would have been too costly in terms of time and CPU power.

## A. Appendix



(a) Mask for the convolution for protons. The peaks correspond to the SAA. (b) SAA-protons flux of the CubeSat during one day with regard to its position.

Figure A.4.: **Mask and SAA-proton flux for one day.** a) represents the mask used for the convolution with the SAA-proton background. b) shows the SAA-proton flux during one day with respect to the position of the CubeSat. The satellite passes through parts of the region of increased flux during 6 consecutive orbits. This is accounted for in the mask by 6 peaks with varying heights. The SAA is passed twice a day. Therefore the peaks in the mask are presented twice.

## A.5. Additional figures for the shielding study with different Materials

The attenuation characteristics in the used materials are given in [subsection A.5.1](#). In [subsection A.5.2](#) the spectra at different stages of event selection are shown for all materials. Furthermore, the fluorescence lines are drawn into the figures and discussed in the subsection.

### A.5.1. Attenuation of photons in different materials

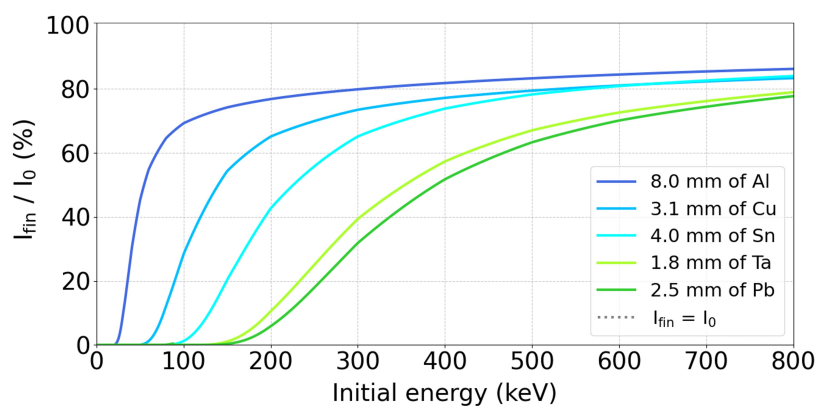


Figure A.5.: **Final intensity vs. initial energy for all simulated collimator-materials.** The thickness of the collimator for each material is given in the legend. Each thickness corresponds to the mass equivalent of a 2 mm lead shielding.

A.5. Additional figures for the shielding study with different Materials

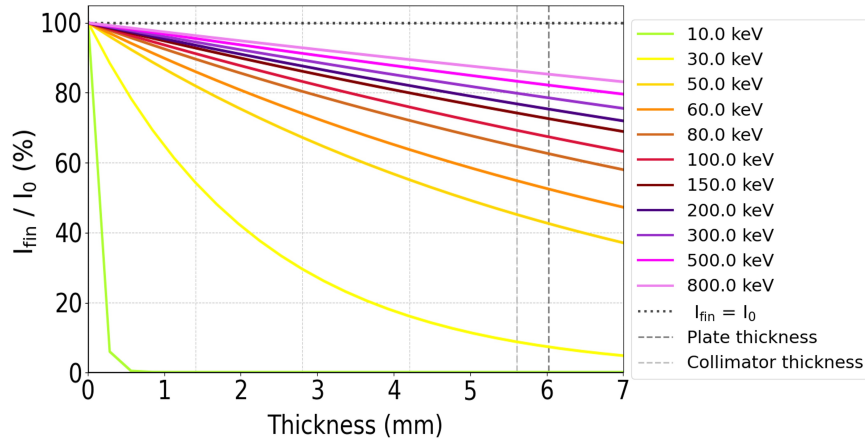


Figure A.6.: **Dependence of the final photon intensity on the thickness of the aluminum shielding for different initial photon energies.** The shielding plate thickness is marked with a grey dashed vertical line at 8.6 mm. The thickness of the collimator wall is shown with a dashed line in light grey and is set to 8.0 mm

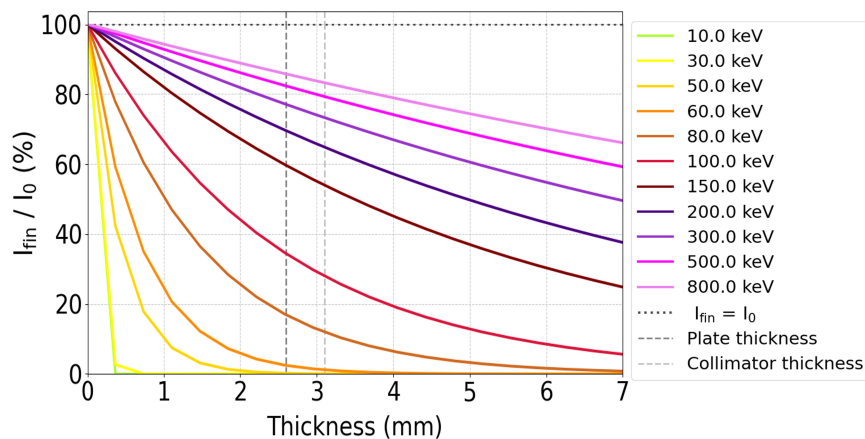


Figure A.7.: **Dependence of the final photon intensity on the thickness of the copper shielding for different initial photon energies.** The shielding plate thickness is marked with a grey dashed vertical line at 2.6 mm. The thickness of the collimator wall is shown with a dashed line in light grey and is set to 3.1 mm

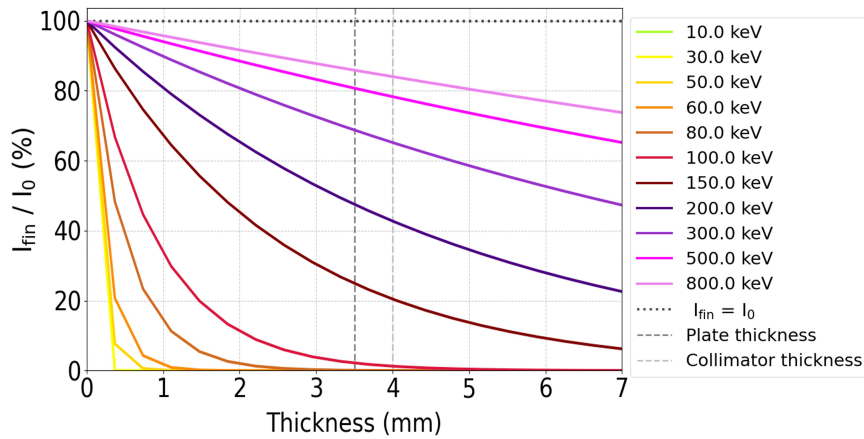


Figure A.8.: **Dependence of the final photon intensity on the thickness of the tin shielding for different initial photon energies.** The shielding plate thickness is marked with a grey dashed vertical line at 3.5 mm. The thickness of the collimator wall is shown with a dashed line in light grey and is set to 4.0 mm

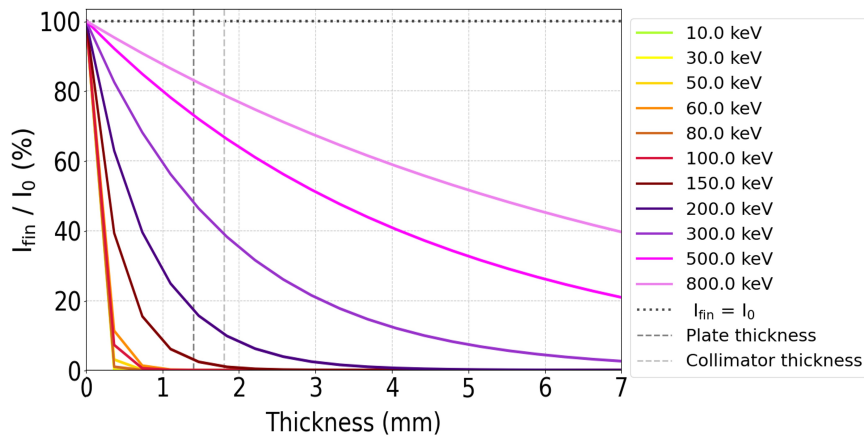


Figure A.9.: **Dependence of the final photon intensity on the thickness of the tantalum shielding for different initial photon energies.** The shielding plate thickness is marked with a grey dashed vertical line at 1.4 mm. The thickness of the collimator wall is shown with a dashed line in light grey and is set to 1.8 mm

### A.5.2. Spectra and fluorescence lines with different shielding materials

In the following, a larger energy range of the lead spectra is shown in [Figure A.10](#) in order to illustrate the 511 keV line. The positron-electron annihilation line is also visible in all shielding configurations, however, it is not shown at this point. The configuration without shielding has no visible 511 keV line since there is no shielding material in which the positrons could annihilate placed in front of the detectors.

Additionally, the spectra for all investigated shielding materials are depicted (see [Figure A.11](#) and [Figure A.12](#)). The aluminum spectrum is depicted in [Figure A.11a](#). Again the lines from

### A.5. Additional figures for the shielding study with different Materials

cerium and bromine are visible. The fluorescence lines for aluminum are not visible there in the detectors. Figure A.11b illustrates the spectra with the copper configuration. Only the  $K_\beta$  line for Copper is slightly visible in the detectors. The fluorescence lines from Tin are easily visible in Figure A.12a. They appear strongly in both detectors and are more pronounced as the cerium lines, which are together with the bromine lines visible as well. The  $K_{\alpha,2}$  and  $K_\beta$  lines from tin contribute also to the coincident events. This area is marked with a grey circle. The final background rate however has no visible contribution of the tin fluorescence lines anymore. Figure A.12b depicts the spectra with the tantalum shielding. The  $K_{\alpha,2}$  and  $K_\beta$  lines from tantalum are all visible in both detectors, however, they do not visibly contribute to the spectrum of coincident events, nor the final spectrum.

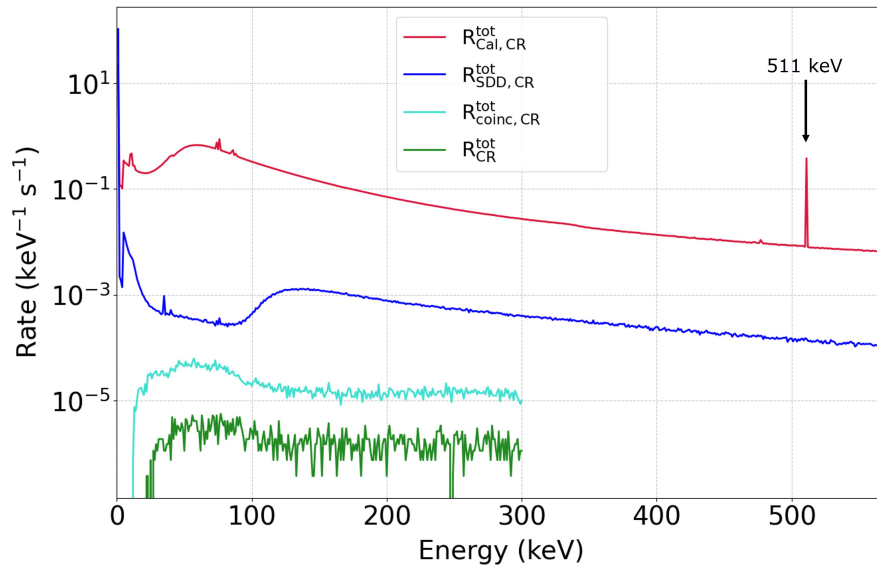
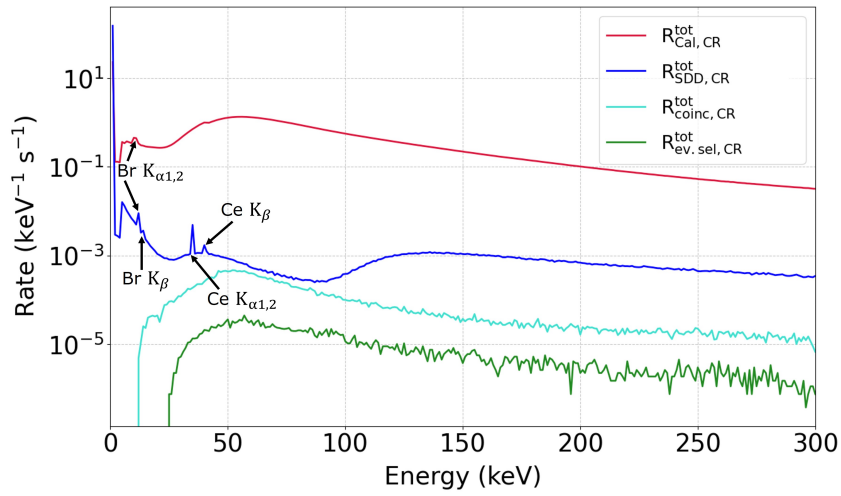
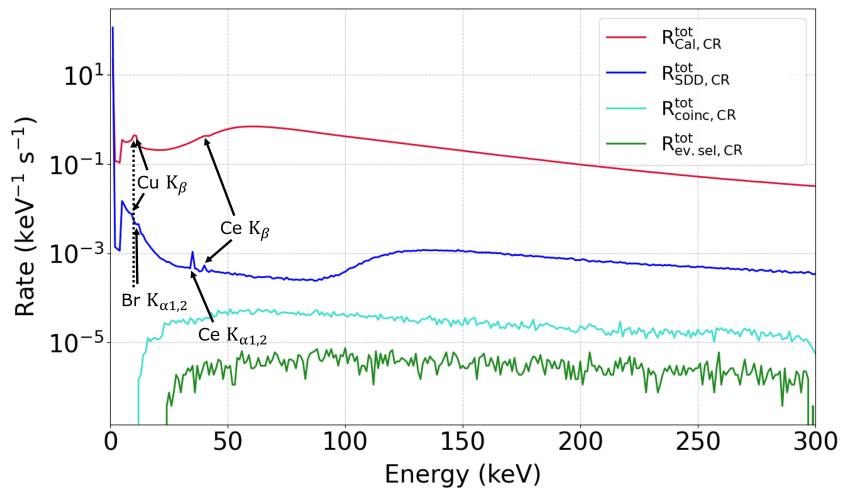


Figure A.10.: **Energy spectrum for the shielding configuration with lead.** The total rate in the calorimeter is shown in red, while the rate in the SDD is depicted in blue. The rate of all coincident events is marked in turquoise, and the rate after event selection is drawn in green. The 511 keV line from positron-electron annihilation is clearly visible.



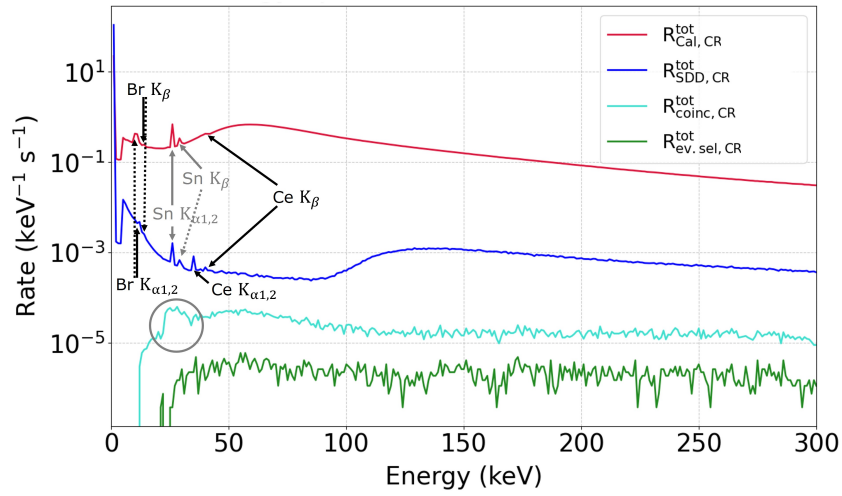
(a) Energy spectrum for the shielding configuration with aluminum in the region of interest. The fluorescence lines of cerium, bromine are indicated.



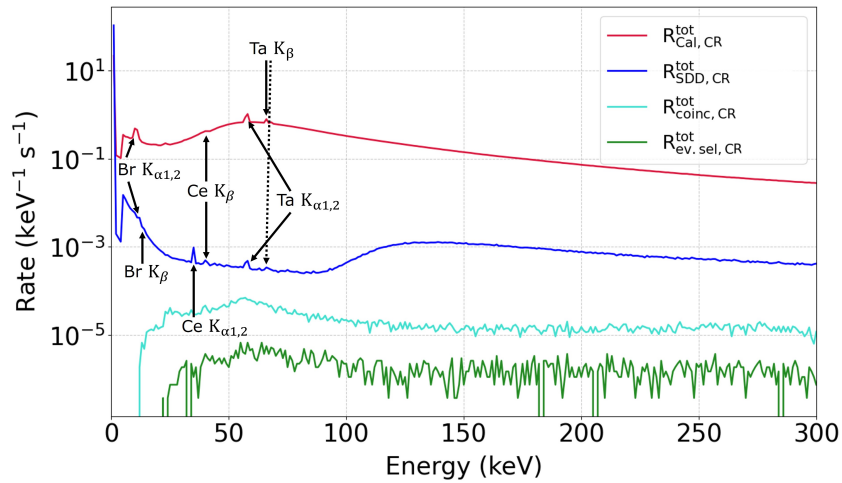
(b) Energy spectrum for the shielding configuration with copper in the region of interest. The fluorescence lines of cerium, bromine, and copper are also indicated.

Figure A.11.: **Energy spectrum for the all shielding configurations in the region of interest.** The total rate in the calorimeter is shown in red, while the rate in the SDD is depicted in blue. The rate of all coincident events is marked in turquoise, and the rate after event selection is drawn in green. The fluorescence energies can be obtained in [Table 6.5](#).

A.5. Additional figures for the shielding study with different Materials



(a) Energy spectrum for the shielding configuration with tin in the region of interest. The fluorescence lines of cerium, bromine (black), and tin (grey) are also indicated.



(b) Energy spectrum for the shielding configuration with tantalum in the region of interest. The fluorescence lines of cerium, bromine, and tantalum are also indicated.

Figure A.12.: **Energy spectrum for the all shielding configurations in the region of interest.** The total rate in the calorimeter is shown in red, while the rate in the SDD is depicted in blue. The rate of all coincident events is marked in turquoise, and the rate after event selection is drawn in green. The fluorescence energies can be obtained in [Table 6.5](#).



# Bibliography

- [1] Meier Matthias. Master's thesis: Tristan fly high - design studies for a cubesat compton telescope, 2019.
- [2] J LaSala, PA Charles, RAD Smith, M Bałucińska-Church, and MJ Church. The orbital period of hde 226868/cyg x-1. *Monthly Notices of the Royal Astronomical Society*, 301(1):285–288, 1998.
- [3] Joseph F Dolan. A catalogue of discrete celestial x-ray sources. *The Astronomical Journal*, 75:223, 1970.
- [4] Charles Thomas Bolton. Identification of cygnus x-1 with hde 226868. *Nature*, 235(5336):271–273, 1972.
- [5] Mark J Reid, Jeffrey E McClintock, Ramesh Narayan, Lijun Gou, Ronald A Remillard, and Jerome A Orosz. The trigonometric parallax of cygnus x-1. *The Astrophysical Journal*, 742(2):83, 2011.
- [6] J Ziółkowski. Determination of the masses of the components of the hde 226868/cyg x-1 binary system. *Monthly Notices of the Royal Astronomical Society: Letters*, 440(1):L61–L65, 2014.
- [7] V Grinberg, K Pottschmidt, M Böck, C Schmid, MA Nowak, P Uttley, JA Tomsick, J Rodriguez, N Hell, A Markowitz, et al. Long term variability of cygnus x-1-vi. energy-resolved x-ray variability 1999–2011. *Astronomy & Astrophysics*, 565:A1, 2014.
- [8] Floriane Cangemi, Jérôme Rodriguez, Victoria Grinberg, Philippe Laurent, and Joern Wilms. High energy spectral study of the black hole cygnus x-1 with integral. *arXiv preprint arXiv:1810.12049*, 2018.
- [9] Philippe Laurent, J Rodriguez, J Wilms, M Cadolle Bel, K Pottschmidt, and V Grinberg. Polarized gamma-ray emission from the galactic black hole cygnus x-1. *Science*, 332(6028):438–439, 2011.
- [10] Josep M Paredes. Gamma rays from compact binary systems. In *AIP Conference Proceedings*, volume 1085, pages 157–168. American Institute of Physics, 2008.
- [11] Jörn Wilms, MA Nowak, Katja Pottschmidt, Guy G Pooley, and Sonia Fritz. Long term variability of cygnus x-1-iv. spectral evolution 1999–2004. *Astronomy & Astrophysics*, 447(1):245–261, 2006.
- [12] Philippe Laurent and Lev Titarchuk. The converging inflow spectrum is an intrinsic signature for a black hole: Monte carlo simulations of comptonization on free-falling electrons. *The Astrophysical Journal*, 511(1):289, 1999.

## Bibliography

- [13] Jérôme Rodriguez, Victoria Grinberg, Philippe Laurent, Marion Cadolle Bel, Katja Pottschmidt, Guy Pooley, Arash Bodaghee, Jörn Wilms, and Christian Gouiffès. Spectral state dependence of the 0.4–2 MeV polarized emission in Cygnus X-1 seen with Integral/IBIS, and links with the AMI radio data. *The Astrophysical Journal*, 807(1):17, 2015.
- [14] Arthur H Compton. A quantum theory of the scattering of x-rays by light elements. *Physical Review*, 21(5):483, 1923.
- [15] Si Chen, H Avakian, VD Burkert, P Eugenio, G Adams, M Amarian, P Ambrozewicz, M Anghinolfi, G Asryan, H Bagdasaryan, et al. Measurement of deeply virtual Compton scattering with a polarized-proton target. *Physical Review Letters*, 97(7):072002, 2006.
- [16] Oskar Klein and Yoshio Nishina. Über die Streuung von Strahlung durch freie Elektronen nach der neuen relativistischen Quantendynamik von Dirac. *Zeitschrift für Physik*, 52(11):853–868, 1929.
- [17] Andreas Christian Zoglauer. *First Light for the next Generation of Compton and Pair Telescopes*. PhD thesis, Technische Universität München, 2005.
- [18] Tod E Strohmayer and Tim R Kallman. On the statistical analysis of x-ray polarization measurements. *The Astrophysical Journal*, 773(2):103, 2013.
- [19] J. Chin, R. Coelho, and et al. CubeSat101 – Basic Concepts and Processes for First-Time CubeSat Developerse. [https://www.nasa.gov/sites/default/files/atoms/files/nasa\\_csli\\_cubesat\\_101\\_508.pdf](https://www.nasa.gov/sites/default/files/atoms/files/nasa_csli_cubesat_101_508.pdf), 2017. [Online; accessed 21-March-2022].
- [20] S Mertens, T Lasserre, S Groh, G Drexlin, F Glueck, A Huber, AWP Poon, M Steidl, N Steinbrink, and C Weinheimer. Sensitivity of next-generation tritium beta-decay experiments for keV-scale sterile neutrinos. *Journal of Cosmology and Astroparticle Physics*, 2015(02):020, 2015.
- [21] Susanne Mertens, Antonio Alborini, Konrad Altenmüller, Tobias Bode, Luca Bombelli, Tim Brunst, Marco Carminati, David Fink, Carlo Fiorini, Thibaut Houdy, et al. A novel detector system for KATRIN to search for keV-scale sterile neutrinos. *Journal of Physics G: Nuclear and Particle Physics*, 46(6):065203, 2019.
- [22] F Perotti and C Fiorini. Observed energy dependence of Fano factor in silicon at hard x-ray energies. *Nuclear Instruments and Methods in Physics Research Section A: Accelerators, Spectrometers, Detectors and Associated Equipment*, 423(2-3):356–363, 1999.
- [23] T Brunst, S Mertens, K Altenmüller, T Houdy, D Siegmann, M Slezák, A Alborini, L Bombelli, M Carminati, C Fiorini, et al. Development of a silicon drift detector system for the TRISTAN project—future search for sterile neutrinos. *Nuclear Instruments and Methods in Physics Research Section A: Accelerators, Spectrometers, Detectors and Associated Equipment*, 936:235–236, 2019.
- [24] WM Higgins, A Churilov, E Van Loef, J Glodo, M Squillante, and K Shah. Crystal growth of large diameter LaBr<sub>3</sub>:Ce and CeBr<sub>3</sub>. *Journal of Crystal Growth*, 310(7-9):2085–2089, 2008.
- [25] A. Gostojic. *Development of a Compton Telescope with 3D Imaging Calorimeter for Gamma-Ray Astronomy*. PhD thesis, Université Paris-Saclay, 2016.

- [26] Martin C Weisskopf. X-ray polarimetry: historical remarks and other considerations. *X-Ray Polarimetry: A New Window in Astrophysics*, 1:1–8, 2010.
- [27] P Cumani, M Hernanz, J Kiener, V Tatischeff, and A Zoglauer. Background for a gamma-ray satellite on a low-earth orbit. *Experimental Astronomy*, 47(3):273–302, 2019.
- [28] Merlin Kole, Mark Pearce, and Maria Muñoz Salinas. A model of the cosmic ray induced atmospheric neutron environment. *Astroparticle Physics*, 62:230–240, 2015.
- [29] ESA. SPENVIS – The NASA models AP-8 and AE-8. <https://www.spennis.oma.be/help/background/traprad/traprad.html#APAE>, 2018. [Online; accessed 27-March-2022].
- [30] operated by Royal Belgian Institute for Space Aeronomy ESA. SPENVIS – website. <https://www.spennis.oma.be/>, 2022. [Online; accessed 27-March-2022].
- [31] Susana Cebrián Guajardo. Cosmogenic Activation. <https://encyclopedia.pub/3265>, 2020. [Online; accessed 14-March-2022].
- [32] Harry Friedmann. *Einführung in die Kernphysik*. John Wiley & Sons, 2014.
- [33] Kyōto Daigaku. Kiso Butsurigaku Kenkyūjo and Nihon Butsuri Gakkai. *Progress of Theoretical Physics*. Number Bd. 35,Nr. 1-3. Yukawa Hall, 1966.
- [34] Werner Stolz. *Radioaktivität: Grundlagen-Messung-Anwendungen*. Springer-Verlag, 2013.
- [35] Vitaly A Kudryavtsev. Cosmogenic activation: Recent results. In *AIP Conference Proceedings*, volume 1921, page 090004. AIP Publishing LLC, 2018.
- [36] Steffen Hauf, Markus Kuster, Matej Batič, Zane W Bell, Dieter HH Hoffmann, Philipp M Lang, Stephan Neff, Maria Grazia Pia, Georg Weidenspointner, and Andreas Zoglauer. Radioactive decays in geant4. *IEEE Transactions on Nuclear Science*, 60(4):2966–2983, 2013.
- [37] Kris Heyde. *Basic ideas and concepts in nuclear physics: an introductory approach*. CRC Press, 2020.
- [38] Geant4 Collaboration. Geant4 – website. <https://geant4.web.cern.ch/>, 2022. [Online; accessed 07-April-2022].
- [39] Sea Agostinelli, John Allison, K al Amako, John Apostolakis, H Araujo, Pedro Arce, Makoto Asai, D Axen, Swagato Banerjee, GJNI Barrand, et al. Geant4—a simulation toolkit. *Nuclear instruments and methods in physics research section A: Accelerators, Spectrometers, Detectors and Associated Equipment*, 506(3):250–303, 2003.
- [40] IAEA. International Atomic Energy Agency - Nuclear Data Services - LiveChart of Nuclides. <https://www-nds.iaea.org/relnsd/vcharthtml/VChartHTML.html#dcy2>, 2022. [Online; accessed 10-May-2022].
- [41] Estanislao Aguayo Navarrete, John L Orrell, and Richard T Kouzes. Monte carlo simulations of cosmic rays hadronic interactions. Technical report, Pacific Northwest National Lab.(PNNL), Richland, WA (United States), 2011.
- [42] Mark Fox. *Optical properties of solids*, 2002.

## Bibliography

- [43] NASA. NASA - Basic Information Regarding Tin Whiskers. <https://nepp.nasa.gov/whisker/background/index.htm#q3>, 2022. [Online; accessed 07-May-2022].
- [44] David Hall, Jonathan Keelan, Chris Davis, Oliver Hetherington, Mark Leese, and Andrew Holland. Predicting the particle-induced background for future x-ray astronomy missions: the importance of experimental validation for geant4 simulations. In *High Energy, Optical, and Infrared Detectors for Astronomy VIII*, volume 10709, page 1070937. International Society for Optics and Photonics, 2018.
- [45] Steffen Hauf, Markus Kuster, Maria Grazia Pia, Dieter HH Hoffmann, Philipp Lang, Stephan Neff, Alexander Stefanescu, and Lothar Strüder. Background simulations of the wide field imager of the athena x-ray observatory. In *2011 IEEE Nuclear Science Symposium Conference Record*, pages 1239–1243. IEEE, 2011.
- [46] S Neff, S Hauf, P Lang, M Roth, M Günther, O Deppert, DHH Hoffmann, M Kuster, MG Pia, and ZW Bell. An activation experiment with laser-accelerated high-energy protons to optimize the graded-z shield design for the ixo/athena satellite missions. In *2011 IEEE Nuclear Science Symposium Conference Record*, pages 1194–1196. IEEE, 2011.
- [47] David W Robinson. Building a new kind of graded-z shield for swift’s burst alert telescope. In *X-Ray and Gamma-Ray Telescopes and Instruments for Astronomy*, volume 4851, pages 1374–1381. International Society for Optics and Photonics, 2003.

## Acknowledgment

I would like to conclude by thanking everyone who helped me along the way and contributed to the outcome of this thesis.

### **Susanne Mertens**

Thank you for making it possible for me to complete this thesis. Your support during the discussions about my progress was always constructive and enriching.

### **Matthias Meier**

Thank you, Matthias, for the many hours you spent proofreading and participating in long zoom-calls and discussions with me. You always had an open ear for my questions about python, Geant4, my simulations, and the activation theory. You accompanied me from the beginning and always supported me and especially worked wonders when fixing my code. With your help, your patience, and the time you invested in me, I grew up to be a "Master-antin". Without you, this work would not have come into being.

### **The Container Crew**

Thank you, for many lunches with educational discussions on everything from neutrinos to all sorts of 3D printing projects. It was a pleasant environment to sit together with you and have a relaxed lunchtime exchange. Unfortunately, I couldn't take full advantage of this beautiful environment because of Corona.

### **My Lieblingsmensch**

Thank you Moritz, for always standing by me. You have always counteracted my temporary depressions with your care and confident words. My questions of all kinds always find two open ears with you and you always give me good advice along the way.

### **My family**

Many thanks to all of you for always supporting me in my studies.

Munich, 17.05.2022